



January 2021

Computational Studies Of Metal-Substituted Systems And Development Of Machine Learning Within GVVPT2

Minh Duong Popis

[How does access to this work benefit you? Let us know!](#)

Follow this and additional works at: <https://commons.und.edu/theses>

Recommended Citation

Popis, Minh Duong, "Computational Studies Of Metal-Substituted Systems And Development Of Machine Learning Within GVVPT2" (2021). *Theses and Dissertations*. 4178.
<https://commons.und.edu/theses/4178>

This Dissertation is brought to you for free and open access by the Theses, Dissertations, and Senior Projects at UND Scholarly Commons. It has been accepted for inclusion in Theses and Dissertations by an authorized administrator of UND Scholarly Commons. For more information, please contact und.common@library.und.edu.

COMPUTATIONAL STUDIES OF METAL-SUBSTITUTED SYSTEMS AND
DEVELOPMENT OF MACHINE LEARNING WITHIN GVVPT2

by

Minh Duong Popis
Bachelor of Arts, Drury University, 2014

A Dissertation

Submitted to the Graduate

Faculty of the

University of North Dakota

in partial fulfillment of the requirements

for the

degree of

Doctor of Philosophy

Grand Forks, North Dakota

December 2021

Copyright 2021 Minh Popis

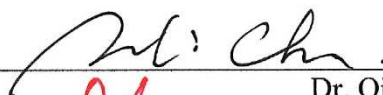
This dissertation, submitted by Minh Popis in partial fulfillment of the requirements for the Degree of Doctor of Philosophy from the University of North Dakota, has been read by the Faculty Advisory Committee under whom the work has been done and is hereby approved.



Dr. Mark R. Hoffmann (Chair)



Dr. Evguenii Kozliak



Dr. Qianli Rick Chu



Dr. Yen Lee Loh



Dr. Nuri Oncel

This dissertation is being submitted by the appointed advisory committee as having met all of the requirements of the School of Graduate Studies at the University of North Dakota and is hereby approved.

Chris Nelson
Dean of the School of Graduate Studies

Date

PERMISSION

Title Computational Studies of Metal-substituted Systems and
 Development of Machine Learning within GVVPT2

Department Chemistry

Degree Doctor of Philosophy

In presenting this dissertation in partial fulfillment of the requirements for a graduate degree from the University of North Dakota, I agree that the library of this University shall make it freely available for inspection. I further agree that permission for extensive copying for scholarly purposes may be granted by the professor who supervised my dissertation work or, in his absence, by the Chairperson of the department or the dean of the School of Graduate Studies. It is understood that any copying or publication or other use of this dissertation or part thereof for financial gain shall not be allowed without my written permission. It is also understood that due recognition shall be given to me and to the University of North Dakota in any scholarly use which may be made of any material in my dissertation.

Minh Popis

November 15, 2021

TABLE OF CONTENTS

LIST OF FIGURES	vii
LIST OF TABLES	x
ABBREVIATIONS	xii
ACKNOWLEDGEMENTS	xvii
ABSTRACT	xix
CHAPTERS	1
I. INTRODUCTION	1
Theoretical and Computational Chemistry	1
Theoretical Studies of Two-Dimensional Materials	3
Theoretical Studies of Astrophysical Molecules	6
Development of Machine Learning in Computational Chemistry	8
Dissertation Framework	10
II. METHODS	11
Time-Independent Schrödinger Equation	11
Hartree–Fock Approximation	12
Density Functional Theory	15
Second-Order Møller–Plesset Perturbation Theory	27
Multiconfigurational Self-Consistent Field	32
Second-Order Generalized van Vleck Perturbation Theory	38
The Spin-Free Exact Two-Component Method	42
Advances in Active Space Selection using Machine Learning	45
III. THEORETICAL STUDIES OF IRIDIUM SILICIDE MONOLAYERS USING DENSITY FUNCTIONAL THEORY	48

Introduction	48
Computational Methods	50
Results and Discussion	51
Conclusions	66
IV. THEORETICAL STUDIES OF CALCIUM MONOHYDROXIDE AND STRONTIUM MONOHYDROXIDE MONOMERS USING GVVPT2.....	68
Introduction	68
Computational Methods	71
Results and Discussion	71
Conclusions	77
V. THEORETICAL STUDIES OF CALCIUM MONOHYDROXIDE DIMERIZATION USING GVVPT2	78
Introduction	78
Computational Methods	79
Discussion and Future Directions.....	80
VI. DEVELOPMENT OF MACHINE LEARNING IN ACTIVE SPACE SELECTION WITHIN GVVPT2	83
Introduction	83
Computational Methods	86
Results and Discussion	91
Conclusions	106
CONCLUDING REMARKS AND FUTURE DIRECTIONS.....	108
REFERENCES	110

LIST OF FIGURES

Figure I-1. Comparison of the crystal structures between (a) top view and (b) side view of graphene and (c) top view and (d) side view of silicene. The graphene has a perfect planar structure, while silicene possesses a slightly out-of-plane buckling structure (h denotes the buckling distance). (Image taken from Ref. ⁷⁶)	4
Figure II-1. Perdew's metaphorical Jacob's Ladder of XC functionals. (Image taken from Ref. ¹⁸⁴)	20
Figure II-2. The crystal structure (c) is form by the basis (b) occupying each lattice point of the space lattice (a). (Image taken from Ref. ¹⁸⁷)	22
Figure II-3. Illustration of the atomic core and interstitial regions in a valence wavefunction. (Image taken from Ref. ¹⁸⁸).....	25
Figure II-4. Three subspaces of a CASSCF ansatz (the arrow represents electron excitations for generating a full CI within the active space). (Image taken from Ref. ²²²)	34
Figure II-5. Schematic representation of a RASSCF ansatz (the arrows represent electron excitations within the active space).	36
Figure II-6. Schematic representation of the subspaces labelled with their corresponding Hamiltonian matrices within a GVVPT2 ansatz.....	41
Figure III-1. The top and side views of rectangular r-IrSi ₂ monolayer. The optimized lattice constants are $a = 6.18 \text{ \AA}$ and $b = 2.84 \text{ \AA}$. (Image taken from Ref. ¹¹⁴)	52
Figure III-2. The top and side views of the ELF for the r-IrSi ₂ monolayer. The ELF isovalue is set to 0.7. (Image taken from Ref. ¹¹⁴)	53

Figure III-3. Direction-dependent (a) Young's modulus (N/m) and (b) Poisson's ratio for the r-IrSi ₂ monolayer. (Image taken from Ref. ¹¹⁴).....	55
Figure III-4. Phonon spectra and PDOS of the rectangular r-IrSi ₂ monolayer. (Image taken from Ref. ¹¹⁴).....	57
Figure III-5. Band structure and orbital decomposed DOS of the r-IrSi ₂ monolayer. The Fermi level marks the zero energy. (Image taken from Ref. ¹¹⁴).....	58
Figure III-6. The top and side views of several optimized Ir-Si monolayers. Cohesive energies (eV) per formula unit are given for each structure. (Image taken from Ref. ¹¹⁴)	59
Figure III-7. Phonon spectra of (a) h-Ir ₂ Si and (b) t-IrSi monolayers. (Image taken from Ref. ¹¹⁴)	61
Figure III-8. Calculated Helmholtz free energies and entropies for (a) r-IrSi ₂ , (b) t-IrSi, and (c) h-Ir ₂ Si monolayers. (Image taken from Ref. ¹¹⁴)	63
Figure III-9. The lowest energy adsorption structure of (a) H ₂ O and (b) O ₂ on the free-standing r-IrSi ₂ monolayer. (Image taken from Ref. ¹¹⁴).....	65
Figure IV-1. Equilibrium structure of CaOH optimized at the GVVPT2/cc-pVTZ level.	72
Figure IV-2. Equilibrium structure of SrOH optimized at the GVVPT2/cc-pVTZ level (a) with and (b) without relativistic corrections.	75
Figure V-1. The starting arrangement of two CaOH monomers in our study of CaOH dimerization.	82
Figure VI-1. Schematic representation of our ML model.....	90
Figure VI-2. Equilibrium structure of ³ CH ₂ constructed from the experimental values of its geometry parameters.	101

Figure VI-3. Structure of the stretched water constructed from the experimental values of its geometry parameters. 104

LIST OF TABLES

Table IV-1. Comparison of geometry parameters (\AA and degrees) of the ground state of CaOH optimized at the GVVPT2/cc-pVTZ level with other <i>ab initio</i> methods and with experimental data.	73
Table IV-2. Comparison of vertical excitation energies T_e for the first low-lying excited state of CaOH calculated at the GVVPT2/cc-pVTZ level with other <i>ab initio</i> methods and with experimental data. $T_e = 0$ eV for the ground state.	74
Table IV-3. Comparison of geometry parameters (\AA and degrees) of the ground state of SrOH optimized at the GVVPT2/cc-pVTZ level with other <i>ab initio</i> methods and with experimental data.	76
Table VI-1. The occurrences (times) and the occurrence probabilities (%) that our ML model found the desired configurations for H ₂ O in different learning durations.	95
Table VI-2. The total number of configurations found by our ML model that met all the predetermined conditions. (LR = 10 ⁻⁸).....	97
Table VI-3. The occurrences (times) and the occurrence probabilities (%) that our ML model found the desired configurations for H ₂ O using different LRs with 50,000 as the maximum number of episodes.	99
Table VI-4. Comparison of electronic energies of ³ CH ₂ computed with different active space configurations at the GVVPT2/DH level. The data from published literature is also included.....	103

Table VI-5. Comparison of electronic energies of the stretched H₂O computed with
different active space configurations at the GVVPT2/DH level. 105

ABBREVIATIONS

AMBER	Assisted Model Building with Energy Refinement
AM1	Austin Model 1
AO	Atomic Orbital
APW	Augmented Plane Wave
a.u.	Atomic Unit
B3LYP	Becke 1988 Three Parameter Hybrid Functional with Lee– Yang–Parr Exchange–Correlation Functional
B88	Becke 1988 Exchange–Correlation Functional
CAS	Complete Active Space
CASPT2	Complete Active Space Second-Order Perturbation Theory
CASSCF	Complete Active Space Self-Consistent Field
CC	Coupled Cluster
cc-pVTZ	Correlation Consistent Polarized Valence Triple Zeta Basis Set
cc-pVTZ-X2C	Correlation Consistent Polarized Valence Triple Zeta Basis Set for Exact Two-Component
CI	Configuration Interaction
CNN	Convolutional Neural Network
CSF	Configuration State Function
DFPT	Density Functional Perturbation Theory
DFT	Density Functional Theory

DFT-D3	Density Functional Theory with Dispersion Corrections
DH	Dunning/Huzinaga Double Zeta Basis Set
DMRG	Density Matrix Renormalization Group
DOS	Density of States
ELF	Electron Localization Function
f.u.	Formula Unit
GGA	Generalized Gradient Approximation
GVVPT2	Second-Order Generalized van Vleck Perturbation Theory
HF	Hartree–Fock
HK	Hohenberg–Kohn
HOMO	Highest Occupied Molecular Orbital
HSE06	Heyd–Scuseria–Ernzerhof Exchange–Correlation Functional
H^v	Effective Valence Shell Hamiltonian
ICF	Inhomogeneity Correction Factor
KS	Kohn–Sham
KS-DFT	Kohn–Sham Density Functional Theory
LA	Longitudinal Acoustic
LDA	Local Density Approximation
LR	Learning Rate
LSDA	Local Spin Density Approximation
LUMO	Lowest Unoccupied Molecular Orbital
LYP	Lee–Yang–Parr
MCSCF	Multiconfigurational Self-Consistent Field

ML	Machine Learning
MM	Molecular Mechanics
MNDO	Modified Neglect of Diatomic Overlap
MO	Molecular Orbital
MPPT	Møller–Plesset Perturbation Theory
MP1	First-Order Møller–Plesset Perturbation Theory
MP2	Second-Order Møller–Plesset Perturbation Theory
MR-CC	Multireference Coupled Cluster
MR-CI	Multireference Configuration Interaction
MR-CISD	Multireference Configuration Interaction with Single and Double Excitations
MRD–CI	Multireference Double-Excitation Configuration Interaction
MRPT	Multireference Perturbation Theory
MSE	Mean Squared Error
NESC	Normalized Elimination of Small Component
NN	Neural Network
PAW	Projector Augmented Wave
PBE	Perdew–Burke–Ernzerhof Exchange–Correlation Functional
PDOS	Phonon Density of States
P86	Perdew 1986 Exchange–Correlation Functional
PM3	Parametric Method 3
P2RDM	Parametric Two-Electron Reduced Density Matrix
PW91	Perdew–Wang 1991 Exchange–Correlation Functional

PW92	Perdew–Wang 1992 Exchange–Correlation Functional
PZ81	Perdew–Zunger 1981 Exchange–Correlation Functional
QM	Quantum Mechanics
RAS	Restricted Active Space
RASSCF	Restricted Active Space Self-Consistent Field
RCCSD(T)	Spin-Restricted Coupled Cluster with Single, Double, and Perturbative Triple Excitations
RHF	Restricted Hartree–Fock
RMP2	Restricted Second-Order Møller–Plesset Perturbation Theory
rovibronic	Rotation-Vibration-Electronic
RSPT	Rayleigh–Schrödinger Perturbation Theory
SCF	Self-Consistent Field
sd	Spin-Dependent
sf	Spin-Free
sf-X2C	Spin-Free Exact Two-Component
TA	Transverse Acoustic
2D	Two-Dimensional
3D	Three-Dimensional
TD-DFT	Time-Dependent Density Functional Theory
TM	Transition Metal
UEG	Uniform Electron Gas
UHF	Unrestricted Hartree–Fock
UND	University of North Dakota

VWN	Vosko–Wilk–Nusair Exchange–Correlation Functional
WFT	Wave Function Theory
XC	Exchange–Correlation
X2C	Exact Two-Component
ZA	Flexural Acoustic

ACKNOWLEDGEMENTS

First of all, I would like to express my sincere gratitude to my advisor, Dr. Mark R. Hoffmann for accepting me into his research group and helping me attain a firm grasp of computational electronic structure theories. There was a point in my research journey, I had lost my purpose in pursuing the doctorate degree. Thank you, Dr. Hoffmann, for helping me find my passion in research again by showing me the possibilities of applying computational chemistry theories to the field of astrophysics and machine learning. He helped me get back on track and finish my goal. His passion for research and teaching will continue to be my inspiration for years to come.

Second, I would like to thank my committee members, Dr. Evgenii Kozliak, Dr. Qianli Rick Chu, Dr. Yen Lee Loh, and Dr. Nuri Oncel, for their guidance and support with my research. Thank you, Dr. Kozliak, for recruiting me to join the graduate program at the University of North Dakota (UND). Without this opportunity, I would have never met many wonderful individuals who have taught me so much. Thank you, Dr. Loh, for teaching me the basics of machine learning and many other fascinating physics phenomena. I would like to thank Dr. Chu for being kind and supportive throughout my study at UND. And a big thank-you to Dr. Oncel and Dr. Deniz Çakir from the UND Physics and Astrophysics Department for your collaboration with the iridium silicide project. I also wish to express my great appreciation to Dr. Kathryn Thomasson who passed away last year. She was an excellent mentor and a wonderful friend. I cannot thank her enough for all the love and support she had given me.

I would also like to thank the members of my research group: Sylvester V. Popis, Dr. Jason Hicks, Dr. Run Li, Dr. Eric Timian, Aliakbar Sepehri, Hans Musgrave, and Brandon Bush for their support and assistance. Without you, research would not have been that much fun. In addition, I would like to express my appreciation to the Computational Research Center (HPC-Linux cluster) at UND for providing the computer resources I needed to complete my projects.

I would like to thank my family, especially my parents, for their love and continual support not only throughout college, but also through life. Thank you for letting me go explore the world to find my place.

Finally, my special thanks go to my beloved husband, Sylvester V. Popis, for being my beacon of light in times of darkness. Thank you for going through all the ups and downs of life with me and never leaving my side. You often joke that I am directionally challenged, and you are right. If I hadn't met you, I would have been lost in this big world. Thank you for teaching me how to program in C, C++, and Python, helping me build the machine learning algorithm, and supporting me through all my research projects. Thank you for the countless nights you stayed up with me when I had to study or finish my schoolwork. Thank you for believing in me and encouraging me to pursue my dreams. You are my greatest partner, my dearest husband, and my best friend.

ABSTRACT

Computational electronic structure theory has become an inexorable engine for understanding and even predicting the properties of novel molecules and materials. In this dissertation, two types of novel metal-containing systems, one a material and one a molecule, were examined using *ab initio* methods. In addition, progress on using machine learning (ML) to systematize the selection of qualitatively correct descriptions of molecular systems were examined.

The ever-increasing demand for smaller, faster, and cheaper electronics has fueled the ongoing search for new materials. Silicene, a two-dimensional (2D) monolayer of silicon (Si) atoms arranging in a honeycomb lattice, has attracted much attention because of its compatibility with the current Si-based technologies. To enrich the properties of silicene, transition metals (TMs) are often integrated into the silicene network. Binary monolayers of Si with different TMs are known as TM silicides. By using density functional theory (DFT) calculations, the structural, electronic, and mechanical properties of iridium (Ir)-silicide monolayers were investigated. Different plausible 2D structures of Ir-Si with various atomic ratios were modelled and the cohesive energies were then calculated for the geometry optimized structures with the lowest equilibrium lattice constants. Among a large number of candidate structures, we identified several mechanically (via elastic constants and Young's modulus), dynamically (via phonon calculations) and thermodynamically stable Ir-Si monolayer structures. Ir₂Si₄ (called IrSi₂) with a rectangular lattice (Pmmn space group) had the lowest cohesive energy of

−0.248 eV (per IrSi₂ unit) with respect to bulk Ir and bulk Si. The band structure suggested that metallic properties could be detected within Ir₂Si₄ monolayer. Hexagonal (P-3m1) and tetragonal (P4/nmm) cell structures were also found to be stable structures with 0.12 and 0.20 eV (per formula unit) higher cohesive energies, respectively. The interactions of stable Ir-Si monolayers with O₂ and H₂O molecules were also investigated. We found that Ir-Si monolayers are reactive to these molecules.

The search for new materials does not stop at Earth. Many astrophysical molecules have been detected and studied in recent years. Alkaline earth metal monohydroxide radicals, especially calcium monohydroxide (CaOH) and strontium monohydroxide (SrOH), have attracted much attention due to their expected presence on rocky exoplanets, and by their potential applications in laser cooling and trapping technologies. Since samples of these interstellar molecules are not easily accessible, it is very challenging to study them using experimental methods. Theoretical approaches often become the more viable option, especially for providing detailed insights into the mechanisms of formation and dissociation of these radicals. Multireference perturbation theory (MRPT) methods are better alternatives to DFT for studying these electronic structures because a carefully balanced dynamical and non-dynamical (or static) electron correlations, starting from multiconfigurational self-consistent field (MCSCF), is needed. The second-order generalized van Vleck perturbation theory (GVVPT2), one of the MRPT approaches, was utilized to study CaOH and SrOH monomers. The dimerization of CaOH was also considered. The optimized geometry parameters of the ground state CaOH monomer as well as the vertical excitation energy of the first low-lying excited state are in good agreement with other *ab initio* methods and experimental data. On the other hand, the

optimized geometry of the ground state of SrOH appears to be quasilinear as opposed to the linear geometry described in published literature. In addition, by applying relativistic corrections, the GVVPT2 optimized geometry of SrOH became more bent by approximately 6° .

The biggest challenge of MRPT methods is to find a proper active space which is unique for each electronic structure and heavily dependent on user's choice. If the active space is too big, the computational cost may be prohibitively expensive. If the active space is too small, the chemical properties of the structure may not be described appropriately, leading to inaccurate results. Hence, an improvement to these methods is much needed. Recently, ML has entered and is revolutionizing the quantum chemistry field. With the ability to automatically process a large amount of data and improve through experience, ML offers a solution to the user-specified active space problem of MRPT methods. This means that studying challenging and extensive chemical systems could become feasible in the near future while maintaining the accuracy of the underlying methods. In this study, we built our ML protocol to find a list of feasible active space configurations to be starting inputs for the GVVPT2 method. By implementing the reinforcement learning algorithm within ML, the machine was allowed to explore the unknown dynamical environment of the input chemical systems and receive feedback for each action it took. As a result, the machine gradually learned how to choose a proper active space. So far, we have used our ML algorithm to find the active space of the ground state water, triplet ground state methylene, and stretched water model systems. Good starting point active space configurations were found for all these three molecules which confirmed the active space selection ability of our ML model.

CHAPTERS

I. INTRODUCTION

Theoretical and Computational Chemistry

There are many important chemistry problems which cannot be solved by experimental methods alone. This has fueled the rapid evolution of theoretical and computational chemistry over the last century to provide complementary alternatives for studying a variety of challenging chemical systems, such as transition-metal complexes,¹⁻³ organometallic substances,⁴⁻⁶ semiconductors,⁷⁻¹⁰ and biological molecules.^{11,12} The developments of all of the theoretical approaches have centered around one core problem, which is to find a sufficiently accurate description of the electrons and nuclei contained in the chemical systems of interest.^{13,14} Regrettably, only one-electron models, such as the hydrogen atom and the molecular hydrogen cation H_2^+ , can be described and solved exactly with the Schrödinger equation.^{14,15} For many-body problems which involve numerous electron interactions, different types of approximations have to be developed to include electron correlations as close to the ones in the real systems as possible, from both a technical perspective and considering available computer resources.^{14,16,17}

The Hartree–Fock (HF) approximation¹⁸⁻²⁰ is one of the first approaches which was introduced to solve many-body problems.²¹ HF uses an electron wave function in the form of a single Slater determinant²⁰ to turn the many-body time-independent Schrödinger equation into many single-particle equations.^{21,22} By using the mean-field approach in

which each electron moves in an average field made up of the remaining electrons, HF cannot compute electron correlations with sufficient accuracy for nearly all practical applications.^{22,23} Many post-HF methods, such as single-reference approaches (e.g., configuration interaction (CI),²⁴⁻²⁷ second-order Møller–Plesset perturbation theory (MP2),²⁸ and single-reference coupled cluster (CC)²⁹), and multireference approaches (e.g., multireference CI (MR-CI),^{24,25,30,31} multireference perturbation theory (MRPT),³²⁻³⁶ multiconfigurational self-consistent field (MCSCF),^{31,37,38} and multireference CC (MR-CC)^{39,40}), have been developed to give better descriptions of correlation effects. However, maintaining a balance between accuracy and computational cost for these post-HF methods is a challenge in itself.

Another popular method that belongs in the first-principles or *ab initio* methods with the wave function theory (WFT) approaches mentioned above is density functional theory (DFT).⁴¹⁻⁴⁷ While the HF and post-HF methods employ electron wave functions, DFT uses electron density instead.^{45,48} A tremendous effort has been put in the derivation of density functionals to calculate the electron correlation effects in DFT, since the true density functional is in general unknown except for certain model problems. In 2017, a total of 200 exchange-correlation functionals were benchmarked.⁴⁶ Since DFT is computationally efficient and can provide reasonably accurate results for many chemical systems containing a large number of electrons, DFT has become a widely-used method in solid-state physics and quantum chemistry.^{46,49,50}

Despite the great balance between accuracy and computational cost that DFT offers, DFT is not necessarily a good fit for studying systems of more than 1,000 atoms.^{23,51,52} Semi-empirical methods (e.g., Modified Neglect of Diatomic Overlap

(MNDO),⁵³ Austin Model 1 (AM1),⁵⁴ and Parametric Method 3 (PM3)^{55,56}) and molecular mechanics (MM) methods (or force field methods) (e.g., MM2⁵⁷ and Assisted Model Building with Energy Refinement (AMBER)⁵⁸) have become the methods of choice for studying large organic molecules and biological systems.^{23,51,59,60} However, DFT, semi-empirical, and force field methods require dispersion corrections because their standard versions do not take van der Waals interactions into account. The D3 method has been shown to improve the accuracy of DFT (i.e., DFT-D3)⁶¹ and quantum mechanics (QM)/MM calculations.⁶¹⁻⁶⁷ For our DFT studies of iridium silicide monolayers presented in chapter III of this dissertation, we used the DFT-D3 method with Becke-Johnson damping⁶⁸ to describe the van der Waals interactions between iridium silicide surfaces and O₂ and H₂O molecules. Becke-Johnson damping helps avoid repulsive interatomic forces at shorter distances and often provides better results for cases of medium-range electron correlations.⁶⁸ In summary, depending on the size of the chemical system of interest, desired level of accuracy, and available computational resources, a proper method needs to be chosen. Since the *ab initio* methods like HF, post-HF, and DFT are more suited for studying our targeted systems, the methodology chapter of the dissertation will focus on these methods.

Theoretical Studies of Two-Dimensional Materials

Technology is the heart and soul of our modern world. To keep up with the fast-growing rate of technology changes, better electronic components are needed. This demand for more efficient electronics has become the driving force for many scientists to develop new types of materials. The discovery of graphene by Andre Geim and Kostya Novoselov

in 2004^{69,70} has marked the beginning of a new generation of candidates, two-dimensional (2D) materials. Graphene is a monolayer of carbon atoms tightly packed together in a honeycomb lattice (see Figure I-1(a) and 1(b)).⁷⁰ Its high charge carrier mobility is the key factor in developing graphene's potential electronics applications.⁷⁰⁻⁷⁴ However, for a direct integration to the existing silicon-based technologies, graphene might not be the best contender.⁷⁵

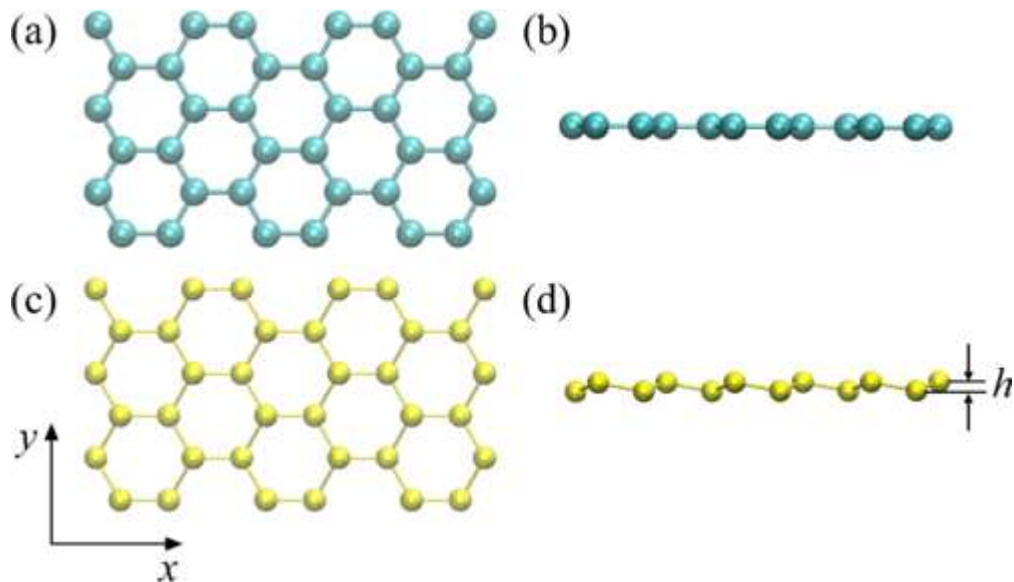


Figure I-1. Comparison of the crystal structures between (a) top view and (b) side view of graphene and (c) top view and (d) side view of silicene. The graphene has a perfect planar structure, while silicene possesses a slightly out-of-plane buckling structure (h denotes the buckling distance). (Image taken from Ref.⁷⁶)

Silicene,⁷⁷⁻⁷⁹ a silicon-based equivalent of graphene, on the other hand, suggests a high compatibility with the present semiconductor technologies.^{75,80,81} Theoretical calculations have shown that similar to graphene, free-standing silicene exhibits extremely high charge carrier mobility,^{60,61,69} topological Dirac insulator characteristics,⁸⁴⁻⁸⁷ and quantum spin and anomalous Hall effects.⁸⁸⁻⁹² Experiments have shown that silicene can

grow epitaxially on various substrates such as Ag(111),^{79,93–97} Ir(111),⁹⁸ ZrB₂(0001),⁹⁹ MoS₂,¹⁰⁰ ZrC(111),¹⁰¹ and Au(111) surfaces.¹⁰² However, in contrast to graphene, silicene has highly reactive buckled hexagonal structures (see Figure I-1(c) and 1(d)), resulting in strong orbital hybridization between silicene and these metal atoms.^{103,104} Consequently, the electronic properties of silicene drastically changed on these metallic substrates.^{103,104} To weaken the interactions between silicene and these metal atoms in order to preserve the novel properties of silicene, alkali metals can be intercalated between silicene and the metal surfaces.¹⁰³

This has inspired many research groups to integrate a variety of metals, especially transition metals (TMs), into the silicene network with the intention of enriching the properties of silicene further. A new family of 2D nanomaterials, called transition metal (TM) silicides, has emerged. Many TM silicides, binary monolayers of Si with different TMs, have been investigated using *ab initio* methods and have shown promising applications in spintronic and magnetic electronic devices.^{105–113}

Chapter III of this dissertation describes our published work in studying iridium silicide (Ir-Si) monolayers.¹¹⁴ By using DFT methods, we modelled different plausible structures of Ir-Si monolayers and calculated cohesive energies on the geometry optimized structures.¹¹⁴ Subsequently, phonon dispersions, band structures, density of states, and mechanical analyses were computed on the stable structures to assess their physical and chemical properties.¹¹⁴

Theoretical Studies of Astrophysical Molecules

Space is vast and complex. Despite all the time and resources that are directed towards space exploration programs, much of space remains a mystery to humanity. Could it be that the answer to our search for better types of materials can be found in space? Up to now, more than 200 astrophysical molecules have been detected in various environments like planetary atmospheres, circumstellar envelopes, protoplanetary disks, and interstellar medium.^{115,116} These molecules contain several different elements with a variety of size and charge.¹¹⁶ Hence, studying astrophysical environments could help discover new molecules, leading to a better understanding of the types of matter that made up the universe, and possible ways to advance life on Earth.

Astronomical observations and spectroscopic detection are one thing, collecting samples for experimentation is quite another. Even for planets and regions that are relatively close to Earth, launching a space probe to collect samples is without a doubt expensive and time-consuming. For instance, the NASA Cassini-Huygens mission launched in 1997 was a long two-decade journey to planet Saturn and its moons.^{117,118} The cost of the mission was about \$3.9 billion.¹¹⁹ Therefore, samples of astrophysical molecules are certainly not easy to access and preserve. While there have been significant advances in the laboratory synthesis and characterization of molecules of astrophysical interest^{120–124}, some molecules have proven difficult to study via so-called laboratory astrophysics. Moreover, even for molecules that can be synthesized in conditions similar to space, they are often difficult to fully characterize.

Over the years, theoretical methods have helped overcome this limitation. Computational modelling and theoretical calculations have made it possible to study highly

reactive and short-lived astrophysical radicals and ions.^{115,125} Theoretical approaches also help make predictions for additional characteristics of these species like emission spectra, rotational constants, and possible mechanisms of their formation and dissociation.^{23,115,116} This helps develop new technologies on Earth, such as inertial confinement fusion^{126,127} and laser cooling.^{128,129} Theoretical methods have become valuable assets in the field of astrophysics and astrochemistry.

Chapter IV of this dissertation describes our theoretical studies of two astrophysical radicals: calcium monohydroxide (CaOH) and strontium monohydroxide (SrOH) monomers. Aside from their inherent interest as astrophysical molecules, the molecules are of interest as exemplars of systems in which simplified descriptions of chemical bonding (e.g., ionic, covalent) are challenged, and predictions of properties are unusually sensitive to methodology used. Hence, our calculations were performed by using second-order generalized van Vleck perturbation theory (GVVPT2)^{36,130-134} – a variant of the MRPT method, which balances dynamic (e.g., instantaneous) electron correlation with nondynamic (or static) electron correlation which is long-range. Moreover, different electronic states of CaOH have differing mixes of ionic vs. covalent characteristic, hence necessitating the use of methodology that can describe excited electronic states on an even footing with the description of the ground state. GVVPT2 is implemented in our in-house computational chemistry software named UNDMOL,³⁶ which also provides significant flexibility in construction of MCSCF wave functions and has the capability of all-electron, spin-free relativistic methodology. The discussion of CaOH radical is extended to chapter V where our GVVPT2 calculations for the CaOH dimers are presented. One of the motivating factors for examination of CaOH, which had been studied by more

computationally expensive methods, is the validation of the GVVPT2 method for studies of groupings of multiple CaOH monomers for which calculation by the more expensive methods become quickly overwhelming.

Development of Machine Learning in Computational Chemistry

Machine learning (ML) is no longer a futuristic dream. Voice assistants,¹³⁵ image recognition,¹³⁶ intelligent gaming,¹³⁷ autonomous driving,¹³⁸ etc. are all different applications of ML in our daily lives. ML refers to an algorithm in which a machine is given a specific task so that it will automatically improve its task performance through training experiences.¹³⁹ There are three main types of ML methods: supervised learning, unsupervised learning, and reinforcement learning.¹³⁹ Supervised learning algorithm uses a set of input variables to train a machine to produce desired outputs.^{139,140} On the other hand, unsupervised learning uses unlabeled data so that the machine can discover underlying patterns within the data set.^{139,141} Reinforcement learning uses rewards as pointers for the machine to figure out which actions to take in an unknown dynamical environment.^{139,142,143} Many current research studies also use hybrid forms of these three learning algorithms,¹³⁹ such as semi-supervised learning^{144,145} and active learning.^{146,147}

With great abilities of ML in processing vast amount of data and yielding optimized outputs, let's imagine all the potential applications that ML could bring to the field of quantum chemistry. In recent years, theoretical chemists and physicists have brought some of these applications into reality, for instance, solving certain electronic structure problems using ML.¹⁴⁸⁻¹⁵¹ ML has been used to predict electron charge density and density of states in DFT, given just atomic configurations of target systems,¹⁵² or to obtain more accurate

levels of theory energies from DFT.¹⁵³ ML has also been making strides in improving multireference methods.^{150,154,155} Although these multireference methods can often provide high level of accuracy for small- to medium-sized chemical systems, their major drawback lies in the difficulty of active space selection procedure.^{150,154} Each electronic structure has a unique active space and requires the user to have great knowledge and experience to make a proper selection.^{150,154} With ML, this limitation can be overcome. The ultimate goal is to establish a universal automatic protocol in selecting complex active space within these multireference methods.

Chapter VI of this dissertation describes how we incorporated ML to solve the user-oriented active space problem within GVVPT2 method. We used a reinforcement learning algorithm, implemented in PyTorch software package,¹⁵⁶ to train the machine to select a proper active space. The machine first explored the unknown environment for each target chemical system. Rewards were then given when it reached certain desired outputs. On the other hand, if the machine chose a wrong way of redistributing the orbitals, resulting in bad active space configurations which did not satisfy certain pre-determined conditions, it would be penalized. Our ML routine was built as a pre-processor program to generate good starting inputs for the GVVPT2 method, which is encoded in the UNDMOL software. The active space selection ability of the ML was evaluated by comparison with well-studied model problems: the case of ground state water, triplet ground state methylene, and stretched water.

Dissertation Framework

This section outlines the structure of the dissertation. The introduction chapter gave an overview of theoretical and computational chemistry along with the methods that were used in theoretical studies of 2D materials and astrophysical molecules. The chapter also highlights recent advances of ML in computational chemistry, and hence, the inspiration to apply ML to our work. Chapter II provides a synopsis of the *ab initio* methods which lay the foundation for our theoretical studies, such as the HF approximation, DFT, MCSCF, MRPT, and its variant, GVVPT2. The spin-free exact two-component method, an approach to study scalar relativistic effects within GVVPT2, will also be discussed there. In addition, the chapter reviews important developments of ML in active space selection within the multireference-multiconfigurational methods. Chapter III presents our theoretical studies of iridium silicide monolayers using DFT. Chapter IV discusses our GVVPT2 studies of CaOH and SrOH monomers. The discussion of CaOH will be continued in chapter V where we show our GVVPT2 calculations for CaOH dimers. In chapter VI, an extensive description of how we incorporated ML to solve the user-oriented active space problem within GVVPT2 will be provided. The chapter also presents the ML's active space selection ability in the case of ground state water, triplet ground state methylene, and stretched water. The final chapter delivers concluding remarks and future directions.

II. METHODS

Time-Independent Schrödinger Equation

The main objective of quantum chemistry is to solve the electronic Schrödinger equation for molecules and molecular ions.¹⁵ The time-independent Schrödinger equation can be written in the form of bra-ket notation as:

$$\hat{H}|\Psi\rangle = E|\Psi\rangle \quad (\text{Eq. II-1})$$

where \hat{H} is the Hamiltonian operator, operating on the wave function $|\Psi\rangle$ of the system of interest to produce the corresponding energy E . The non-relativistic Hamiltonian operator can be written as the sum of the kinetic energy operator, \hat{T} , and potential energy operator, \hat{V} :

$$\hat{H} = \hat{T} + \hat{V} \quad (\text{Eq. II-2})$$

in which

$$\hat{T} = \hat{T}_N + \hat{T}_e = -\sum_{A=1}^{N_N} \frac{1}{2M_A} \nabla_A^2 - \sum_{i=1}^{N_e} \frac{1}{2} \nabla_i^2 \quad (\text{Eq. II-3})$$

and

$$\hat{V} = \hat{V}_{NN} + \hat{V}_{eN} + \hat{V}_{ee} = \sum_{A=1}^{N_N} \sum_{B>A}^{N_N} \frac{Z_A Z_B}{R_{AB}} - \sum_{i=1}^{N_e} \sum_{A=1}^{N_N} \frac{Z_A}{r_{iA}} + \sum_{i=1}^{N_e} \sum_{j>i}^{N_e} \frac{1}{r_{ij}} \quad (\text{Eq. II-4})$$

where \hat{T}_N and \hat{T}_e are the kinetic energy operator of the nuclei and electrons; \hat{V}_{NN} , \hat{V}_{eN} , and \hat{V}_{ee} are the potential energy operator for the interactions between nuclei-nuclei, electron-nuclei, and electron-electron, respectively; N_N and N_e represent the number of nuclei and electrons; ∇_A^2 and ∇_i^2 are the Laplacian operators of nucleus A and electron i ; M_A denotes the ratio of the mass of nucleus A to the mass of an electron, Z_A and Z_B represent the atomic number of nucleus A and nucleus B ; and R_{AB} , r_{iA} , and r_{ij} designate the distances between nucleus A and nucleus B , electron i and nucleus A , and electron i and electron j , respectively.^{157,158}

To simplify the non-relativistic time-independent Schrödinger equation further, Born–Oppenheimer approximation¹⁵⁹ is often applied. In this approximation, due to significant differences between the masses of the nuclei and the electrons, the fast electrons are perceived to be moving in a field of stationary nuclei.^{157,159} As a result, the terms \hat{T}_N and \hat{V}_{NN} can be neglected, and Eq. II-2 becomes:¹⁵⁷

$$\hat{H} = -\sum_{i=1}^{N_e} \frac{1}{2} \nabla_i^2 - \sum_{i=1}^{N_e} \sum_{A=1}^{N_N} \frac{Z_A}{r_{iA}} + \sum_{i=1}^{N_e} \sum_{j>i}^{N_e} \frac{1}{r_{ij}} \quad (\text{Eq. II-5})$$

However, as mentioned in chapter I, the above equation can only be solved exactly for one-electron models.¹⁴ For many-body problems, the term \hat{V}_{ee} that represents the electron-electron interactions turns out to be quite complicated and requires approximations.^{14,16,17}

Hartree–Fock Approximation

One of the first and simplest approaches which was derived to solve many-body electronic problems is the Hartree–Fock (HF) approximation.^{18–20} The N -electron

Hamiltonian operator can be approximated using the form of a single Slater determinant²⁰ of N spin-orbitals $\chi_i(\mathbf{x}_i)$:

$$\Psi(\mathbf{x}_1, \mathbf{x}_2, \dots, \mathbf{x}_N) = \frac{1}{\sqrt{N!}} \begin{vmatrix} \chi_1(\mathbf{x}_1) & \chi_2(\mathbf{x}_1) & \cdots & \chi_N(\mathbf{x}_1) \\ \chi_1(\mathbf{x}_2) & \chi_2(\mathbf{x}_2) & \cdots & \chi_N(\mathbf{x}_2) \\ \vdots & \vdots & \ddots & \vdots \\ \chi_1(\mathbf{x}_N) & \chi_2(\mathbf{x}_N) & \cdots & \chi_N(\mathbf{x}_N) \end{vmatrix} \quad (\text{Eq. II-6})$$

where $\frac{1}{\sqrt{N!}}$ represents the normalization factor and \mathbf{x}_i includes space and spin coordinates of i th electron.¹⁵⁷ Eq. II-6 satisfies the Pauli exclusion principle¹⁶⁰ in which the indistinguishability of electrons is preserved and the requirement for antisymmetric character of the total wave function is met.¹⁵⁷ According to the variational principle, the ideal set of spin orbitals will give us the lowest possible energy, E_0 .^{157,161}

$$E_0 = \langle \Psi_0 | \hat{H} | \Psi_0 \rangle \quad (\text{Eq. II-7})$$

By considering the i th electron to be moving in an average field made up of the remaining electrons, the HF approximation uses the HF potential, $v^{HF}(i)$, which represents the average field of $N - 1$ electrons experienced by the i th electron.¹⁵⁷ Thus, the one-electron Hamiltonian operator is:

$$\hat{f}_i = -\frac{1}{2} \nabla_i^2 - \sum_{A=1}^{N_N} \frac{Z_A}{r_{iA}} + v^{HF}(i) = h(i) + v^{HF}(i) \quad (\text{Eq. II-8})$$

where the Fock operator, \hat{f}_i , is an effective one-electron operator, and $h(i)$ includes the kinetic energy of one electron i and its potential energy due to the interaction between electron i and the nuclei.¹⁵⁷ Let's choose the i th electron to be electron 1 in the set of spin-orbitals, χ_i , then we have:^{157,162}

$$\hat{f}_1 \chi_i(\mathbf{x}_1) = \varepsilon_i \chi_i(\mathbf{x}_1) \quad (\text{Eq. II-9})$$

or

$$[h(\mathbf{x}_1) + v^{HF}(\mathbf{x}_1)]\chi_i(\mathbf{x}_1) = \varepsilon_i\chi_i(\mathbf{x}_1) \quad (\text{Eq. II-10})$$

The term $v^{HF}(\mathbf{x}_1)$ can be expanded in terms of the Coulomb operator, $J_j(\mathbf{x}_1)$, and the exchange operator, $K_j(\mathbf{x}_1)$. Hence, Eq. II-10 becomes:^{48,157}

$$\left[h(\mathbf{x}_1) + \sum_{j \neq i} J_j(\mathbf{x}_1) - \sum_{j \neq i} K_j(\mathbf{x}_1) \right] \chi_i(\mathbf{x}_1) = \varepsilon_i\chi_i(\mathbf{x}_1) \quad (\text{Eq. II-11})$$

Based on the types of spin orbitals – restricted or unrestricted, HF method can be categorized as either restricted HF (RHF) or unrestricted HF (UHF).¹⁵⁷ While UHF employs different spatial functions for a spin-up α and a spin-down β , RHF uses the same spatial function as shown below:¹⁵⁷

$$\chi_i(\mathbf{x}) = \begin{cases} \psi_i(\mathbf{r})\alpha(\omega) \\ \psi_i(\mathbf{r})\beta(\omega) \end{cases} \quad (\text{Eq. II-12})$$

where ψ_i represents the spatial function for the spin orbital χ_i , and \mathbf{r} and ω indicate the space and spin coordinates of the electrons, respectively. Within RHF, the spin functions $\alpha(\omega)$ and $\beta(\omega)$ can often be integrated out, and the spatial molecular orbitals (MOs) ψ_i written as a linear combination of atomic orbitals (AOs) as follows:

$$\psi_i = \sum_{\mu=1}^n C_{\mu i} \phi_{\mu} \quad (\text{Eq. II-13})$$

in which $C_{\mu i}$ represents the coefficient for the μ th AO basis function, ϕ_{μ} , with n is the total number of basis functions in the basis set, the HF equation that appeared in Eq. II-9 turns out to be:^{157,163}

$$\hat{f}_1 \sum_{\mu=1}^n C_{\mu i} \phi_{\mu}(\mathbf{x}_1) = \varepsilon_i \sum_{\mu=1}^n C_{\mu i} \phi_{\mu}(\mathbf{x}_1) \quad (\text{Eq. II-14})$$

Eq. II-14 usually appears in the compact form of Roothaan-Hall matrix equation:^{163,164}

$$\mathbf{FC} = \boldsymbol{\varepsilon}\mathbf{SC} \quad (\text{Eq. II-15})$$

where \mathbf{F} symbolizes the matrix representation of the Fock operator; \mathbf{C} is a square matrix of the expansion coefficients, $C_{\mu i}$; \mathbf{S} denotes the overlap matrix between the basis functions; and $\boldsymbol{\varepsilon}$ is the diagonal matrix containing the orbital energies, ε_i .

Because the HF approximation is a mean-field method, the N -electron wave function needs to be solved iteratively using a self-consistent field (SCF) method.^{21,157} This means an initial guess of MOs needs to be established in order to calculate the term v^{HF} included in the Fock operator. By solving the Roothaan-Hall matrix equation, a new set of MOs can be obtained. The process needs to be repeated until the new set of MOs is not different than the one found in the previous iteration within a certain margin of error, in which we say self-consistency has been reached.¹⁵⁷ As mentioned in Chapter I, the accuracy level of HF method is not sufficient for most practical applications. However, HF can provide a decent starting guess for post-HF calculations which are generally much more computationally expensive. For the work described in this dissertation, we used RHF to generate the starting MOs to help reduce the computational cost for our post-HF calculations.

Density Functional Theory

The story of density functional theory (DFT) began with Thomas-Fermi theory in 1926.^{165,166} The theory used electron density of a uniform electron gas to solve the Schrödinger equation, but unfortunately, it could not describe characteristics of chemical bonds in molecules accurately.^{49,50,165-167} In 1964, Hohenberg and Kohn⁴¹ introduced two theorems; theorem I states that the external potential, $V_{ext}(\mathbf{r})$, and thus the total energy is

a unique functional of the electron density, $\rho(\mathbf{r})$; and theorem II embodies the variational principle wherein the lowest total energy can only be obtained with the true electron density.^{48–50,168} Hohenberg–Kohn (HK) theorems led to a method called orbital-free DFT.^{49,169,170} However, this method lacks the ability to calculate electronic energies for many electronic problems.^{49,50} In 1965, Kohn and Sham⁴² proposed an alternative approach to overcome the limitations of the orbital-free DFT.^{45,48} This approach has turned into the most widely-used version of DFT known as Kohn–Sham (KS)-DFT or just DFT as many researchers prefer to call it.^{46,49,50} The DFT method used in our work in this dissertation is KS-DFT, which we will also call DFT for short.

Similar to HF theory, DFT is a mean-field method in which one electron is considered to be moving in the average field made up of all other electrons.²² However, instead of using electron wave functions, DFT uses electron density, $\rho(\mathbf{r})$.^{45,48} By using KS orbitals, a system of many interacting electrons is converted into a fictitious system of non-interacting electrons in a way that the one-electron density, $\rho(\mathbf{r})$, is the same for both interacting and non-interacting systems.¹⁷¹ The one-electron density, $\rho(\mathbf{r})$, is given by:^{171,172}

$$\rho(\mathbf{r}) = \sum_{p=1}^N |\phi_p(\mathbf{r})|^2 \quad (\text{Eq. II-16})$$

Because the KS orbitals are obtained using a Slater determinant, the fermionic character of the wave function is preserved to a greater extent than orbital-free DFT and becomes applicable to many chemical systems. The electronic energy of the target system can then be described in terms of the non-interacting kinetic energy, T_S , of the one-electron KS orbitals, $\phi_p(\mathbf{r})$; the external energy (or electron-nuclei attraction energy), $V_{ext}[\rho(\mathbf{r})]$; the

Hartree (or Coulomb) energy, $E_H[\rho(\mathbf{r})]$; and the exchange–correlation (XC) energy, $E_{XC}[\rho(\mathbf{r})]$, as shown below:^{45,151,156}

$$E = T_S[\phi_p(\mathbf{r})] + V_{ext}[\rho(\mathbf{r})] + E_H[\rho(\mathbf{r})] + E_{XC}[\rho(\mathbf{r})] \quad (\text{Eq. II-17})$$

To find the electronic energy of the target system, the KS equation:⁴²

$$\left(-\frac{1}{2}\nabla_p^2 + v_S(\mathbf{r})\right)\phi_p(\mathbf{r}) = \varepsilon_p\phi_p(\mathbf{r}) \quad (\text{Eq. II-18})$$

needs to be solved self-consistently.⁴⁹ The effective KS potential, $v_S(\mathbf{r})$, is the sum of the external potential, $v_{ext}(\mathbf{r})$; the Hartree potential, $v_H(\mathbf{r})$; and the XC potential, $v_{XC}(\mathbf{r})$, as follows:^{42,167,171,172}

$$v_S(\mathbf{r}) = v_{ext}(\mathbf{r}) + v_H(\mathbf{r}) + v_{XC}(\mathbf{r}) \quad (\text{Eq. II-19})$$

where:

$$v_{ext}(\mathbf{r}) = -\sum_{M=1}^{N_{nuc}} \frac{Z_M}{r_{pM}} \quad (\text{Eq. II-20})$$

(N_{nuc} : number of nuclei; Z_M : the atomic number of nucleus M ; r_{pM} : the distance between electron p and nucleus M), and

$$v_H(\mathbf{r}) = \int d\mathbf{r}' \frac{\rho(\mathbf{r}')}{|\mathbf{r} - \mathbf{r}'|} \quad (\text{Eq. II-21})$$

and

$$v_{XC}(\mathbf{r}) = \frac{\delta E_{XC}[\rho(\mathbf{r})]}{\delta \rho(\mathbf{r})} \quad (\text{Eq. II-22})$$

The SCF routine¹⁷³ for solving KS equation starts with an initial electron density used to calculate the KS potential, which in turn generates a new electron density. The process is repeated until there is a negligible difference between the new electron density and the one in the previous iteration which means self-consistency has been reached.

Although DFT is a mean-field method, it is an exact theory in principle because if an exact XC functional was used, an exact electronic energy would be acquired.^{22,48} Unfortunately, the exact XC functional is unknown, and therefore, many approximate XC functionals have emerged based on experimental data or computationally modelled systems.⁴⁸ These approximate XC functionals are defined based on the exchange-energy functional, E_X , and the correlation-energy functional, E_C , in a sum relationship as shown below:¹⁷¹

$$E_{XC} = E_X + E_C \quad (\text{Eq. II-23})$$

There are three commonly used types of XC functionals: local functionals, gradient-corrected functionals, and hybrid functionals.⁴⁸ Local functionals such as the local density approximation (LDA) and local spin density approximation (LSDA) are XC functionals of only electron density, ρ .^{50,171} Within LDA, the correlation part, E_C , is calculated based on Vosko–Wilk–Nusair (VWN) parametrization,¹⁷⁴ and the exchange part, E_X , can be expressed as:¹⁷¹

$$E_X^{LDA} = -\frac{3}{4} \left(\frac{3}{\pi} \right)^{1/3} \int [\rho(\mathbf{r})]^{4/3} d\mathbf{r} \quad (\text{Eq. II-24})$$

For LSDA, E_C can be computed based on either VWN5,^{174,175} Perdew–Zunger 1981 (PZ81),¹⁷⁶ or Perdew–Wang 1992 (PW92)¹⁷⁷ parametrizations; and E_X is calculated using both spin α and β and the uniform (or homogeneous) electron gas (UEG) exchange-energy density per unit volume, $e_{x,\sigma}^{UEG}$.⁴⁶

$$E_X^{LSDA} = \sum_{\sigma}^{\alpha,\beta} \int e_{x,\sigma}^{UEG} d\mathbf{r} = -\frac{3}{2} \left(\frac{3}{4\pi} \right)^{1/3} \sum_{\sigma}^{\alpha,\beta} \int \rho_{\sigma}^{4/3} d\mathbf{r} \quad (\text{Eq. II-25})$$

The XC functionals implemented in LDA and LSDA were derived from UEG, so they are not accurate enough for molecular systems which involve inhomogeneous electron density distributions.^{46,171}

Gradient-corrected functionals like generalized gradient approximation (GGA) are derived with inclusion of the density gradient, $\nabla\rho$, to overcome the UEG limitations of LDA and LSDA.^{46,50} The exchange functional, E_X , for GGA often appears in the general form given below:

$$E_X^{GGA} = \sum_{\sigma} \int e_{x,\sigma}^{UEG} g_{x,\sigma}^{GGA} d\mathbf{r} \quad (\text{Eq. II-26})$$

where $g_{x,\sigma}^{GGA}$ is the inhomogeneity correction factor (ICF).⁴⁶ The ICF takes on different forms in different exchange functionals.⁴⁶ Becke 1988 (B88),¹⁷⁸ Perdew–Wang 1991 (PW91),¹⁷⁹ and Perdew–Burke–Ernzerhof (PBE)¹⁸⁰ are among the most well-known GGA exchange functionals. The mainstream GGA correlation functionals include Perdew 1986 (P86),¹⁸¹ Lee–Yang–Parr (LYP),¹⁸² PW91,¹⁷⁹ and PBE.¹⁸⁰ Meta-GGA functionals are another type of gradient-corrected functionals, but they improve upon GGA by using second derivatives of the electron density, such as the kinetic energy density, τ ,^{46,50} or Laplacian.

Hybrid functionals are XC functionals which mix in the HF exchange (or exact exchange) component, E_X^{HF} .⁵⁰ For example, the most popular global hybrid GGA density functional B3LYP (B88 + three parameters¹⁸³ + LYP) can be described as follows:

$$E_{XC}^{B3LYP} = E_{XC}^{LDA} + a_1(E_X^{HF} - E_X^{LDA}) + a_2\Delta E_X^{B88} + a_3(E_C^{LYP} - E_C^{VWN-LDA}) \quad (\text{Eq. II-27})$$

in which $a_1 = 0.20$, $a_2 = 0.72$, and $a_3 = 0.81$ represent the mixing ratio.⁵⁰ The global hybrid density functionals are often used for calculations of molecular properties because the descriptions of bond interactions and kinetics are improved significantly by the HF exchange part.⁴⁶ In order to compare the accuracy level of hybrid functionals with the local and gradient-corrected functionals, one could look at Perdew's metaphorical Jacob's Ladder¹⁸⁴ illustrated in Figure II-1 in which the accuracy increases as we go up the ladder.

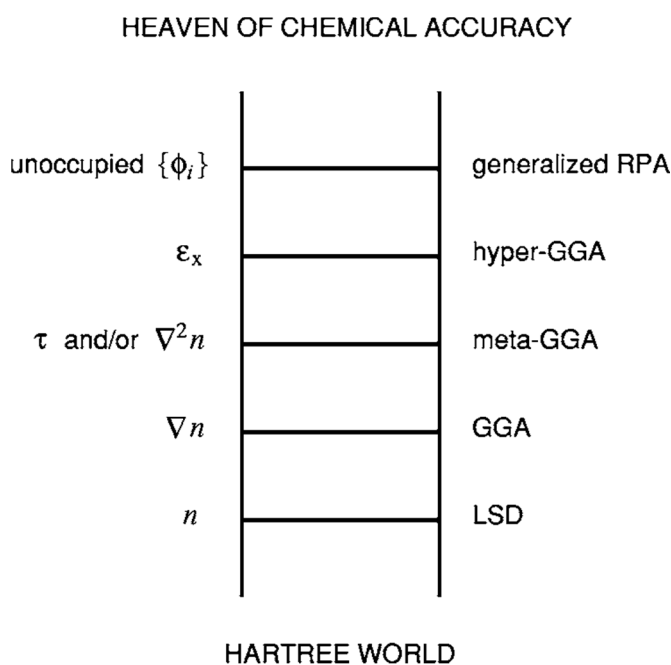


Figure II-1. Perdew's metaphorical Jacob's Ladder of XC functionals. (Image taken from Ref.¹⁸⁴)

A significant number of density functionals (up to 200 functionals in 2017)⁴⁶ has been derived to calculate the XC effects in DFT. Due to a great balance between level of accuracy and computational cost, DFT has become the dominant method for studying ground-state molecules and solids.^{46,49,50} That is the reason why we employed DFT in our theoretical studies of iridium silicide monolayers which will be discussed further in chapter

III. However, instead of using coordinate-space representations as described above, we used momentum-space functions called plane waves in our calculations. Plane wave DFT is more suited for studies of solid states because solids often have repeated arrangements of atoms, molecules, or ions, and plane waves can describe the periodicity of crystal lattices through periodic boundary conditions¹⁸⁵ and Bloch's theorem.¹⁸⁶ Periodic boundary conditions help simulate a large lattice by using a periodic lattice of identical unit cells.¹⁸⁵ The unit cells, after being translated through lattice vectors: $\mathbf{R} = n_1\mathbf{a}_1 + n_2\mathbf{a}_2 + n_3\mathbf{a}_3$ (n_1 , n_2 , and n_3 are integers, and \mathbf{a}_1 , \mathbf{a}_2 , and \mathbf{a}_3 are primitive translation vectors of the crystal lattice), fill the lattice space without any gaps or overlapping.¹⁸⁷ As seen in Figure II-2, the basis contains two different ions (2(b)) and each basis occupies one lattice point in 2(a) to make up the crystal structure in 2(c).

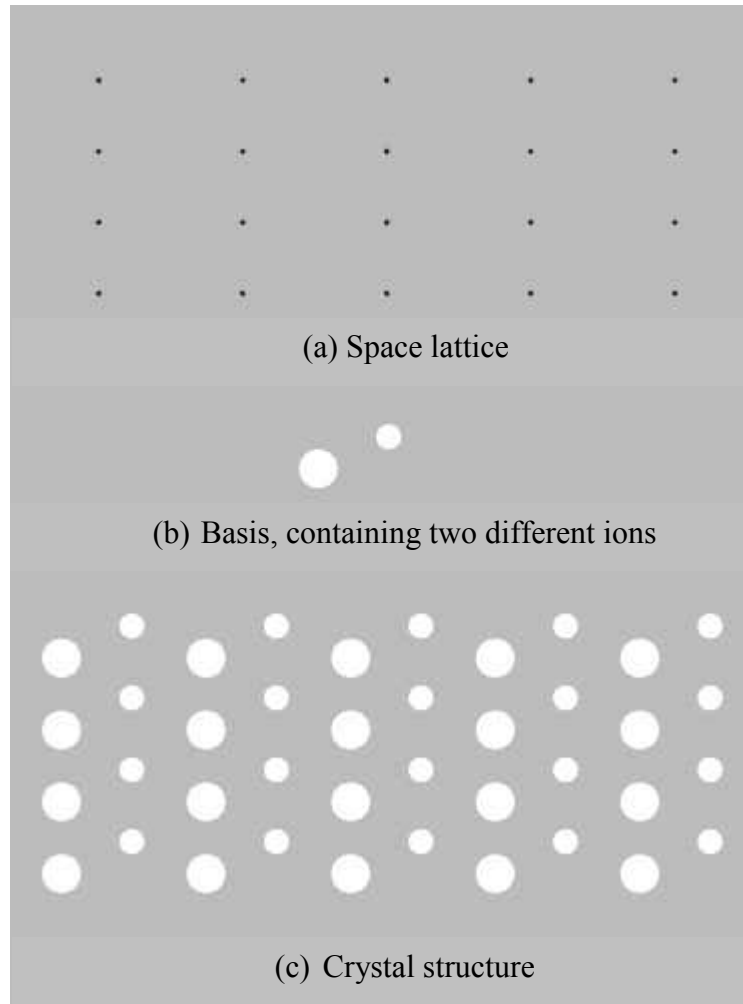


Figure II-2. The crystal structure (c) is form by the basis (b) occupying each lattice point of the space lattice (a). (Image taken from Ref.¹⁸⁷)

The lattice described above exists in real space and is called direct lattice. By applying Fourier transform, the direct lattice is transformed into a reciprocal lattice which exists in reciprocal space or momentum space.¹⁸⁷ The form of a reciprocal lattice vector is:

$$\mathbf{G} = \nu_1 \mathbf{b}_1 + \nu_2 \mathbf{b}_2 + \nu_3 \mathbf{b}_3 \quad (\text{Eq. II-28})$$

where ν_1 , ν_2 , and ν_3 are integers, and \mathbf{b}_1 , \mathbf{b}_2 , and \mathbf{b}_3 are primitive translation vectors of the reciprocal lattice which are defined as below:

$$\mathbf{b}_1 = 2\pi \frac{\mathbf{a}_2 \times \mathbf{a}_3}{\mathbf{a}_1 \cdot (\mathbf{a}_2 \times \mathbf{a}_3)} \quad (\text{Eq. II-29})$$

$$\mathbf{b}_2 = 2\pi \frac{\mathbf{a}_3 \times \mathbf{a}_1}{\mathbf{a}_1 \cdot (\mathbf{a}_2 \times \mathbf{a}_3)} \quad (\text{Eq. II-30})$$

$$\mathbf{b}_3 = 2\pi \frac{\mathbf{a}_1 \times \mathbf{a}_2}{\mathbf{a}_1 \cdot (\mathbf{a}_2 \times \mathbf{a}_3)} \quad (\text{Eq. II-31})$$

and the choice of \mathbf{b}_1 , \mathbf{b}_2 , and \mathbf{b}_3 needs to satisfy the orthogonality condition:

$$\mathbf{b}_i \cdot \mathbf{a}_j = 2\pi \delta_{ij} \quad (\text{Eq. II-32})$$

in which $\delta_{ij} = 1$ if $i = j$ and $\delta_{ij} = 0$ if $i \neq j$.¹⁸⁷ Since the lattice is periodic, the plane wave, $e^{i\mathbf{G}\cdot\mathbf{r}}$, will have the periodicity of the lattice:¹⁸⁷

$$e^{i\mathbf{G}\cdot(\mathbf{r}+\mathbf{R})} = e^{i\mathbf{G}\cdot\mathbf{r}} \quad (\text{Eq. II-33})$$

Based on Bloch's theorem,¹⁸⁶ the solutions to the Schrödinger equation in a periodic potential have the form of a plane wave, $e^{i\mathbf{k}\cdot\mathbf{r}}$, transformed by the periodic function of the lattice, $u_{n,\mathbf{k}}(\mathbf{r})$:

$$\psi_{n,\mathbf{k}}(\mathbf{r}) = e^{i\mathbf{k}\cdot\mathbf{r}} u_{n,\mathbf{k}}(\mathbf{r}) \quad (\text{Eq. II-34})$$

where

$$u_{n,\mathbf{k}}(\mathbf{r} + \mathbf{R}) = u_{n,\mathbf{k}}(\mathbf{r}) \quad (\text{Eq. II-35})$$

and $\psi_{n,\mathbf{k}}(\mathbf{r})$ is the wave function with n being the band index and \mathbf{k} is the Bloch vector or momentum vector. Due to the periodicity of the lattice, we have:

$$\psi_{n,\mathbf{k}}(\mathbf{r} + \mathbf{R}) = e^{i\mathbf{k}\cdot\mathbf{R}} \psi_{n,\mathbf{k}}(\mathbf{r}) \quad (\text{Eq. II-36})$$

The plane wave expansion of KS states is given by:

$$\psi_{n,\mathbf{k}}(\mathbf{r}) = \frac{1}{\sqrt{\Omega}} \sum_{\mathbf{G}} c_{\mathbf{G}n\mathbf{k}} e^{i(\mathbf{k}+\mathbf{G})\cdot\mathbf{r}} \quad (\text{Eq. II-37})$$

where $\frac{1}{\sqrt{\Omega}}$ is the normalization constant and $c_{\mathbf{G}n\mathbf{k}}$ represents the expansion coefficients. The electron density, $\rho(\mathbf{r})$, is also expanded using the plane waves:

$$\rho(\mathbf{r}) = \sum_{\mathbf{G}} \rho_{\mathbf{G}} e^{i\mathbf{G}\cdot\mathbf{r}} \quad (\text{Eq. II-38})$$

In practice, the size of plane wave basis sets is limited by the kinetic energy cutoff, E_{cutoff} :

$$\frac{1}{2} |\mathbf{k} + \mathbf{G}|^2 < E_{\text{cutoff}} \quad (\text{Eq. II-39})$$

For most chemical systems, there are two distinguishable regions in a valance wavefunction: atomic core region and interstitial region (see Figure II-3).¹⁸⁸ Since the core region often exhibits strong oscillations, large plane wave basis sets are needed to describe this region accurately.^{188,189} The use of pseudopotentials^{190–198} replaces the Pauli repulsion effects between the core electrons and the nucleus with an effective potential, and therefore, reduces the number of basis functions required.¹⁸⁹ However, the characteristics of wave functions and charge densities near the nucleus are not included in the pseudopotentials.¹⁸⁹ On the other hand, augmented plane wave (APW) method^{199–201} uses atom-like partial waves to describe the atomic core region and envelop functions to describe the interstitial or bonding region. The projector augmented wave (PAW) method^{189,202–205} is a generalization of the APW method and is combined with the pseudopotential approach.

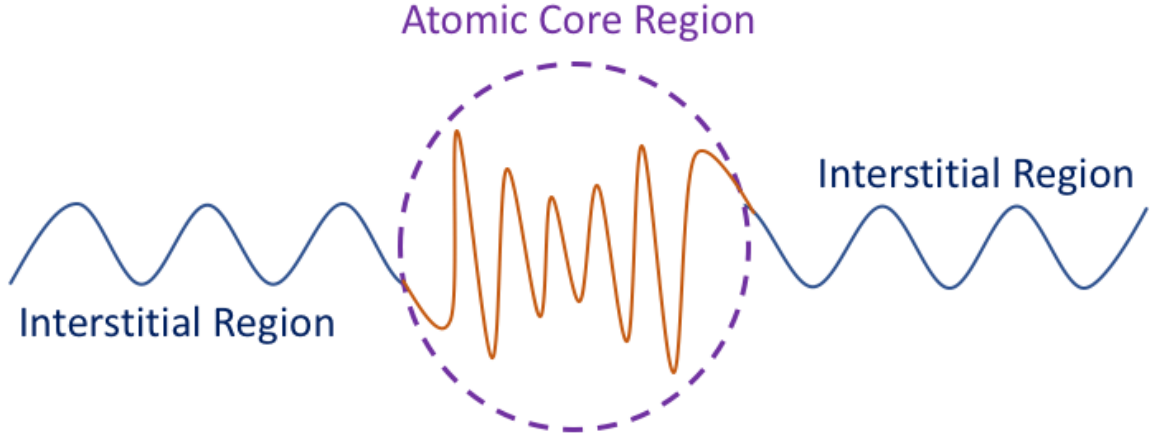


Figure II-3. Illustration of the atomic core and interstitial regions in a valence wavefunction. (Image taken from Ref.¹⁸⁸)

The PAW method uses a linear transformation \mathcal{T} to map the true KS one-particle wave functions, $|\Psi_i\rangle$, onto the auxiliary (or pseudo) wave functions, $|\tilde{\Psi}_i\rangle$:¹⁸⁹

$$|\Psi_i\rangle = \mathcal{T}|\tilde{\Psi}_i\rangle \quad (\text{Eq. II-40})$$

The KS equation is transformed into:¹⁸⁹

$$\mathcal{T}^\dagger \hat{H} \mathcal{T} |\tilde{\Psi}_i\rangle = \varepsilon_i \mathcal{T}^\dagger \mathcal{T} |\tilde{\Psi}_i\rangle \quad (\text{Eq. II-41})$$

Since the transformation \mathcal{T} needs to modify the auxiliary wave functions in the atomic core region, the transformation can be rewritten as identity plus a sum of local, atom-centered contributions, \mathcal{T}_A :^{189,202}

$$\mathcal{T} = 1 + \sum_A \mathcal{T}_A \quad (\text{Eq. II-42})$$

where \mathcal{T}_A only has effects within some augmentation region Ω_A enclosing the atom A . Within Ω_A , the auxiliary wave functions can be expanded into auxiliary partial waves, $|\tilde{\phi}_j^A\rangle$:²⁰²

$$|\tilde{\Psi}_i^A\rangle = \sum_j c_j |\tilde{\Phi}_j^A\rangle \quad (\text{Eq. II-43})$$

where c_j represents the expansion coefficients. By utilizing the same transformation \mathcal{T} ,

$$|\Phi_j^A\rangle = \mathcal{T}|\tilde{\Phi}_j^A\rangle \quad (\text{Eq. II-44})$$

and we have:²⁰²

$$|\Psi_i^A\rangle = \mathcal{T}|\tilde{\Psi}_i^A\rangle = \sum_j c_j |\Phi_j^A\rangle \quad (\text{Eq. II-45})$$

Since the transformation \mathcal{T} is linear, the coefficients, c_j , must be linear functionals of the auxiliary wave functions, $|\tilde{\Psi}_i^A\rangle$, and thus, can be written as:²⁰²

$$c_j = \langle \tilde{p}_j^A | \tilde{\Psi}_i^A \rangle \quad (\text{Eq. II-46})$$

in which $\langle \tilde{p}_j^A |$ are projector functions. There is only one projector function for each auxiliary partial wave, and within Ω_A ,

$$\sum_j |\tilde{\Phi}_j^A\rangle \langle \tilde{p}_j^A | = 1 \quad (\text{Eq. II-47})$$

in order to have one-center expansion $\sum_j |\tilde{\Phi}_j^A\rangle \langle \tilde{p}_j^A | \tilde{\Psi}_i^A$ of an auxiliary wave function to be equal to the auxiliary wave function, $|\tilde{\Psi}_i^A\rangle$, itself.²⁰² This also implies the condition below:^{189,202}

$$\langle \tilde{p}_j^A | \tilde{\Phi}_l^A \rangle = \delta_{jl} \quad (\text{Eq. II-48})$$

Consequently, by using the linear transformation \mathcal{T} :

$$\mathcal{T} = 1 + \sum_j (|\Phi_j^A\rangle - |\tilde{\Phi}_j^A\rangle) \langle \tilde{p}_j^A | \quad (\text{Eq. II-49})$$

the true KS one-particle wave functions, $|\Psi_i^A\rangle$, can be obtained:^{189,202}

$$|\Psi_i^A\rangle = |\tilde{\Psi}_i^A\rangle + \sum_j (|\phi_j^A\rangle - |\tilde{\phi}_j^A\rangle) \langle \tilde{p}_j^A | \tilde{\Psi}_i^A \rangle \quad (\text{Eq. II-50})$$

For our studies of iridium silicide monolayers which will be described further in chapter III, the PAW method was used to simulate interactions between ion cores and valence electrons. The plane wave DFT approach was utilized because iridium silicide monolayers are solids. Both coordinate-space and plane wave DFT methods are used widely in modern computational chemistry. Despite many of DFT's great advantages, DFT often falls short in studying excited states and multiconfigurational electronic structures, in general. Considerable research efforts have been dedicated to developing time-dependent DFT (TD-DFT)^{206–209} and its extensions with the hope of eliminating the shortcomings of DFT. Many successful studies have been reported, but much improvement is still needed.^{48,210–213}

Second-Order Møller–Plesset Perturbation Theory

Møller–Plesset perturbation theory (MPPT)²⁸ is one of the post-HF methods, and was originally derived by Møller and Plesset in 1934. By adding in electron correlation effects through the implementation of Rayleigh–Schrödinger perturbation theory (RSPT),^{15,214} MPPT greatly improves the HF results for situations in which it is valid. The time-independent Hamiltonian, \hat{H} , within RSPT can be written as the sum of the reference Hamiltonian, \hat{H}_0 , and the perturbation term, $\lambda\hat{V}$:

$$\hat{H} = \hat{H}_0 + \lambda\hat{V} \quad (\text{Eq. II-51})$$

in which λ is a real parameter between 0 and 1, signifying the strength of the perturbation.²¹⁵ The case of $\lambda = 0$ results in the zeroth-order of MPPT or the unperturbed problem where:²¹⁶

$$\hat{H} = \hat{H}_0 = \sum_{i=1}^N \hat{f}_i = \sum_{i=1}^N [h(i) + v^{HF}(i)] \quad (\text{Eq. II-52})$$

with N being the total number of electrons. Since \hat{H}_0 can be defined as the sum of Fock operators, \hat{f}_i , as described above, the corresponding zeroth-order energy, $E_m^{(0)}$ (the number in the parenthesis indicates the order of MPPT), can be calculated by solving the eigenvalue problem:^{157,216}

$$\hat{H}_0 |\Psi_m^{(0)}\rangle = E_m^{(0)} |\Psi_m^{(0)}\rangle \quad (\text{Eq. II-53})$$

where

$$E_m^{(0)} = \sum_{i=1}^N \varepsilon_i \quad (\text{Eq. II-54})$$

with ε_i being the orbital energy of the i th electron. For the case of $\lambda \neq 0$ which means there is a perturbation, the perturbed wave function and the perturbed energy of the target system can be expanded using a Taylor series shown in Eq. II-55 and Eq. II-56, respectively:¹⁵⁷

$$|\Psi_m\rangle = |\Psi_m^{(0)}\rangle + \lambda |\Psi_m^{(1)}\rangle + \lambda^2 |\Psi_m^{(2)}\rangle + \dots \quad (\text{Eq. II-55})$$

$$E_m = E_m^{(0)} + \lambda E_m^{(1)} + \lambda^2 E_m^{(2)} + \dots \quad (\text{Eq. II-56})$$

Let's set $\lambda = 1$ to demonstrate the case of full-strength perturbation. The first-order correction to the system energy can be computed using the perturbation operator, $\hat{\mathcal{V}}$.²¹⁶

$$E_m^{(1)} = \langle \Psi_m^{(0)} | \hat{\mathcal{V}} | \Psi_m^{(0)} \rangle \quad (\text{Eq. II-57})$$

in which

$$\hat{V} = \hat{H} - \hat{H}_0 = \sum_{i < j}^N \frac{1}{r_{ij}} - \sum_{i=1}^N v^{HF}(i) \quad (\text{Eq. II-58})$$

The next step is best expressed in terms of square-bracket notations for the one- and two-electron integrals over spin orbitals. But first, it is important to understand the differences between round brackets, angle brackets, and square brackets. The round brackets are used for the one- and two-electron integrals over spatial orbitals as shown below:¹⁵⁷

- One-electron integral:

$$(i|h|j) = \int d\mathbf{r}_1 \psi_i^*(\mathbf{r}_1) h(\mathbf{r}_1) \psi_j(\mathbf{r}_1) \quad (\text{Eq. II-59})$$

- Two-electron integral:

$$(ij|kl) = \int d\mathbf{r}_1 \int d\mathbf{r}_2 \psi_i^*(\mathbf{r}_1) \psi_j(\mathbf{r}_1) \frac{1}{r_{12}} \psi_k^*(\mathbf{r}_2) \psi_l(\mathbf{r}_2) \quad (\text{Eq. II-60})$$

While the angle brackets are used in the physicists' notation, the square brackets are employed in the chemists' notation for the one- and two-electron integrals over spin orbitals. The physicists' notation for the two-electron integral over spin orbitals, χ_i , χ_j , χ_k , and χ_l , is:¹⁵⁷

$$\langle ij|kl \rangle = \int d\mathbf{x}_1 \int d\mathbf{x}_2 \chi_i^*(\mathbf{x}_1) \chi_j^*(\mathbf{x}_2) \frac{1}{r_{12}} \chi_k(\mathbf{x}_1) \chi_l(\mathbf{x}_2) \quad (\text{Eq. II-61})$$

On the other hand, the chemists' notation for the two-electron integral over spin orbitals, χ_i , χ_j , χ_k , and χ_l , is:¹⁵⁷

$$[ij|kl] = \int d\mathbf{x}_1 \int d\mathbf{x}_2 \chi_i^*(\mathbf{x}_1) \chi_j(\mathbf{x}_1) \frac{1}{r_{12}} \chi_k^*(\mathbf{x}_2) \chi_l(\mathbf{x}_2) \quad (\text{Eq. II-62})$$

However, the expressions for the one-electron integral over spin orbitals in both the physicists' and chemists' notations are the same:¹⁵⁷

$$\langle i|h|j\rangle = [i|h|j] = \int d\mathbf{x}_1 \chi_i^*(\mathbf{x}_1) h(\mathbf{r}_1) \chi_j(\mathbf{x}_1) \quad (\text{Eq. II-63})$$

From here on out, the chemists' notation will be used to express the one- and two-electron integrals over spin orbitals. The results of evaluating matrix elements using Slater-Condon rules can be expressed in terms of square-bracket notations for the two-electron integral over spin orbitals, χ_i , χ_j , χ_k , and χ_l .¹⁵⁷

$$\langle \Psi_m^{(0)} | \sum_{i<j}^N \frac{1}{r_{ij}} | \Psi_m^{(0)} \rangle = \frac{1}{2} \sum_{ij} ([ii|jj] - [ij|ji]) \quad (\text{Eq. II-64})$$

and

$$\langle \Psi_m^{(0)} | \sum_{i=1}^N v^{HF}(i) | \Psi_m^{(0)} \rangle = \sum_{ij} ([ii|jj] - [ij|ji]) \quad (\text{Eq. II-65})$$

Then the first-order correction term, $E_m^{(1)}$, can be simplified as:

$$E_m^{(1)} = -\frac{1}{2} \sum_{ij} ([ii|jj] - [ij|ji]) \quad (\text{Eq. II-66})$$

The system energy provided by the first-order Møller–Plesset perturbation theory (MP1) turns out to be the same as the HF energy:²¹⁶

$$\begin{aligned} E_m^{MP1} &= E_m^{(0)} + E_m^{(1)} = \langle \Psi_m^{(0)} | \hat{H}_0 | \Psi_m^{(0)} \rangle + \langle \Psi_m^{(0)} | \hat{v} | \Psi_m^{(0)} \rangle \\ &= \langle \Psi_m^{(0)} | \hat{H}_0 + \hat{v} | \Psi_m^{(0)} \rangle \\ &= \langle \Psi_m^{(0)} | \hat{H} | \Psi_m^{(0)} \rangle = E_0^{HF} \end{aligned} \quad (\text{Eq. II-67})$$

Second-order Møller–Plesset perturbation theory (MP2)^{216–218} is actually the one to provide the first meaningful correction to the HF energy:

$$E_m^{MP2} = E_m^{(0)} + E_m^{(1)} + E_m^{(2)} = E_0^{HF} + E_m^{(2)} \quad (\text{Eq. II-68})$$

The second-order correction to the system energy can be determined by:¹⁵⁷

$$E_m^{(2)} = \sum_{n>m} \frac{|\langle \Psi_m^{(0)} | \hat{v} | \Psi_n^{(0)} \rangle|^2}{E_m^{(0)} - E_n^{(0)}} \quad (\text{Eq. II-69})$$

in which $E_n^{(0)}$ is the eigenvalue corresponding to the eigenfunction $|\Psi_n^{(0)}\rangle$. The wave function $|\Psi_n^{(0)}\rangle$ represents the excited state with respect to the HF reference state. Due to the Brillouin theorem wherein the single excitation determinant, $|\Psi_i^a\rangle$, does not have a direct interaction with the HF ground-state electron configuration, we have:^{50,157,216}

$$\langle \Psi_0^{(0)} | \hat{v} | \Psi_i^a \rangle = 0 \quad (\text{Eq. II-70})$$

As a result, only double excitation determinants, $|\Psi_{ij}^{ab}\rangle$, contribute to the system energy via:¹⁵⁷

$$\langle \Psi_0^{(0)} | \sum_{i<j}^N \frac{1}{r_{ij}} |\Psi_{ij}^{ab}\rangle = \frac{1}{2} ([ia|jb] - [ib|ja]) \quad (\text{Eq. II-71})$$

and

$$\langle \Psi_0^{(0)} | \sum_{i=1}^N v^{HF}(i) |\Psi_{ij}^{ab}\rangle = [ia|jb] - [ib|ja] \quad (\text{Eq. II-72})$$

along with

$$\hat{H}_0 |\Psi_{ij}^{ab}\rangle = (E_0^{(0)} - (\varepsilon_i + \varepsilon_j - \varepsilon_a - \varepsilon_b)) |\Psi_{ij}^{ab}\rangle \quad (\text{Eq. II-73})$$

Hence, the second-order correction term, $E_0^{(2)}$, with respect to the HF ground-state wave function, $\Psi_0^{(0)}$, can be written as:^{157,216}

$$E_0^{(2)} = \frac{1}{4} \sum_{i<j} \sum_{a<b} \frac{|[ia|jb] - [ib|ja]|^2}{\varepsilon_i + \varepsilon_j - \varepsilon_a - \varepsilon_b} \quad (\text{Eq. II-74})$$

Similar to HF, MP2 has restricted and unrestricted versions. For the work described in this dissertation, we used restricted MP2 (RMP2) where the spin-up and spin-down electrons share the same spatial function. Although RMP2 does not characterize electron correlations well enough for our desired accuracy, especially static electron correlations, it was used to generate starting guesses of MOs, via diagonalizations of approximate one-particle density matrices,²¹⁹ for the next level of calculations utilizing the multiconfigurational self-consistent field (MCSCF) method which will be discussed in the next section.

Multiconfigurational Self-Consistent Field

In practice, chemical systems which have quasi-degenerate ground states with low-lying excited states are often of interest, e.g., in many molecules that contain one or more metal atoms. Besides that, many research studies are centered around the formation and dissociation pathways of these types of systems. Due to the inability to describe correlation effects accurately, RHF and RMP2 are not sufficient for such investigations. As discussed earlier, DFT is also not a good fit for studying excited states and multiconfigurational systems in general. Parenthetically, we note that although time-dependent DFT is often useful for describing excited states that are related to nondegenerate ground states by one-electron excitations, it is not useful for general excited states or for multiconfigurational ground states. Thus, we need a method that can describe electronic states that even qualitatively have multiple electron configurations. Multiconfigurational self-consistent field (MCSCF)^{31,37,38} is one of those methods where multiconfigurational characters are

captured in the form of multiple Slater determinants (in practice, spin-adapted linear combinations of Slater determinants (called configuration state functions (CSFs)) are used.

The MCSCF wave function, $|\Psi_{MCSCF}\rangle$, can be written as a linear combination of CSFs:^{37,157}

$$|\Psi_{MCSCF}\rangle = \sum_I c_I |\Psi_I\rangle \quad (\text{Eq. II-75})$$

in which c_I represents the configuration mixing coefficient corresponding to the I th CSF, $|\Psi_I\rangle$. The CSFs are defined in terms of fixed linear combinations of Slater determinants which are themselves anti-symmetrized linear combinations of MOs, ψ_i :³⁷

$$\Psi_I = A \left\{ \prod_{i \in I} \psi_i \right\} \quad (\text{Eq. II-76})$$

where ψ_i can be written as a linear combination of AOs as shown in Eq. II-13. The MCSCF energy is obtained by employing the variational principle in which $\langle \Psi_{MCSCF} | \hat{H} | \Psi_{MCSCF} \rangle$ is minimized.¹⁵⁷ Given a set of robust computational routines or programs, the most challenging task when applying the MCSCF method lies in the selection of active spaces (or model spaces).¹⁵⁰ An active space is often spanned by multiple electron configurations which allow excitations from specific high-occupancy orbitals to certain low-occupancy orbitals.⁵⁰ The selection of an active space has to be carried out manually by deciding how many active electrons and active orbitals are needed to make up a meaningful active space.¹⁵⁰

The most two popular variants of the MCSCF methods are the complete active space self-consistent field (CASSCF)²²⁰ and the restricted active space self-consistent field (RASSCF).²²¹ In CASSCF, all possible excited CSFs generated from the valence electrons of the target system are included in the complete active space (CAS).⁵⁰ Within this

approach, the orbitals are divided into three subspaces as shown in Figure II-4: (a) inactive space, where all the orbitals are doubly occupied, (b) active space, where a full configuration interaction (CI),²⁴⁻²⁷ with all possible CSFs being considered (the occupancy is between 0 and 2), and (c) virtual space, where the orbitals are unoccupied.²²² The CASSCF method brings two major advantages to the field of computational electronic structure theory. The first one resides in its ability to capture the multireference and multiconfigurational natures of many chemical systems within its complete active space.^{50,150} The second advantage exists in its decent descriptions of static electron correlations which are missing in the RHF and RMP2 methods.^{50,150} These two advantages have made the CASSCF method an excellent starting point when studying complex systems such as transition metals²²³⁻²²⁵ and biomolecules.^{226,227}

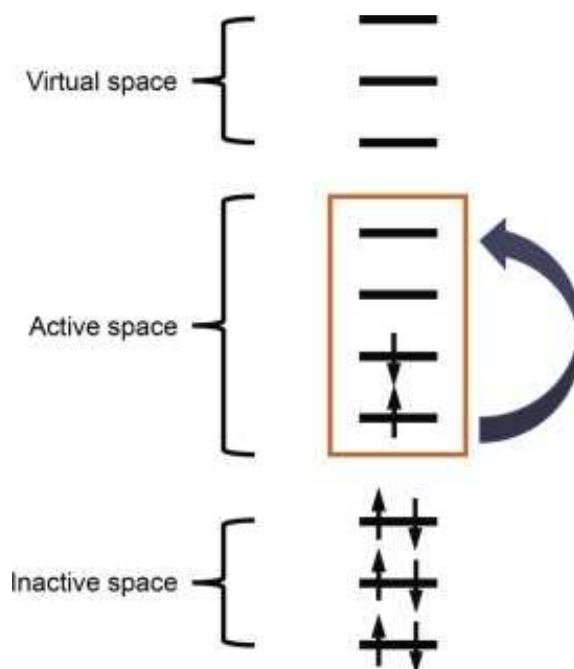


Figure II-4. Three subspaces of a CASSCF ansatz (the arrow represents electron excitations for generating a full CI within the active space). (Image taken from Ref.²²²)

With that being said, the CASSCF approach cannot be applied to many chemical systems because the more complex the target system becomes, the higher the number of MOs needed in the active space, resulting in the exponential scaling of the required number of CSFs within the CASSCF ansatz.^{50,228} In order to reduce the number of CSFs, a RASSCF is often used. Similar to CASSCF, a RASSCF ansatz has three subspaces: inactive, active, and virtual space. However, the active space in the RASSCF approach is divided further into three restricted active space (RAS) parts as shown in Figure II-5: (i) RAS1, where only a limited number of holes is allowed, (ii) RAS2, just like the active space in the CASSCF ansatz, and (iii) RAS3, where only a limited number of electrons is allowed.²²¹

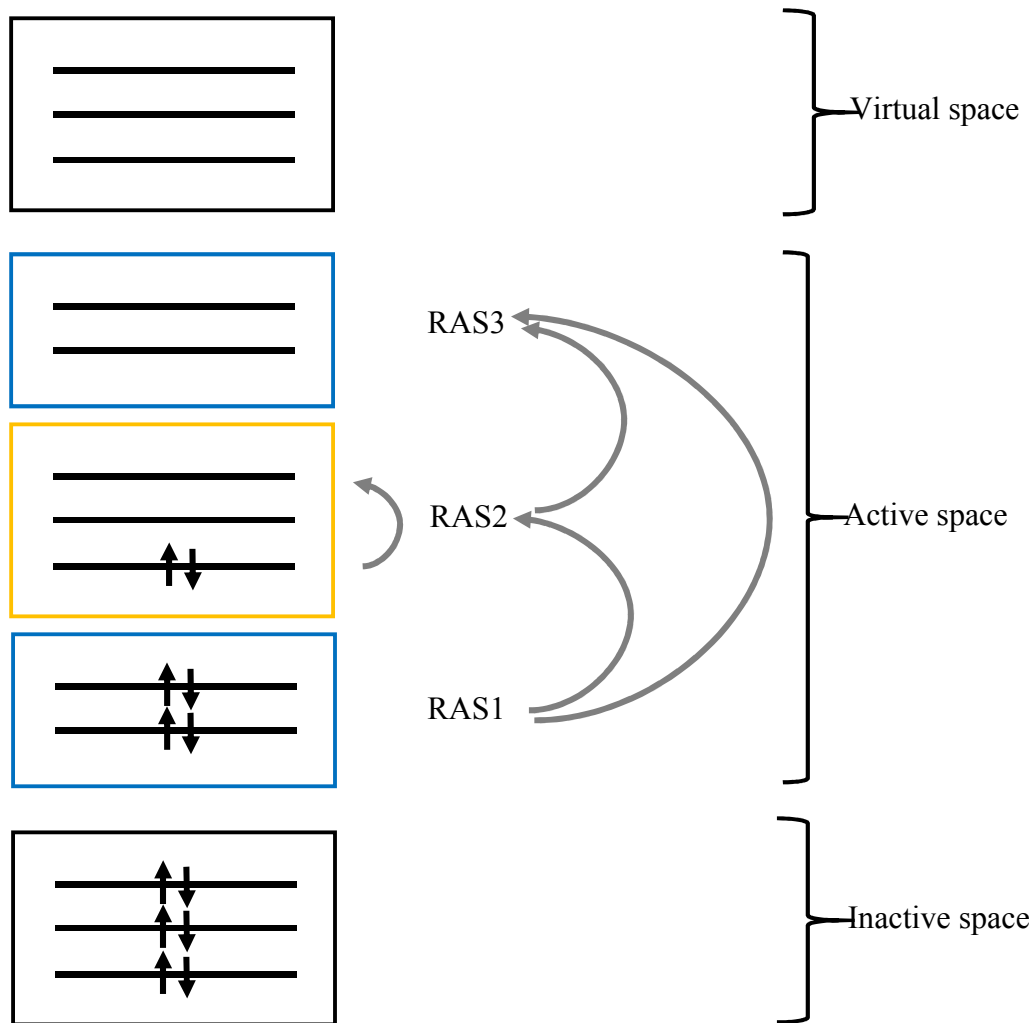


Figure II-5. Schematic representation of a RASSCF ansatz (the arrows represent electron excitations within the active space).

For our studies described in this dissertation, we used either CAS or the macroconfiguration approach.¹³⁴ The macroconfiguration approach, which was developed in our group, is a systematic way of generating incomplete model spaces that retain certain permutational symmetries. A RASSCF can be viewed as a special case of the macroconfiguration approach. In this approach, active orbitals are partitioned into subsets

(called groups for historical reasons) and active electrons are distributed among these groups:¹³⁴

$$\kappa(\mathbf{n}): \{G_1^{n_1} G_2^{n_2} \dots G_g^{n_g}\} \quad (\text{Eq. II-77})$$

where $\kappa(\mathbf{n})$ symbolizes a macroconfiguration with \mathbf{n} being a vector that specifies the distribution of active electrons over subsets of orbitals, G_1, G_2, \dots, G_g representing the active orbital groups, and n_1, n_2, \dots, n_g denoting the active electrons assigned to each group. The numbers of active electrons in the orbital groups must obey two conditions:¹³⁴

$$(i) \quad 0 \leq n_i \leq 2m_i \quad (i \in [1, g]) \quad (\text{Eq. II-78})$$

$$(ii) \quad n_1 + n_2 + \dots + n_g = \mathbf{n} \quad (\text{Eq. II-79})$$

in which n_i represents the number of active electrons in the active orbital group, G_i , and m_i denotes the number of active orbitals in G_i . So, unlike RASSCF, the macroconfiguration approach does not constrain the number of active electrons in any groups of active orbitals or the number of active orbitals in each group which gives the user more flexibility in choosing the active space of the system of interest. However, the use of macroconfigurations does not eliminate the limitations of the MCSCF method. The biggest problem still lies in the procedure of choosing a proper active space for the target system. Too small of an active space can lead to inaccurate results because the chemical properties of the system may not be described appropriately. Too big of an active space can result in prohibitively high computational cost. Therefore, the selection of a proper active space is not an easy task. It requires expert knowledge and years of experience. Another limitation within the MCSCF method is that it only accounts for static electron correlations but still misses most dynamic correlation effects. In fact, one of the subtler difficulties of using MCSCF is that the amount of dynamic correlation (i.e., relative to RHF) that is included

can be a function of nuclear geometry. That is the reason why we applied the GVVPT2 method to add in the dynamic electron correlations, to a consistent and high level, which will be discussed more in the next section. Nonetheless, the MCSCF method with the macroconfigurations gave us improved MOs compared to the ones obtained from our RMP2 calculations. These improved MOs significantly improve the accuracy of the GVVPT2 calculations.

Second-Order Generalized van Vleck Perturbation Theory

Second-order generalized van Vleck perturbation theory (GVVPT2)^{36,130–134} is a subspace-specific approach of the multireference perturbation theory (MRPT) method.²²⁹ By adding dynamical correlation effects into a starting MCSCF system, GVVPT2 provides a balanced description of dynamical and non-dynamical (or static) electron correlations.¹³³ GVVPT2 follows the “perturb-then-diagonalize” scheme, in which perturbative corrections are added to the active space term of the unperturbed Hamiltonian to construct an effective Hamiltonian matrix, which is then diagonalized to obtain the energies of electrons.^{132,133}

In the GVVPT2 method, a configuration space, L , is spanned by a set of target wave functions, $|\Psi_p\rangle$:

$$|\Psi_p\rangle = |\Psi_1, \Psi_2, \dots, \Psi_{N_p}\rangle \quad (\text{Eq. II-80})$$

where $\Psi_1, \Psi_2, \dots, \Psi_{N_p}$ are the target wave functions, and N_p represents the number of low-lying electronic states of the system of interest.¹³³ There are two subspaces within L : (i) model space, L_M (dimension of L_M is greater than N_p), and (ii) external space, L_Q , being connected with L_M through electron excitations.¹³³ An MCSCF space can also be used as

a spanning basis for the model space, L_M , of which a subset of reference functions, $\{\Phi_P\}_{P=1}^{N_P}$, are of interest.^{132,133} Consequently, the model space, L_M , can be further divided into two subspaces: (i) primary subspace, L_P , and (ii) secondary subspace, L_S , being the orthogonal complement to L_P , so we have:¹³³

$$L_M = L_P \oplus L_S \quad (\text{Eq. II-81})$$

The set of reference functions, $|\Phi_P\rangle$, can be mapped onto the set of target wave functions, $|\Psi_P\rangle$, by using the unitary wavelike operator, Ω :^{133,230}

$$|\Psi_P\rangle = e^X |\Phi_P\rangle \quad (\text{Eq. II-82})$$

where:

$$\Omega = e^X \quad (X^\dagger = -X) \quad (\text{Eq. II-83})$$

and X represents an anti-Hermitian operator and describes the primary-external (P - Q) rotations. By using the projection operators:

$$P = |\Phi_P\rangle\langle\Phi_P| \quad (\text{Eq. II-84})$$

$$S = |\Phi_S\rangle\langle\Phi_S| \quad (\text{Eq. II-85})$$

$$Q = |\Phi_Q\rangle\langle\Phi_Q| \quad (\text{Eq. II-86})$$

on L_P , L_S , and L_Q , respectively, and considering the $P - Q$ interactions to first-order in the target system's wave function, the block structure of the Hamiltonian matrix in the $L_P \oplus L_Q$ space can be used to express the unperturbed Hamiltonian, H_0 , as:²³¹

$$H_0 = PHP + QHQ \quad (\text{Eq. II-87})$$

and the off-diagonal block, \mathcal{V} , to be a perturbation, determined by:

$$\mathcal{V} = PHQ + QHP \quad (\text{Eq. II-88})$$

we arrive at the expressions for the second-order perturbatively corrected Hamiltonian matrices:¹³³

$$\mathbf{H}_{PP}^{eff} = \mathbf{H}_{PP} + \frac{1}{2}(\mathbf{H}_{PQ}\mathbf{X}_{QP} + \mathbf{X}_{QP}^\dagger\mathbf{H}_{QP}) \quad (\text{Eq. II-89})$$

$$\mathbf{H}_{SP}^{eff} = \mathbf{H}_{PS}^{eff} = \mathbf{H}_{SQ}\mathbf{X}_{QP} \quad (\text{Eq. II-90})$$

$$\mathbf{H}_{SS}^{eff} = \mathbf{H}_{SS} \quad (\text{Eq. II-91})$$

The P - Q rotation parameters included in the anti-Hermitian matrix, \mathbf{X}_{QP} , satisfy the system of linear equations:¹³³

$$(\mathbf{H}_{QQ} - E_0^P)\mathbf{X}_{QP} = -\mathbf{H}_{QP} \quad (\text{Eq. II-92})$$

with $P \in [1, N_p]$ and $\{E_0^P = \langle \Phi_P | H | \Phi_P \rangle\}_{P=1}^{N_p}$ being the energies of the reference states (i.e., MCSCF energies within L_M). The diagonalization scheme of the GVVPT2 method is demonstrated in Figure II-6.

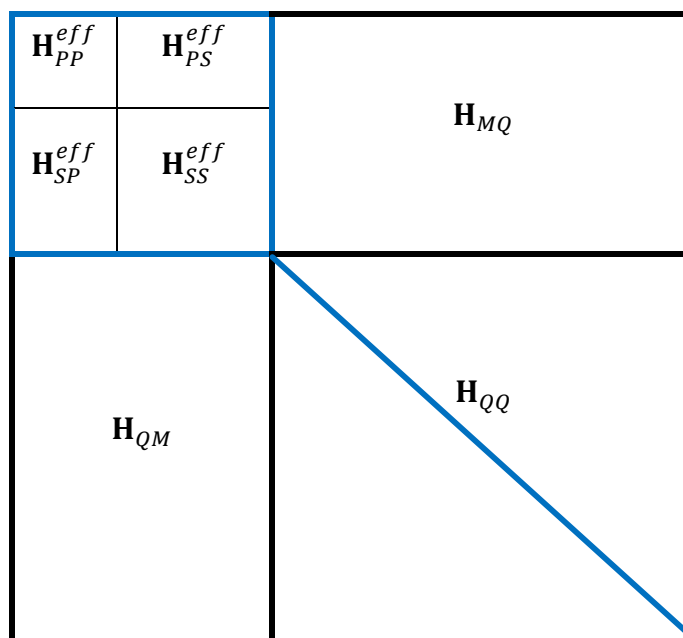


Figure II-6. Schematic representation of the subspaces labelled with their corresponding Hamiltonian matrices within a GVVPT2 ansatz.

(The \mathbf{H}_{PP}^{eff} , \mathbf{H}_{SP}^{eff} , \mathbf{H}_{PS}^{eff} , and \mathbf{H}_{SS}^{eff} make up the effective Hamiltonian matrix, \mathbf{H}_{MM}^{eff} , in the model space, and the blue diagonal line signifies that only the diagonal elements of the Hamiltonian matrix, \mathbf{H}_{QQ} , in the external space are kept (P : primary subspace, S : secondary subspace, M : model space, Q : external space)).

Since the subspaces can act as a buffer (in the energy spectrum) between the unperturbed MCSCF states and the external CSFs, the existence of intruder states is greatly diminished and can be eliminated entirely by judicious choice of nonlinear responses (see original articles for further detail).^{36,132,133} Other advantages of GVVPT2 include continuous, differentiable ground and excited potential energy surfaces, ability to adapt spins, and no restrictions on the active space structure.^{36,133} Above these, the most important advantage of GVVPT2 is the implementation of macroconfigurations.¹³⁴ This allows the use of incomplete active spaces, resulting in higher computational efficiency, especially for the evaluation of dynamic electron correlations.¹³³ GVVPT2 can be applied

for large systems which have up to 20 active orbitals and 1000 external orbitals.³⁶ In this dissertation, we used the GVVPT2 method which was implemented in our in-house software package named UNDMOL³⁶ to carry out the calculations on CaOH and SrOH monomers along with CaOH dimers. Details about these computational studies will be provided in chapter IV and V. Even though GVVPT2 has many great advantages mentioned above, it still suffers from the tedious and error-prone protocol of active space selection, just like in the case of the MCSCF method. Without in-depth knowledge, the user could arrive at many improper choices for the active space, resulting in inaccurate results or extremely high computational cost. This problem can be overcome with machine learning which will be described in the last section of this chapter.

The Spin-Free Exact Two-Component Method

Up till now, we have discussed only the nonrelativistic side of the Born-Oppenheimer approximation to the time-independent Schrödinger equation because relativistic effects are normally not dominant in the usual observables, such as positions, momenta, energies, and so on of molecules comprised entirely of lighter elements.²³² However, in the case of heavier elements (e.g., transition metals), relativistic effects could play an important role in the manifestations of certain observables such as spectroscopic and magnetic properties.²³² For our theoretical studies of SrOH described in this dissertation, the relativistic effects of strontium were considered. We used the spin-free exact two-component (sf-X2C) approach^{233–242} within the GVVPT2 method to include scalar relativistic effects.

The sf-X2C Hamiltonian can be written in second quantization as follows:

$$H = \sum_{pq} [\mathbf{h}_{+,sf}^{X2C}]_{pq} a_p^\dagger a_q + \frac{1}{2} \sum_{pqrs} (pr|qs) a_p^\dagger a_q^\dagger a_s a_r \quad (\text{Eq. II-93})$$

in which the first term denotes the one-electron spin-free (sf) part of the exact two-component (X2C) Hamiltonian with $\mathbf{h}_{+,sf}^{X2C}$ being the sf-X2C Hamiltonian for positive energy states, and the second term is responsible for the two-electron Coulomb interactions.²³⁴ In order to define $\mathbf{h}_{+,sf}^{X2C}$, we must first define the modified Dirac Hamiltonian, \mathbf{h}^D , which is the sum of the sf part, \mathbf{h}_{sf}^D , and spin-dependent (sd) part, \mathbf{h}_{sd}^D , as shown below:²³⁹

$$\mathbf{h}^D = \mathbf{h}_{sf}^D + \mathbf{h}_{sd}^D = \begin{pmatrix} \mathbf{V} & \mathbf{T} \\ \mathbf{T} & \frac{\alpha^2}{4} \mathbf{W}_{sf} - \mathbf{T} \end{pmatrix} + \begin{pmatrix} 0 & 0 \\ 0 & \frac{\alpha^2}{4} \mathbf{W}_{sd} \end{pmatrix} \quad (\text{Eq. II-94})$$

where \mathbf{V} is the matrix of the external nuclear attraction potential operator, $\hat{V} = -\frac{Z}{\vec{r}}$ (Z : charge of nucleus, \vec{r} : distance between electron and nucleus), \mathbf{T} is the matrix of the kinetic energy operator, $\hat{T} = \frac{\vec{p}^2}{2}$ (\vec{p} : momentum), α is the fine-structure constant, and \mathbf{W} is the matrix of the \hat{W} operator coupling momenta and the Pauli spinors,

$$\hat{W} = (\vec{\sigma} \cdot \vec{p}) \hat{V} (\vec{\sigma} \cdot \vec{p}) = \vec{p} \cdot \hat{V} \vec{p} + i \vec{\sigma} \cdot (\vec{p} \hat{V} \times \vec{p}) = \hat{W}_{sf} + \hat{W}_{sd} \quad (\text{Eq. II-95})$$

(with Dirac identity being applied). The sf part, \hat{W}_{sf} , of \hat{W} describes the scalar relativistic effects, and the sd part, \hat{W}_{sd} , represents the spin-orbit coupling effects.²³⁹ The modified Dirac Hamiltonian, \mathbf{h}^D , satisfies the one-electron Dirac equation:²³⁹

$$\mathbf{h}^D \mathbf{C} = \mathbf{MCE} \quad (\text{Eq. II-96})$$

where \mathbf{C} is the matrix of the Dirac bispinor, spanned by the large (**A**) and small (**B**) component coefficient matrices:

$$\mathbf{C} = \begin{pmatrix} \mathbf{A} \\ \mathbf{B} \end{pmatrix} \quad (\text{Eq. II-97})$$

and \mathbf{M} is the nonrelativistic metric:

$$\mathbf{M} = \begin{pmatrix} \mathbf{S} & 0 \\ 0 & \frac{\alpha^2}{2} \mathbf{T} \end{pmatrix} \quad (\text{Eq. II-98})$$

in which \mathbf{S} represents the overlap matrix in the kinetically balanced basis, $\{g_\mu\}$:

$$\mathbf{S}_{\mu\nu} = \langle g_\mu | g_\nu \rangle \quad (\text{Eq. II-99})$$

If the spin-orbit coupling effects are neglected, \mathbf{h}^D will only contain \mathbf{h}_{sf}^D , so Eq. II-96 will simply become:²³⁹

$$\mathbf{h}_{sf}^D \mathbf{C} = \mathbf{MCE} \quad (\text{Eq. II-100})$$

In the Schrödinger picture, the sf-X2C Hamiltonian for positive energy states, $\mathbf{h}_{+,sf}^{X2C}$, can now be expressed as:²³⁴

$$\mathbf{h}_{+,sf}^{X2C} \mathbf{C}_+ = \mathbf{S} \mathbf{C}_+ \mathbf{E} \quad (\text{Eq. II-101})$$

where \mathbf{S} represents the nonrelativistic metric. To incorporate the relativistic terms into the nonrelativistic Schrödinger equation, the relativistic metric, $\tilde{\mathbf{S}}_+$, in the Dirac picture needs to be utilized:²³⁴

$$\tilde{\mathbf{S}}_+ = \mathbf{S} + \left(\frac{\alpha^2}{4} \right) \mathbf{X}^\dagger \mathbf{T} \mathbf{X} \quad (\text{Eq. II-102})$$

The sf normalized elimination of small component (NESC) Hamiltonian, $\mathbf{L}_{+,sf}^{NESC}$, given by:²³³

$$\mathbf{L}_{+,sf}^{NESC} = \mathbf{V} + \mathbf{T} \mathbf{X} + \mathbf{X}^\dagger \mathbf{T} + \mathbf{X}^\dagger \left[\frac{\alpha^2}{4} \mathbf{W}_{sf} - \mathbf{T} \right] \mathbf{X} \quad (\text{Eq. II-103})$$

is then introduced, where \mathbf{X} describes the relation between the small and large component coefficient matrices as follows:

$$\mathbf{X} = \mathbf{B}_+ \mathbf{A}_+^{-1} \quad (\text{Eq. II-104})$$

Thus, the expression for the sf NESC Hamiltonian, $\mathbf{L}_{+,sf}^{NESC}$, in the Dirac picture turns out to be.²³⁴

$$\mathbf{L}_{+,sf}^{NESC} \mathbf{A}_+ = \tilde{\mathbf{S}}_+ \mathbf{A}_+ \mathbf{E} \quad (\text{Eq. II-105})$$

With the picture-change transformation, \mathbf{R} , given by:

$$\mathbf{R} = (\mathbf{S}^{-1} \tilde{\mathbf{S}}_+)^{-\frac{1}{2}} = \mathbf{S}^{-\frac{1}{2}} \left(\mathbf{S}^{-\frac{1}{2}} \tilde{\mathbf{S}}_+ \mathbf{S}^{-\frac{1}{2}} \right)^{-\frac{1}{2}} \mathbf{S}^{\frac{1}{2}} \quad (\text{Eq. II-106})$$

the sf NESC Hamiltonian, $\mathbf{L}_{+,sf}^{NESC}$, in the Dirac picture can be transformed into the sf-X2C Hamiltonian for positive energy states, $\mathbf{h}_{+,sf}^{X2C}$, in the Schrödinger picture, by using the relation.²³⁴

$$\mathbf{h}_{+,sf}^{X2C} = \mathbf{R}_+^\dagger \mathbf{L}_{+,sf}^{NESC} \mathbf{R}_+ \quad (\text{Eq. II-107})$$

By implementing NESC within the modified Dirac equation, a single matrix relating the small and large component coefficient matrices can be constructed for the whole set of positive energy states which is then obtained with just a single diagonalization.²³³ The method has shown to be successful in incorporating the relativistic terms into the nonrelativistic Schrödinger equation.^{233,235,236,240–246}

Advances in Active Space Selection using Machine Learning

As mentioned in the previous sections, the biggest drawback in which MCSCF, GVVPT2, along with other multireference methods all suffer from is the tricky protocol of active space selection. The procedure of choosing a proper active space requires professional expertise in order to acquire high level of accuracy while retaining computational efficiency. As the complexity of the chemical systems of interest increases,

the more electrons the systems contain, leading to more possible pathways the user could take to arrive at an appropriate active space for each of these systems. Thus, even with expert knowledge, it is still time-consuming to go through trials and errors to experiment with different active spaces and determine which one is the ideal one. As a result, this has hindered the studies of many complex chemical systems.

To achieve the ultimate goal of creating a black-box method in the field of active space selection for all chemical systems, an automatic process with data-driven technique is needed. Machine learning (ML) turns out to be a good fit for this job because ML algorithms are data-driven and can possibly operate without human intervention if being provided with sufficient training data.^{150,154} However, the incorporation of ML into multireference methods is very new and there is still a lot of work needed to be done to reach the ultimate goal. So far, the supervised ML model has been used to predict if an active space chosen for a system of interest is good or bad, a routine for which was developed by Jeong et al.¹⁵⁴ In this routine, data points at specific internuclear distances were first extracted from CASSCF/complete active space second-order perturbation theory (CASPT2)^{33,34} calculations conducted on a training set of diatomic molecules; and then the corresponding active spaces to these data points were labelled as either good or bad based on the comparison of bond dissociation energies, equilibrium bond lengths, and vibrational constants to experimental data.¹⁵⁴ By applying the scalable gradient-boosting system called XGBoost,²⁴⁷ which is an algorithm used to make a final prediction by combining the predictions from previous trees in the decision-tree system, a classification ML model was built and trained for active space screening.¹⁵⁴

Golub et al.,²⁴⁸ on the other hand, used the neural network (NN) approach within ML to predict the importance of orbitals. They employed density matrix renormalization group (DMRG)^{249–251} (a variation of the multireference methods) to generate the training data for chemical systems of transition metal complexes.²⁴⁸ After training, their NN models were able to predict which strongly correlated orbitals were important and needed to be included in the active spaces of other systems, which were not parts of the training sets.²⁴⁸ Although the work of Jeong et al.¹⁵⁴ and Golub et al.²⁴⁸ described above have helped reduce the number of trials involved in the active space selection procedure for investigating certain systems, their protocols have not yet reached the goal of being universal for all chemical systems because there are still problems in the transferability between the training sets and the systems of interest. This has inspired us to develop a ML routine using macroconfigurations within the GVVPT2 method. Since macroconfigurations enable the use of incomplete active spaces and have no restrictions on the number of active electrons in each active orbital group,^{133,134} many more complicated systems could be used without trading off essential accuracy for low computational cost. A training set with a wider variety of size and composition would ensure better transferability from the training data to the target systems. For our ML models described in this dissertation, we used reinforcement learning approach to solve the user-specified active space problem within GVVPT2. The calculations of ground state water, stretched water (i.e., ground state water in which the bonds were symmetrically elongated), and triplet ground state methylene have validated the active space selection ability of our ML model as well as the high degree of transferability that the model offers. Further discussions are provided in chapter VI.

III. THEORETICAL STUDIES OF IRIIDIUM SILICIDE MONOLAYERS USING DENSITY FUNCTIONAL THEORY

Introduction

Ever increasing markets for smaller, faster, and cheaper electronics have created and are expected to continue to foster a constant demand for new materials. The latest excitement in the field is over two-dimensional (2D) materials with novel electronic structures such as graphene,^{69,70,73,74} silicene,⁷⁷⁻⁷⁹ and germanene,²⁰⁹⁻²¹¹ which exhibit extremely high charge carrier mobility,^{71,72,82,83} topological Dirac insulator characteristics,⁸⁴⁻⁸⁷ and quantum spin and anomalous Hall effects.⁸⁸⁻⁹² Among these 2D materials, silicene, a monolayer of silicon atoms arranging in a honeycomb lattice, has a special place due to relative ease of incorporating it into existing Si-based technologies.^{75,80,81} Experimentally, silicene has been reported to grow epitaxially on various substrates such as Ag(111),^{79,93-97} Ir(111),⁹⁸ ZrB₂(0001),⁹⁹ MoS₂,¹⁰⁰ ZrC(111),¹⁰¹ and Au(111) surfaces.¹⁰² Theoretical calculations on free-standing silicene suggest that this 2D system is stable with properties similar to graphene. However, in contrast to graphene, the interaction between metal atoms and the silicene is quite strong due to highly reactive buckled hexagonal structures which drastically modify the electronic properties of silicene.^{103,104} One possible way to preserve novel properties of silicene is to intercalate alkali metals between the silicene and the metal surface, which makes it possible to weaken the interaction between silicene and the metal surface.¹⁰³

A possible method to enrich properties of silicene is to integrate metals, especially transition metals, into the silicene network. Binary monolayers of silicon with different transition metals have given rise to a new family of 2D nanomaterials that is known as transition metal (TM) silicides. Twenty *3d* and *4d* TM silicides with a chemical formula of $TMSi_2$ (TM = Sc, Ti, V, Cr, Mn, Fe, Co, Ni, Cu, Zn, Y, Zr, Nb, Mo, Tc, Ru, Rh, Pd, Ag, and Cd) have been investigated by applying first-principles calculations.¹⁰⁵ The TM silicides have exhibited a variety of magnetic properties, with $TiSi_2$, VSi_2 , $CrSi_2$, $NbSi_2$, and $MoSi_2$ being ferromagnetic, $MnSi_2$ and $FeSi_2$ antiferromagnetic, and the rest possessing nonmagnetic properties.¹⁰⁵ Other theoretical studies have also showed diverse magnetic properties of different TM silicides, indicating promising applications in spintronic and magnetic electronic devices.^{106–113}

This chapter of the dissertation describes our published work in studying iridium silicide (Ir-Si) monolayers.¹¹⁴ By using density functional theory (DFT)^{43,47} calculations, we investigated structural, electronic, and mechanical properties of iridium (Ir) silicide monolayers. In bulk form, the Ir-silicide/Si interface has the lowest (highest) Schottky barrier for holes (electrons), which indicates that the 2D form of the material might be expected to exhibit novel properties, including in-plane anisotropy,^{255,256} ultra-high carrier mobility,⁷³ strong-light matter interaction,²⁵⁷ extreme mechanical stability,²⁵⁸ high flexibility,²⁵⁹ and so on. Different plausible structures of Ir-Si monolayers with various atomic ratios were first modelled, with their lattice constants varied to explore structure relaxations. The cohesive energies were then calculated on the geometry optimized structures with the lowest energy equilibrium lattice constant to determine their relative stabilities. Subsequently, the computation of phonon dispersions, band structures, density

of states, and mechanical analyses were conducted on the stable structures to explore their physical and chemical properties.

Computational Methods

The projector augmented wave (PAW) method^{189,202–205} was used to simulate interactions between ion cores and valence electrons. The exchange-correlation (XC) potential was treated using Perdew-Burke-Ernzerhof (PBE) formalism within generalized gradient approximation (GGA).¹⁸⁰ Because periodic boundary conditions¹⁸⁵ were applied, a vacuum region of 15 Å was placed along the z -direction to avoid spurious interactions between periodic images. Structure relaxation was performed until a force of less than 0.01 eV/Å on each atom was obtained. The kinetic energy cutoff for plane waves and the total energy convergence criteria were set to 500 eV and 10^{-6} eV, respectively. The spacing of \mathbf{k} -points in Monkhorst-Pack grids was 0.01 \AA^{-1} . To confirm the energetic stability of the Ir-Si monolayers, we calculated the cohesive energies using the following equation;

$$E_{coh} = E_{total}(Ir_xSi_y) - xE_{total}^{bulk}(Ir) - yE_{total}^{bulk}(Si) \quad (\text{Eq. III-1})$$

where $E_{total}(Ir_xSi_y)$, $E_{total}^{bulk}(Ir)$, and $E_{total}^{bulk}(Si)$ are the total energies of the Ir_xSi_y monolayer, of the bulk Ir (per atom), and of the bulk Si (per atom), respectively. The interatomic force constants and elastic moduli were obtained using density functional perturbation theory (DFPT) as implemented in the VASP code.²⁶⁰ Here, the convergence criterion of the self-consistent field calculations was set to 10^{-8} eV, atomic positions and lattice constants were optimized until the Hellmann-Feynman forces were less than 0.00001 eV/Å and the pressure on the supercell was decreased to values less than 1 kbar.

Finally, the vibrational frequencies were obtained by using the phonopy code,²⁶¹ which can directly use the force constants obtained by either DFPT or the force constant method.

Results and Discussion

Different plausible structures of Ir-silicide monolayers with various Ir:Si ratios and lattice types (rectangular, square, and hexagonal) were modeled, including relaxation of the structures, to find their optimal values with the lowest equilibrium lattice constants. The cohesive energies of these optimized structures were then calculated using Eq. III-1. We found that the ground state of all considered structures is spin-unpolarized. Among these structures, the Ir₂Si₄ monolayer (r-IrSi₂) with Pmmn space group was identified as the lowest energy structure, with a cohesive energy of -0.495 eV (or -0.248 eV per formula unit (f.u.)) with respect to bulk Ir and bulk Si (Figure III-1). This can be attributed to the strong Si-Si bonding within this structure. A negative cohesive energy means that the chemical reaction of $2\text{Ir (bulk)} + 4\text{Si (bulk)} \rightarrow \text{Ir}_2\text{Si}_4 \text{ (monolayer)}$ is exothermic, i.e., such reaction is thermodynamically favorable in experiments. The structure also has a geometry that is slightly buckled. Therefore, we opine that it should be possible to experimentally synthesize the Ir₂Si₄ monolayer.

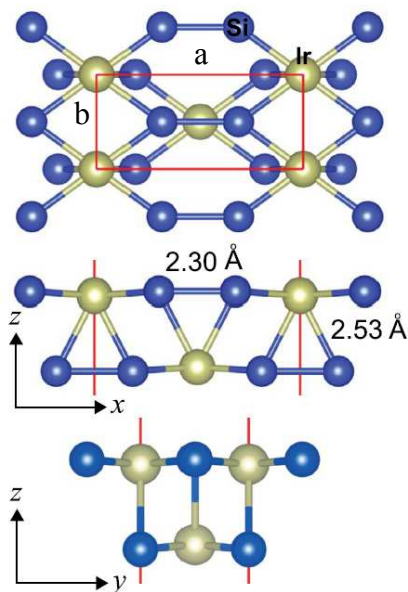


Figure III-1. The top and side views of rectangular r-IrSi₂ monolayer. The optimized lattice constants are $a = 6.18 \text{ \AA}$ and $b = 2.84 \text{ \AA}$. (Image taken from Ref.¹¹⁴)

The optimized lattice constants of the r-IrSi₂ monolayer are $a = 6.18 \text{ \AA}$ and $b = 2.84 \text{ \AA}$. The thickness of this monolayer (t), calculated using the distance between the topmost Si surface atoms, is 2.38 \AA . In addition, the calculated Si-Si distance within the dimer and the inter-plane (in-plane) Ir-Si bond lengths are 2.30 and 2.53 (2.41) \AA , respectively. Such a bond length between silicon atoms indicates that there is a single bond between Si atoms so that one can qualitatively describe the bonding in terms of Si₂ dimers. Since semi-local functionals can be expected to overestimate the lattice parameters, we performed test calculations to check the effect of varying XC functionals on the structural parameters of r-IrSi₂. The lattice constants became $a = 6.12 \text{ \AA}$ and $b = 2.81 \text{ \AA}$ when we used the screened Heyd–Scuseria–Ernzerhof (HSE06) hybrid functional.²⁶² In addition, the interatomic lengths within the Si-Si dimer and in-plane Ir-Si bond length are 2.28 and 2.38 \AA , respectively, which can be seen to be very close to PBE values. Additionally, we repeated

the band structure calculation using the HSE06 hybrid functional, which is expected to be more accurate in describing the XC energy of electrons. We found that both the GGA and HSE06 functionals lead to similar dispersion curves of bands. Of special note, the metallic property is preserved. Thus, we believe that PBE is sufficient to capture the properties of Ir-Si monolayers.

Figure III-2 shows the electron localization function (ELF), which takes values between 0.00 and 1.00. Generally, values of 1.00 and 0.50 denote the fully localized and fully delocalized electrons, respectively. The values near 0.00 correspond to very low charge densities. Here, the ELF isovalue is set to 0.7. Localization of a charge density between Si atoms corroborates the geometrical evidence of strong covalent bonding within Si dimers. Note that Si dimers on the same plane also interact with each other.

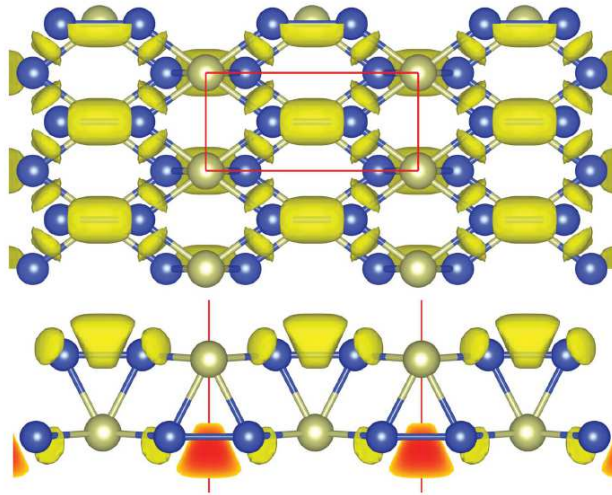


Figure III-2. The top and side views of the ELF for the r-IrSi₂ monolayer. The ELF isovalue is set to 0.7. (Image taken from Ref.¹¹⁴)

To further investigate the mechanical stability of the r-IrSi₂ monolayer, we calculated its elastic constants as well as the direction-dependent Young's modulus, $Y(\theta)$, and Poisson's ratio, $\nu(\theta)$, based on the elastic constants using Eq. III-2 and Eq. III-3:

$$Y(\theta) = \frac{C_{11}C_{22} - C_{12}^2}{C_{11}s^4 + C_{22}c^4 + \left(\frac{C_{11}C_{22} - C_{12}^2}{C_{44}} - 2C_{12}\right)c^2s^2} \quad (\text{Eq. III-2})$$

$$\nu(\theta) = -\frac{\left(C_{11} + C_{22} - \frac{C_{11}C_{22} - C_{12}^2}{C_{44}}\right)c^2s^2 - C_{12}(s^4 + c^4)}{C_{11}s^4 + C_{22}c^4 + \left(\frac{C_{11}C_{22} - C_{12}^2}{C_{44}} - 2C_{12}\right)c^2s^2} \quad (\text{Eq. III-3})$$

where $c = \cos\theta$ and $s = \sin\theta$. We first calculated the elastic constants and found them to be $C_{11} = 246.8$ N/m, $C_{22} = 148.5$ N/m, $C_{12} = 68.9$ N/m, and $C_{44} = 53.7$ N/m. They satisfy the Born criteria: namely $C_{11}, C_{22}, C_{44} > 0$, and $C_{11}C_{22} - C_{12}^2 > 0$, which implies that r-IrSi₂ is mechanically stable. In Figure III-3, we show the direction-dependent $Y(\theta)$ and $\nu(\theta)$. The Young's modulus for the r-IrSi₂ monolayer in the x ($\theta = 0^\circ$) and y ($\theta = 90^\circ$) directions are calculated to be $Y_x(\theta = 0^\circ) = 214.8$ N/m and $Y_y(\theta = 90^\circ) = 129.3$ N/m, respectively. Since all the Si-Si dimers are aligned parallel in the x direction, $Y(\theta)$ and $\nu(\theta)$ deviate from perfect circles and display a mechanical anisotropy of the r-IrSi₂ sheet. Along the x -direction, Ir atoms bind to Si-Si dimers, leading to much stronger interaction as compared to the y -direction, thereby giving rise to a large value of Y along the x -direction. Comparing these results to those of MoS₂ (with $C_{11} = 132.7$ N/m, $C_{12} = 33$ N/m, $Y = 124.5$ N/m, and $\nu = 0.25$),²⁶³ the r-IrSi₂ monolayer is stiffer. The corresponding Poisson's ratios (the ratio between the lateral contraction and the longitudinal extension) in the x ($\theta = 0^\circ$) and y ($\theta = 90^\circ$) directions are $\nu_x(\theta = 0^\circ) = 0.46$ and $\nu_y(\theta = 90^\circ) = 0.28$, respectively.

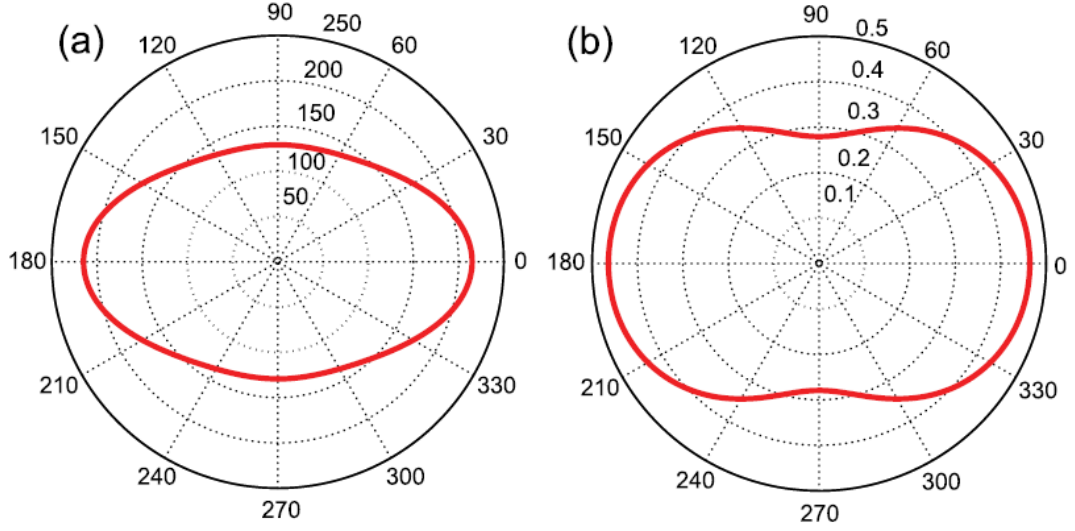


Figure III-3. Direction-dependent (a) Young's modulus (N/m) and (b) Poisson's ratio for the r-IrSi₂ monolayer. (Image taken from Ref.¹¹⁴)

To make a reliable comparison with experimentally measured Young's modulus values of other 2D materials, we recalculated Young's modulus of r-IrSi₂ using $Y_{3D}=Y/t$. With this definition, we are able to compare the stiffness against uniaxial stress of various 2D and three-dimensional (3D) materials. By using this definition, Young's modulus becomes 902.5 GPa along the x -direction and 543.3 GPa along the y -direction. The effective thickness of Ir₂Si₄ monolayer is likely be larger than 2.38 Å due to the effective decay of electron density into vacuum.²⁶⁴ Therefore, we can suggest that our calculated values are the upper limits for Young's modulus.

With the help of elastic theory, the gravity induced out-of-plane deformation (h) can be estimated by using Eq. III-4:

$$\frac{h}{L} \approx \left(\frac{\rho g L}{Y} \right)^{1/3} \quad (\text{Eq. III-4})$$

where g is the gravitational acceleration, $\rho = 4.7 \times 10^{-6} \text{ kg/m}^2$ is the density of the 2D r-IrSi₂ crystal, and L is the size of the nanosheet. When taking $L \approx 100 \text{ }\mu\text{m}$ and $Y = 129.3$

N/m (which is the smallest value of Young's modulus), we obtain $h/L \approx 3.29 \times 10^{-4}$, comparable to that of graphene.²⁶⁵ Therefore, it should be expected that the Ir₂Si₄ nanosheet can withstand its own weight and retain a freestanding planar structure.

Phonon dispersion spectra and phonon density of states (PDOS) were computed for the r-IrSi₂ monolayer to investigate its dynamical stability. As shown in Figure III-4, all vibrational modes are real in the whole Brillouin zone, which indicates dynamical stability of this structure. While longitudinal acoustic (LA) and transverse acoustic (TA) modes have a linear dispersion for small \mathbf{q} values (i.e., in the long wavelength limit), which represent in-plane vibrations, the flexural acoustic (ZA) mode shows a quadratic relationship, which demonstrates out-of-plane vibrations. The highest frequency optical mode approaches 16 THz and corresponds to the Si-Si vibration within Si₂ dimers. Due to its greater atomic weight, the Ir atom mainly contributes to the vibrational modes below 5 THz. The two highest optical modes are separated from other optical modes by a phonon gap of 5 THz.

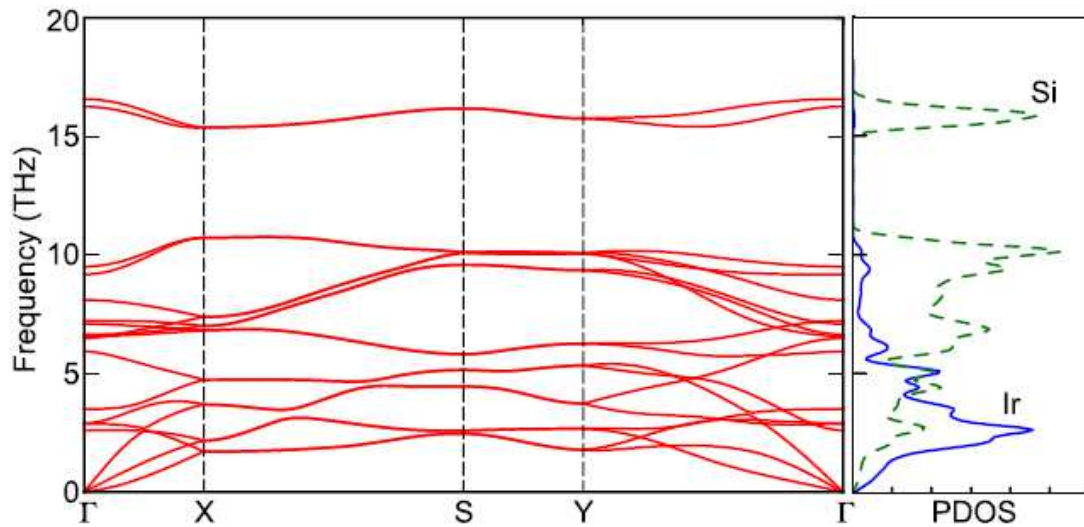


Figure III-4. Phonon spectra and PDOS of the rectangular r-IrSi₂ monolayer. (Image taken from Ref.¹¹⁴)

Band structure and density of states (DOS) were also calculated for the r-IrSi₂ monolayer. As can be seen in Figure III-5, there is no band gap in its band structure, indicating that the rectangular Ir₂Si₄ monolayer displays metallic properties. Orbital decomposed DOS shows that the bands near the Fermi level are dominated by Ir 5*d* (red) and Si 3*p* (blue) orbitals. It can also be seen that the majority of the Ir 5*d*-orbitals contributions lie about 1 eV below the Fermi level and are localized within a range of 4 eV, which indicates a charge transfer from the less electronegative Si atom to more electronegative Ir atom. Bader charge analysis^{266–269} confirmed that Si atoms (Ir) lose (gain) electrons. The DOS also indicates apparent hybridization between Ir 5*d*-orbitals and Si-3*p* orbitals. In addition, we calculated the work function as 4.69 eV, meaning that r-IrSi₂ is a high work-function material.

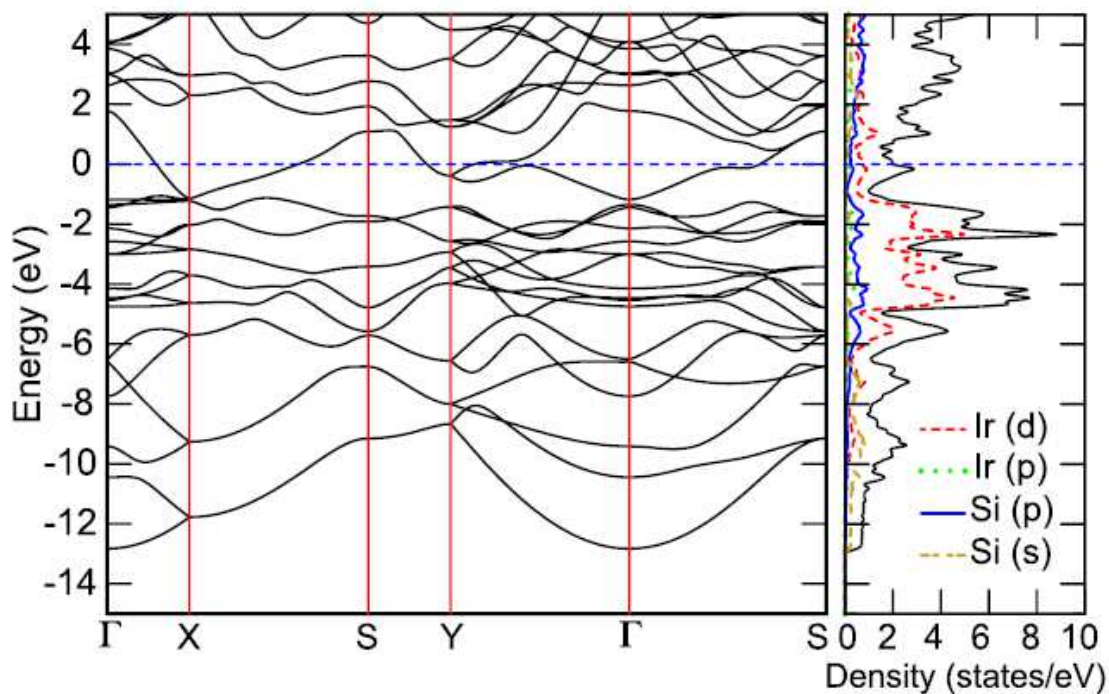


Figure III-5. Band structure and orbital decomposed DOS of the r-IrSi₂ monolayer. The Fermi level marks the zero energy. (Image taken from Ref.¹¹⁴)

In addition to the lowest energy r-Ir₂Si₄ structure, numerous other higher energy monolayer structures with different unit-cell symmetries were investigated; see Figure III-6 for the fully optimized structures. Some of candidate structures were based on bulk IrSi₂, such as structures shown in Figure III-6(b) and 6(e).²⁷⁰ Other silicide monolayer structures were based on the most stable structures for Fe-Si (Figure III-6(c) and 6(h)),²⁷¹ Ti-Si (Figure III-6(d) and 6(f)),¹¹³ Cu-Si,²⁷² and Ni-Si.²⁷³ But, these are energetically less stable for Ir-Si than r-Ir₂Si₄.

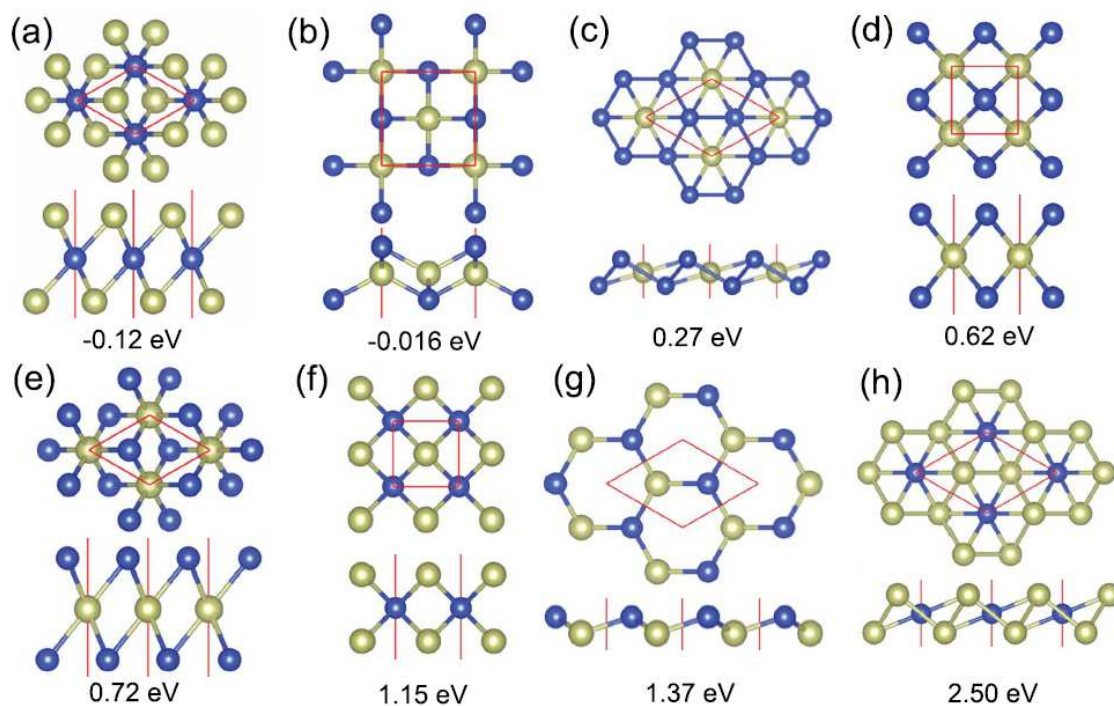


Figure III-6. The top and side views of several optimized Ir-Si monolayers. Cohesive energies (eV) per formula unit are given for each structure. (Image taken from Ref.¹¹⁴)

Akin to our predicted ground-state structure, all other candidate structures exhibit metallic behavior. In contrast to the planar Cu_2Si monolayer, one atom thick planar structures are highly unstable.²⁷² If one compares the structures shown in Figure III-6(a) with 6(h) and Figure III-6(c) with 6(e), the formation of Si-Si bonds apparently enhances the stability of the monolayer structures. Although the Si-Si distances are 2.79 and 4.35 Å in Figure III-6(e), they become 3.99 and 2.67 Å in Figure III-6(c). Our ground-state structure ($r\text{-IrSi}_2$) can be qualitatively described as a combination of two nearly planar structures on top of each other that maximize the coordination number of Ir and Si atoms. In addition to this structure, we also checked dynamical and mechanical stabilities of the structures shown in Figure III-6(a) ($h\text{-Ir}_2\text{Si}$) and Figure III-6(b) ($t\text{-IrSi}$). The former is

energetically more stable than the latter. Calculated lattice constants are 2.81 Å for h-Ir₂Si and 4.10 Å for t-IrSi; h-Ir₂Si consists of trilayer sheets with a hexagonal-like unit cell, where the “Si” layer is sandwiched by two “Ir” metal layers with a D_{3d} point group symmetry. The Si-Ir-Si bond angle and Ir-Si bond length are 71° and 2.40 Å, respectively. The structure in Figure III-6(h) can be described as a low buckled version of h-Ir₂Si, in which the bond angle becomes 107°. Due to the hexagonal symmetry of h-Ir₂Si, there are only two independent elastic constants, namely $C_{11} = 253.0$ N/m and $C_{12} = 55.5$ N/m. The stability of the h-Ir₂Si monolayer is also confirmed by the phonon dispersion curves shown in Figure III-7(a), where there is no appreciable imaginary phonon mode. The ZA mode is slightly negative for small wave numbers (or in long wavelength limit). The extent of the region of imaginary frequencies around the Γ -point depends, to some extent, on computational parameters, such as \mathbf{k} -mesh, the size of the vacuum region, the energy cut-off, the size of simulation cell, and so on. Therefore, a categorical analysis of computational parameters should be done to be sure that the calculated imaginary frequencies are not artifacts of the calculation. If this is not due to computational accuracy limitations, then this situation may be interpreted as the instability against long-wavelength transversal waves. This instability can be removed in experimental realizations by the formation of the defects, including ripples. In addition, by reducing the flake size under which long-wavelength transversal waves do not occur, it is possible to stabilize the h-Ir₂Si monolayer. The highest frequency of the h-Ir₂Si sheet approached 15.1 THz. Similarly, the mechanical and dynamical stabilities of the t-IrSi monolayer, with an isotropic zigzag-shaped buckled structure, were confirmed via elastic constants and phonon calculations, see Figure III-7(b). This structure has a square unit cell where each Ir atom is four-coordinated. The

buckling parameter, distance between the topmost Si atoms, is 2.24 Å. The calculated elastic constants are $C_{11} = 94.8$ N/m, $C_{22} = 69.1$ N/m, and $C_{12} = 55.3$ N/m. These elastic constants are substantially smaller than those of graphene ($C_{11} = 341$ N/m) but comparable to silicene ($C_{11} = 62$ N/m).

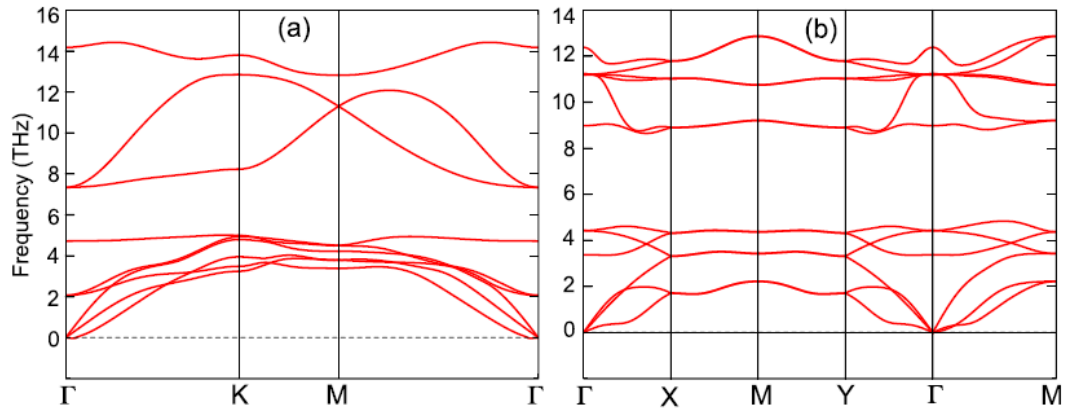


Figure III-7. Phonon spectra of (a) h-Ir₂Si and (b) t-IrSi monolayers. (Image taken from Ref.¹¹⁴)

To check the temperature-dependent stability of dynamically stable Ir-Si monolayers, we computed thermodynamic properties. The calculated Debye temperatures ($\Theta_D = \frac{h\omega_D}{k_B}$, where ω_D is the Debye frequency) are 269, 245, and 297 K for r-IrSi₂, t-IrSi, and h-Ir₂Si, respectively. Here, the Debye temperature is a temperature above which all vibrational modes begin to be excited. In addition, using phonon frequencies in the whole Brillouin zone, we calculated thermodynamic properties, namely, Helmholtz free energy F and entropy S using following formulas:²⁶³

$$F = -k_B T \ln Z = \frac{1}{2} \sum_{\mathbf{q}\nu} \hbar\omega(\mathbf{q}\nu) + k_B T \sum_{\mathbf{q}\nu} \ln \left[1 - \exp\left(-\frac{\hbar\omega(\mathbf{q}\nu)}{k_B T}\right) \right] \quad (\text{Eq. III-5})$$

$$S = -\frac{\partial F}{\partial T} = \frac{1}{2T} \sum_{\mathbf{q}\nu} \hbar\omega(\mathbf{q}\nu) \coth\left(\frac{\hbar\omega(\mathbf{q}\nu)}{2k_B T}\right) - k_B \sum_{\mathbf{q}\nu} \ln \left[2 \sinh\left(\frac{\hbar\omega(\mathbf{q}\nu)}{2k_B T}\right) \right] \quad (\text{Eq. III-6})$$

where T , k_B , \mathbf{q} , and ν are the temperature, the Boltzmann constant, the wave vector, and the band index, respectively. Figure III-8 shows the calculated Helmholtz free energy and entropy as functions of temperature. Consistent with the third law of thermodynamics, the Helmholtz free energy increases with increasing temperature. F is positive around 0 K. However, when we add the calculated cohesive energy, which is negative, F becomes negative for r-IrSi₂ and t-IrSi, which indicates the stability of these monolayers over the considered temperature range. F is still slightly positive for h-Ir₂Si, which indicates that stability of this monolayer depends on temperature and it can be stabilized above 200 K, see Figure III-8(c). Consistent with the calculated E_{coh} values, F is the lowest for the r-IrSi₂ monolayer. At $T = 0$ K, F only includes the contribution of the zero-point energy (the first term in Eq. III-5). Due to the presence of Si-Si dimers, r-IrSi₂ has the highest zero-point energy.

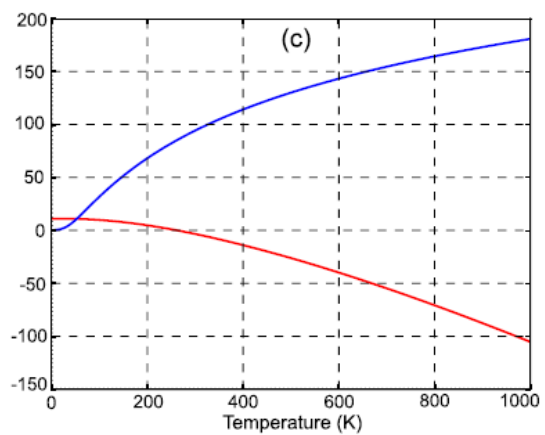
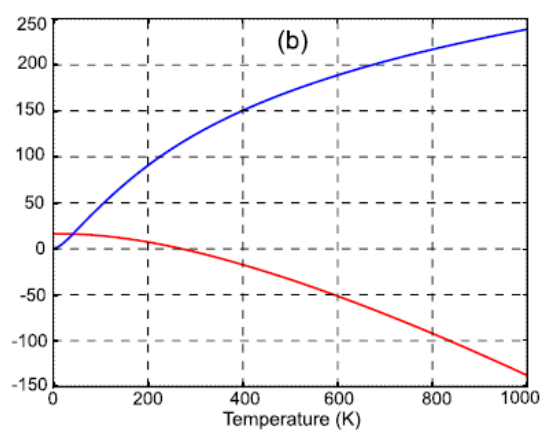
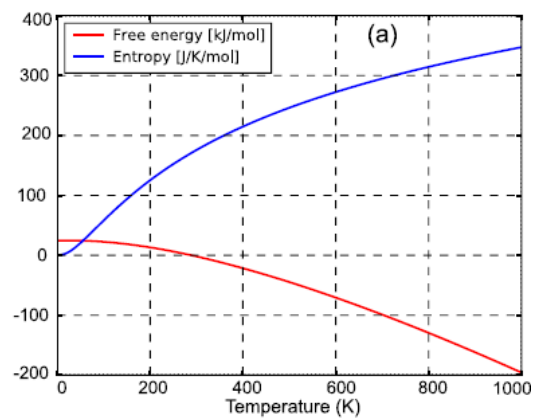


Figure III-8. Calculated Helmholtz free energies and entropies for (a) r-IrSi₂, (b) t-IrSi, and (c) h-Ir₂Si monolayers. (Image taken from Ref.¹¹⁴)

It is known that Si-based surfaces can be very reactive to O₂ and H₂O molecules. We investigated the interaction of O₂ and H₂O with the stable Ir-Si monolayers. Since the O₂ molecule has a triplet ground state, we considered spin-polarization for O₂ adsorption. In addition, the van der Waals interactions were included using the DFT-D3 method (DFT with dispersion corrections),⁶¹ including Becke-Johnson damping.⁶⁸ For the sake of brevity, we only discussed the r-IrSi₂ case. Figure III-9 displays the ground-state adsorption structures for both the H₂O and O₂ molecules. To minimize coupling between molecules in the periodic images, the interaction of these molecules with Ir-Si monolayers were considered using large supercells. Thus, our results can be interpreted to mimic the effects of an isolated molecule. The binding energy, E_b , of molecules were calculated using Eq. III-7:

$$E_b = E_T[\text{monolayer} + \text{molecule}] - E_T[\text{monolayer}] - E_T[\text{molecule}] \quad (\text{Eq. III-7})$$

Here, the first term is the calculated total energy of the monolayer with an adsorbed molecule. The second and third terms are the total energies of the bare monolayer and isolated molecule, respectively. A negative value of E_b indicates binding of a molecule to the Ir-Si monolayer. We found that O₂ exothermically dissociates on the free-standing r-IrSi₂. The dissociated O atoms form strong bonds with Si atoms, which substantially lowers the energy of the system; E_b is -3.71 eV/oxygen. However, the interaction of H₂O molecule with the r-IrSi₂ monolayer is mainly van der Waals type, with a binding energy of -0.42 eV/molecule. In the case of O₂ molecule, the dissociated O atoms reside at a position above the midpoint of Si-Si dimer bond (i.e., bridge site) with a Si-O bond length of 1.68 Å, which is slightly longer than the Si-O bond length in crystalline SiO₂ (ranging from 1.55 to 1.61 Å). The Si-Si bond length in the dimer enlarges from 2.30 to 2.53 Å. H₂O

molecularly binds to the monolayer via an O-Si bond with a bond length of 2.07 Å. Kinetically, the dissociation of O₂ molecule occurs without the need to overcome any energy barrier, which means that freestanding Ir-Si monolayers are unstable in the presence of O₂, which is similar to silicene.²⁷⁴ We have similar absorption behavior for O₂ and H₂O molecules on the t-IrSi and h-Ir₂Si monolayers. For instance, the dissociated O atoms sit at the hollow sites on the h-Ir₂Si monolayer. H₂O molecule always binds to a surface via the O atom of the molecule.

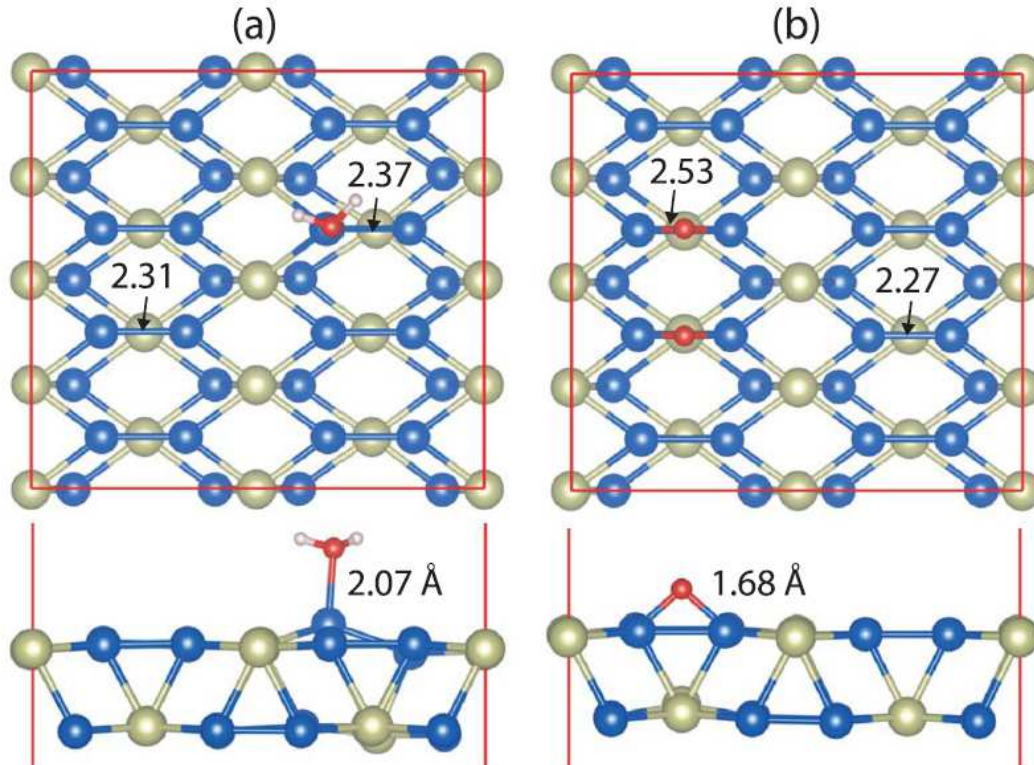


Figure III-9. The lowest energy adsorption structure of (a) H₂O and (b) O₂ on the freestanding r-IrSi₂ monolayer. (Image taken from Ref.¹¹⁴)

We identified three different mechanically and dynamically stable Ir-Si monolayers. Unlike transition metal dichalcogenides (for example, the 1H and 1T phases of MoS₂), we do not expect a spontaneous structural transformation from t-IrSi/h-Ir₂Si to r-IrSi₂. This is because all three structures have significantly different crystal structures (i.e., different coordination numbers for atoms and different symmetries) and they are well separated in configuration space. Therefore, for each stable monolayer, it may be possible to find suitable substrates on which to grow them. For instance, the substrate with a tetragonal surface symmetry can be used to grow t-IrSi. Similarly, h-Ir₂Si can be synthesized on the (111) surface of substrates that have an FCC crystal structure. Importantly, the cohesive energies of these monolayer structures are approximately 1.3–1.4 eV/f.u. higher than that of bulk IrSi₂. The difference of 1.27 eV/f.u. for silicene shows its viability to be synthesized on Ag (111) surfaces,^{79,93–97} which indicates the fabrication of Ir-Si monolayers should be experimentally feasible on suitable substrates.

Conclusions

In this work, we explored stable Ir-Si monolayers using state-of-the-art first principles' calculations. Among the large number of candidate materials, a new type of 2D Ir silicide, namely, r-IrSi₂, was identified as the lowest energy structure. It contains Si₂ dimers in which Si atoms have single bonds. We demonstrated that this sheet is not only dynamically and mechanically stable, but also exhibits a metallic band structure and has anisotropic elasticity. The r-IrSi₂ sheet is stiffer along the direction in which the Si₂ dimers are aligned. In addition to this ground-state structure, we also predicted higher energy dynamically stable structures that have hexagonal and square unit cell structures. Due to

their quite different structures, once they are synthesized, it may be expected that these structures will not transform to each other. We found that Ir-Si monolayers are unstable in an oxygen environment, with the barrierless dissociation of the O₂ molecule into two O atoms. However, we found that the H₂O molecule interacts only weakly with Ir-Si monolayers. Its binding energy are rather small and have predominantly van der Waals character.

IV. THEORETICAL STUDIES OF CALCIUM MONOHYDROXIDE AND STRONTIUM MONOHYDROXIDE MONOMERS USING GVVPT2

Introduction

Astrophysical environments, such as planetary atmospheres on other planets, circumstellar envelopes, protoplanetary disks, and interstellar medium, have gained increasing interest in recent years due to the growing number of new molecules being discovered in these regions.^{115,116} So far, more than 200 astrophysical molecules, containing different elements with various sizes and charges, have been detected.¹¹⁶ However, that number is still insignificant compared to the amount of unidentified spectral features in spectroscopic data.¹¹⁶ To interpret these spectra lines, a large amount of laboratory work should be done, which is not always feasible due to the difficulty in collecting and preserving samples of astrophysical molecules. Even for planets and regions that are relatively close to Earth, launching a space probe to collect samples is extremely expensive and time-consuming. Many NASA missions have costs in the range of hundreds of millions to billions of dollars and often takes years to complete.²⁷⁵ Thus, theoretical methods have risen as alternatives for completing molecular line lists, especially for complex polyatomic molecules.²⁷⁶ Theoretical studies have continued to play a major role in aiding the detection of new astrophysical molecules. And, even in the area of so-called laboratory astrophysics, in which terrestrially unstable molecules are synthesized in

ultrahigh vacuum and generally very cold environments, theoretical studies often play essential roles.

The case of calcium monohydroxide (CaOH) radical has called for theoretical work. Its presence is expected on hot rocky super-Earth exoplanets, but its detection was hindered due to a lack of spectral data in the molecular line lists.^{277,278} CaOH is also the suspected source of missing opacity around $18,000\text{ cm}^{-1}$ from the benchmark BT-Settl model, which is used to simulate stellar atmospheres of stars, brown dwarfs, and planets.^{129,279–281} The missing opacity was found in a 2013 M-dwarf study.²⁸⁰ There have been theoretical studies devoted to completing the spectroscopic data for CaOH to assist with future detection of this astrophysical radical.^{129,281–289}

The missing opacity is not the only motivation for theoretical investigations of CaOH. Its potential applications in laser cooling and trapping technologies have provided additional motivation why CaOH has been actively studied lately. The complicated rotation-vibration-electronic (rovibronic) energy level structure of CaOH fits well in systems of laser cooling and trapping.^{290–293} Not only CaOH, but other alkaline earth metal monohydroxides, especially strontium monohydroxide (SrOH), have also attracted much attention because of their high Franck-Condon factors and strong photon cycling, which are essential elements for designing laser cooling and trapping systems.^{294–298} SrOH was one of the first ultracold polyatomic molecules which were created under direct laser cooling.^{296,299} With laser cooling, full control of quantum states and longer experimental times are possible which help provide insights to chemical reactivities, dynamics, and reaction pathways of many molecular systems.^{296,297,300–302}

As a result, complete and accurate lists of electronic energies across various electronic states, especially excited states, for these alkaline earth metal monohydroxides could prove useful in aiding the designs of laser cooling and trapping schemes as well as astronomical detection of these radicals in the future.²⁸¹ To this end, we used the second-order generalized van Vleck perturbation theory (GVVPT2) method^{36,130–134} to investigate the ground state ($\tilde{X}^2\Sigma^+$) of CaOH and SrOH monomers along with the first low-lying excited state ($\tilde{A}^2\Pi$) of CaOH. In addition, we applied the scalar relativistic effects integrated in the spin-free exact two-component (sf-X2C) approach^{233–239} to study the impact of scalar relativity on SrOH. Although the ground state and many low-lying excited states of CaOH were previously studied using theoretical methods,^{129,281–289} our plan is to reinvestigate these two states to compare the accuracy level of the GVVPT2 method to the other *ab initio* methods used in those previous studies (i.e., multireference configuration interaction (MR-CI),¹²⁹ multireference double-excitation configuration interaction (MRD-CI),²⁸⁸ effective valence shell Hamiltonian (H^v),²⁸⁹ and spin-restricted coupled cluster with single, double, and perturbative triple excitations (RCCSD(T))²⁸⁷) with the intention of establishing the accuracy baseline for our studies of SrOH because to the best of our knowledge, SrOH have not been intensively studied using theoretical methods. Moreover, because of the lower computational scaling of GVVPT2 (i.e., $O(n^5)$ vs. e.g., $O(n^7)$ for RCCSD(T) for computational costs, where n is representative of system size), GVVPT2 offers advantages for larger studies, such as the CaOH dimerization described in the following chapter. The properties of the ground state ($\tilde{X}^2\Sigma^+$) of SrOH were compared to the results from RCCSD(T) method²⁹⁷ and experimental data.³⁰³

Computational Methods

We used the cc-pVTZ basis set^{287,304} for calcium (Ca), oxygen (O), and hydrogen (H) while the cc-pVTZ-X2C basis set^{305,306} was utilized for strontium (Sr). The restricted Hartree–Fock (RHF) approximation^{18–20,157} was used for an initial optimization of equilibrium geometries of CaOH and SrOH monomers as well as to generate their initial molecular orbitals (MOs). Then the restricted second-order Møller–Plesset perturbation theory (RMP2) method^{28,157,216–218} was employed to add some electron correlation and obtain approximate natural orbitals. The actual calculations involve geometry optimization at the GVVPT2 level, using our in-house program called UNDMOL.³⁶ At each nuclear geometry, multiconfigurational self-consistent field (MCSCF)^{31,37,38} calculations were conducted with these active space configurations to further refine the orbitals. When geometries were relatively close, the MOs of the previous geometry were used as initial guesses for the current geometry. Subsequently, to provide balanced descriptions of dynamic and static electron correlations, we applied the GVVPT2 method on the MCSCF optimized orbitals. The sf-X2C method was applied at the time of calculating integrals over atomic basis functions, and so was included in all calculations for SrOH. To assess the effect of relativistic corrections, a series of calculations was run in which the X2C corrections were deliberately turned off.

Results and Discussion

A. Calcium Monohydroxide (CaOH)

The geometry optimization of CaOH equilibrium structure was obtained using C_s point group symmetry in the GVVPT2 method and the cc-pVTZ basis set. A complete

active space (CAS) was used for both the ground state and the first excited state of CaOH. The CAS for the ground state ($\tilde{X}^2\Sigma^+$) included 8 orbitals (7–10a' and 4–7a'') with 11 electrons. The first excited state ($\tilde{A}^2\Pi$) using 10 orbitals in its CAS (7–12a' and 3–6a'') with 13 electrons.

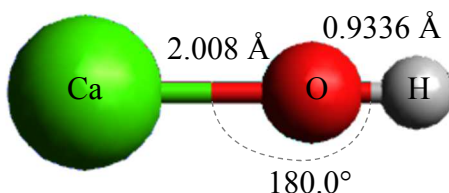


Figure IV-1. Equilibrium structure of CaOH optimized at the GVVPT2/cc-pVTZ level.

The ground state of CaOH was found to be linear (see Figure IV-1), which is consistent with the results from the other *ab initio* methods and experimental data shown in Table IV-1. The equilibrium Ca–O bond length ($R_{\text{Ca-O}}$) calculated at the GVVPT2 level is 2.008 Å, which is slightly longer than the experimental value by approximately 0.033 Å. The equilibrium O–H bond length ($R_{\text{O-H}}$) from our GVVPT2 calculations was computed to be 0.9336 Å, which is shorter than the experimental value by 0.0200 to 0.0226 Å. The results also agree well with the other theoretical studies, which used highly correlated methods, shown in Table IV-1. Our GVVPT2 $R_{\text{Ca-O}}$ is longer than the values from the MR-CI, H^v , and RCCSD(T) method, but shorter than the one from the MRD-CI calculations. On the other hand, the GVVPT2 $R_{\text{O-H}}$ is shorter than all the results from these theoretical studies.

Table IV-1. Comparison of geometry parameters (Å and degrees) of the ground state of CaOH optimized at the GVVPT2/cc-pVTZ level with other *ab initio* methods and with experimental data.

	R _{Ca-O}	R _{O-H}	∠(Ca-O-H)
GVVPT2/cc-pVTZ	2.008	0.9336	180.0
MR-CI/cc-pV5Z ¹²⁹	1.975	0.952	180.0
MRD-CI/AO basis set ²⁸⁸	2.03	0.953	180
<i>H^v</i> /3-21G augmented ²⁸⁹	1.938	0.9568	180
<i>H^v</i> /6-311G** ²⁸⁹	1.989	0.9528	180
RCCSD(T)/cc-pVQZ ²⁸⁷	1.9776	0.9519	180
RCCSD(T)/cc-pV5Z ²⁸⁷	1.9778	0.9520	180
Experiment ^{307,308}	1.9746 – 1.9751	0.9536 – 0.9562	180

The data from Table IV-2 shows that the vertical excitation energy (T_e) for the first low-lying excited state (the $2^2A'$ of $\tilde{A}^2\Pi$) of CaOH computed at the GVVPT2/cc-pVTZ level agrees very well with the value from the $H_{3\text{rd-order}}^v/6-311G^{**}$ calculations, only varying by 0.001 eV. However, the GVVPT2 T_e value is higher than the results from the $H_{3\text{rd-order}}^v/3-21G$ augmented method by 0.027 eV, and higher than the experimental value by 0.029 eV, which are still minor differences. The data from the MRD-CI method with custom AO basis set appears to be the lowest of all (1.94 eV), compared to the experimental value (1.984 eV) and the other *ab initio* methods (1.986 – 2.013 eV). In general, our GVVPT2 T_e data for the first CaOH excited state agrees with the results from published literature. We are also in the process of studying the second excited state ($\tilde{B}^2\Sigma^+$) of CaOH. Unfortunately, we have not been able to find an appropriate active space to describe the nature of this state. This illustrates the rationale for the motivation for us to build our machine learning (ML) algorithm to help us automate the active space selection process. Further discussions about our ML protocol are provided in chapter VI of this dissertation.

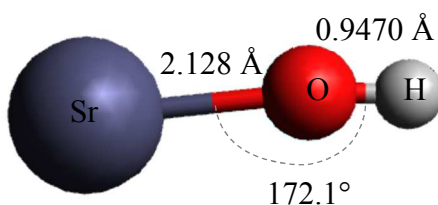
Table IV-2. Comparison of vertical excitation energies (T_e) for the first low-lying excited state of CaOH calculated at the GVVPT2/cc-pVTZ level with other *ab initio* methods and with experimental data. $T_e = 0$ eV for the ground state.

	T_e (eV)
GVVPT2/cc-pVTZ	2.013
MRD-CI/AO basis set ²⁸⁸	1.94
$H_{3\text{rd-order}}^v/3-21G$ augmented ²⁸⁹	1.986
$H_{3\text{rd-order}}^v/6-311G^{**}$ ²⁸⁹	2.012
Experiment ³⁰⁸	1.984

B. Strontium Monohydroxide (SrOH)

The geometry optimization of the SrOH ground state ($\tilde{X}^2\Sigma^+$) equilibrium structure was obtained with C_s point group symmetry using the GVVPT2 method. For the Sr atom, we utilized the cc-pVTZ-X2C basis set, while the cc-pVTZ basis set was applied to the O and H atoms. A complete active space (CAS) was configured in the MCSCF and GVVPT2 calculations. The CAS included 9 orbitals (15–21a' and 6–7a'') with 9 electrons, for both the cases of with and without relativistic corrections.

(a) With relativistic corrections



(b) Without relativistic corrections

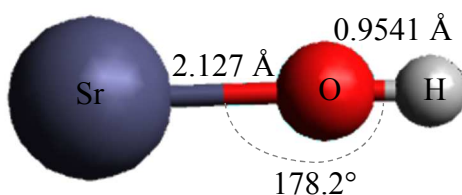


Figure IV-2. Equilibrium structure of SrOH optimized at the GVVPT2/cc-pVTZ level (a) with and (b) without relativistic corrections.

The ground state of SrOH without relativistic effects was found to be a slightly bent geometry with a bond angle of 178.2° (see Figure IV-2(b)), as opposed to the linear geometry found by the RCCSD(T) method and the experiment shown in Table IV-3. The

equilibrium Sr–O bond length ($R_{\text{Sr-O}}$) calculated at the GVVPT2 level without relativistic corrections is 2.127 Å, which is slightly longer than both the experimental value and the RCCSD(T) results by approximately 0.016 Å. The equilibrium O–H bond length ($R_{\text{O-H}}$) from our GVVPT2 calculations was computed to be 0.9541 Å, which is also longer than the experimental value (by 0.0321 Å) and the RCCSD(T) results (by 0.0316 Å).

Table IV-3. Comparison of geometry parameters (Å and degrees) of the ground state of SrOH optimized at the GVVPT2/cc-pVTZ level with other *ab initio* methods and with experimental data.

	$R_{\text{Sr-O}}$	$R_{\text{O-H}}$	$\angle(\text{Sr-O-H})$
GVVPT2 ^a	2.127	0.9541	178.2
GVVPT2/relativistic ^a	2.128	0.9470	172.1
RCCSD(T) ^{297,b}	2.1110	0.9225	180
Experiment ³⁰³	2.111	0.922	180

^aSr: cc-pVTZ-X2C, O and H: cc-pVTZ

^bSr: aug-cc-pV5Z-PP + ECP28MDF, O and H: aug-cc-pCVTZ

By including the relativistic adjustments, the change in the Sr–O bond length was negligible (0.001 Å) – the $R_{\text{Sr-O}}$ slightly increased to 2.128 Å. On the other hand, the change in the O–H bond length was more apparent (0.0071 Å) – the $R_{\text{O-H}}$ decreased to 0.9470 Å (see Figure IV-2(a) and Table IV-3). The bond angle also shifted under the relativistic effects, in which the geometry of SrOH became more bent with an angle of 172.1°. It could be because the relativistic corrections tend to contract the *s* and *p* atomic orbitals, which decreased the bond angle of Sr–O–H by 6.1°.

Conclusions

In this work, we used the GVVPT2 method to investigate the ground state ($\tilde{X}^2\Sigma^+$) of CaOH and SrOH monomers along with the first low-lying excited state ($\tilde{A}^2\Pi$) of CaOH. Our GVVPT2 results show that the optimized geometry parameters of CaOH as well as the vertical excitation energy of its first excited state are in good agreement with other *ab initio* methods and experimental data. However, the GVVPT2 calculations of the SrOH ground state indicate a quasilinear geometry as opposed to the linear characteristics described in the published literature. Since Sr is a heavy element, we suspected the scalar relativity could have a major impact on the equilibrium properties of SrOH. With that in mind, we used the scalar relativistic effects in the sf-X2C approach to study this impact. The optimized geometry of SrOH shifted more towards the bent geometry with a bond angle of 172.1° . For future work, experiments with different basis sets and active space configurations for SrOH could be investigated if this bent geometry is resistant to changes in these types of input parameters. In addition, more low-lying excited states of CaOH should be explored to have a better understanding of the characteristics of this radical.

V. THEORETICAL STUDIES OF CALCIUM MONOHYDROXIDE DIMERIZATION USING GVVPT2

Introduction

In recent years, calcium monohydroxide (CaOH) has been actively studied because of its potential applications in laser cooling and trapping systems. Laser cooling is a technology in which atomic and molecular samples are cooled down to sub-milliKelvin temperatures.^{291,296,297,309–311} Different trapping techniques, such as magnetic trapping,^{312,313} optical trapping,^{314,315} and magneto-optical trapping^{316–318} help confine these ultracold atoms and molecules at ultracold temperatures. These technologies enable full control over quantum states and help lengthen experimental times, resulting in better understanding of chemical reactivities, dynamics, and reaction pathways of many chemical systems.^{296,297,300–302} Alkaline earth metal monohydroxides are great candidates because they have dense rotation-vibration-electronic (rovibronic) energy level structures, high Franck-Condon factors, and strong photon cycling.^{290–298}

The ground state ($\tilde{X}^2\Sigma^+$) and several of the lowest-lying excited states of CaOH monomers have been studied using theoretical methods with the hope that more efficient laser cooling and trapping could be designed with CaOH.^{129,281–289} Besides obtaining accurate descriptions of multiple electronic states, investigating the collisions of CaOH at ultracold temperatures is essential because controlled collisions could lead to desirable elastic and inelastic scattering rates which are important factors in designing these cooling

systems as demonstrated in previous collision studies of different polyatomic molecules.^{291,294,297,319,320} High elastic scattering rates will help achieve thermal equilibrium and low inelastic scattering rates will prevent the molecules from two-body losses.²⁹¹ For the collisions between certain molecules, we also need to consider the possibility of undesirable chemical reactions occurring. For instance, in the case of CaOH monomers colliding with each other, the chemical equation of $\text{CaOH} + \text{CaOH} \rightarrow \text{Ca(OH)}_2 + \text{Ca}$ is considered to be unlikely because the repulsive components of the dipole–dipole interactions could be expected to prevent the reaction from happening; available information about the potential energy surface for the reaction does not support its occurrence.²⁹¹

The work of Augustovičová et al.,²⁹¹ in which they studied the elastic and inelastic scattering rates as functions of electric field, has become the inspiration for our theoretical studies of CaOH dimerization. To this end, we used second-order generalized van Vleck perturbation theory (GVVPT2) method^{36,130–134} to investigate the dimers of CaOH. The starting CaOH monomers were first investigated with the GVVPT2 level of theory and the results were then compared with other *ab initio* calculations to establish the accuracy baseline for our GVVPT2 calculations. This chapter of the dissertation will only focus on our theoretical work on the dimerization of CaOH. The details of our calculations on CaOH monomers were previously provided in chapter IV.

Computational Methods

We used the cc-pVTZ basis set^{287,304} for calcium (Ca), oxygen (O), and hydrogen (H). The restricted Hartree–Fock (RHF) approximation^{18–20,157} was used for an initial

optimization of equilibrium geometries of CaOH dimers as well as to generate their initial molecular orbitals (MOs). Then the restricted second-order Møller–Plesset perturbation theory (RMP2) method^{28,157,216–218} was employed to add some electron correlation and obtain approximate natural orbitals. Next, we used the macroconfiguration approach¹³⁴ which was developed in our group to configure the active space for the dimers of CaOH. The actual calculations involve geometry optimization at the GVVPT2 level, using our in-house UNDMOL program.³⁶ At each nuclear geometry, multiconfigurational self-consistent field (MCSCF)^{31,37,38} calculations were conducted with these active space configurations to further refine the orbitals. When geometries were relatively close, the MOs of the previous geometry were used as initial guesses for the current geometry. Subsequently, to provide balanced descriptions of dynamic and static electron correlations, we applied the GVVPT2 method on the MCSCF optimized orbitals for CaOH dimers. This helped provide insights to the dimerization pathways of CaOH as well as the transformation between various isomers of CaOH dimers.

Discussion and Future Directions

The study of CaOH dimerization started with optimizing CaOH monomers in their ground states. The geometry optimization of the CaOH monomers was obtained with C_s point group symmetry using the GVVPT2 method and the cc-pVTZ basis set. A complete active space (CAS) was used in these monomer calculations which included 8 orbitals (7–10a' and 4–7a'') with 11 electrons. As discussed in chapter IV, the ground state of the CaOH monomer was found to be linear with the equilibrium Ca–O and O–H bond lengths being 2.008 Å and 0.9336 Å, respectively (see Figure IV-1), which is in good agreement

with the results from the other *ab initio* methods and experimental data shown in Table IV-1. It indicates that the active space we used in the calculations of CaOH monomers could be a good starting point for each monomer in the computation of CaOH dimerization.

To begin the calculations of CaOH dimers, we placed two CaOH monomers approximately 6 bohr apart. We kept the Ca–O and O–H bond lengths to be the same as in the optimized ground state of CaOH monomers while decreasing the Ca–O–H bond angles to approximately 150° to account for the van der Waals interactions between two monomers. We partitioned the active space of the CaOH dimer into two groups: $G_1 = \{13-16a' \text{ and } 7-10a''\}$ with 11 electrons, and $G_2 = \{17-20a' \text{ and } 11-14a''\}$ with 11 electrons. Since the total number of configuration state functions (CSFs) are 636,608, which is much higher than the total number of CSFs in the calculations of CaOH monomers (504 CSFs) and of SrOH monomers (4508 CSFs), calculations with this active space are lengthy and there are no good estimates of how long these calculations will take to complete. In addition, for a large system like the CaOH dimer, there are many possible ways of configuring its active space which requires a large number of trials and errors to reach an appropriate configuration. It can be noted that the brute force complete active space of 22 electrons in 16 orbitals is beyond the capabilities any current supercomputer. This type of problem has motivated us to develop our machine learning model with the aim that we could automate the active space selection process. Further discussions are given in chapter VI.

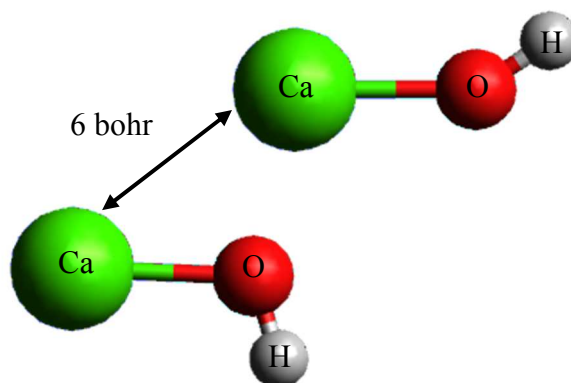


Figure V-1. The starting arrangement of two CaOH monomers in our study of CaOH dimerization.

Subsequent studies could explore more isomers of CaOH dimers and their transition states, in particular optimization of geometry parameters as well as electronic energies in order to determine which isomer is the most stable. Moreover, collisions of CaOH monomers to form $\text{Ca}(\text{OH})_2$ are of interest. Answers to these questions will further characterize systems of CaOH radicals, and especially its potential in applications of cooling and trapping systems.

VI. DEVELOPMENT OF MACHINE LEARNING IN ACTIVE SPACE SELECTION WITHIN GVVPT2

Introduction

Many multireference and multiconfigurational methods, such as multireference CI (MR-CI),^{24,25,30,31} multireference perturbation theory (MRPT),^{32–36} and multireference CC (MR-CC)^{39,40}, have been widely used in the field of computational electronic structure theory to study small- to medium-sized chemical systems because they can provide high levels of accuracy with decent computational cost, if the starting molecular orbitals (MOs) have already been optimized with lower levels of theory ahead of time, such as using Hartree–Fock (HF)^{18–20,157} or multiconfigurational self-consistent field (MCSCF)^{31,37,38} orbitals. Further approximations can also be applied for specific methods to help reduce the computational cost further. For example, incomplete active spaces can be employed (e.g., in the restricted active space self-consistent field (RASSCF) method²²¹) to reduce the exponential scaling of the required number of configuration state functions (CSFs) relative to the complete active space self-consistent field (CASSCF) ansatz.²²⁰ The macroconfiguration approach¹³⁴ has also been proven to be effective in exploring complex chemical systems because it allows the use of more specialized incomplete active spaces. Since macroconfigurations do not constraint the number of active electrons in any groups of active orbitals or the number of active orbitals in each orbital group,¹³⁴ the user has more flexibility in choosing an active space compared to even the restricted active space

approach (i.e., RASSCF). With macroconfigurations, calculations using high level methods like MR-CI with single and double excitations (MR-CISD), and especially $O(n^5)$ methods such as second-order generalized van Vleck perturbation theory (GVVPT2),^{36,130–134} can be carried out at reasonable computational cost, as demonstrated in published studies.^{321–324}

However, without expert knowledge and years of experience, the procedure of choosing a proper active space can be very tricky for these multireference-multiconfigurational methods. As the complexity of chemical systems of interest increases, the number of possible arrangements for the electrons in different orbital groups also increases, resulting in more trial and error cycles the user must go through to arrive at an ideal active space for the systems of interest. Unfortunately, a universal protocol for active space selection has not yet been established. Recently, the question of whether the process of active space selection can be automated has been put back on the table because there is a new rising technology that is data-driven and can help with the automatic process. It is called machine learning (ML).¹³⁹ ML algorithms are data-driven and can possibly operate without human intervention if being provided sufficient training data.^{150,154} Since ML has already revolutionized many aspects of our daily life, including the use of voice assistants,¹³⁵ image recognition,¹³⁶ intelligent gaming,¹³⁷ autonomous driving,¹³⁸ and so on, why not quantum chemistry?

Evidently, ML has opened the gate to new ways of solving electronic structure problems.^{148–155} Yet there is a long way to go to achieve a black-box method which can be used on any chemical system. Although the incorporation of ML into multireference methods is still new, the works of Jeong et al.¹⁵⁴ and Golub et al.²⁴⁸ have proven that ML

could help automate the process of active space selection. The routine developed by Jeong et al.¹⁵⁴ used a supervised ML model to predict if an active space chosen for a system of interest is good or bad. Golub et al.,²⁴⁸ on the other hand, used the neural network (NN) approach within ML to predict the importance of orbitals, and hence, which orbitals should be included in the active space. Unfortunately, their protocols have not yet reached the goal of being universal for all chemical systems because there are still problems in the transferability between the training sets and the systems of interest.

This has inspired us to develop our own ML routine to solve the user-specified active space problem within the GVVPT2 method. Since macroconfigurations allow the use of incomplete active spaces and have no restrictions on the number of electrons in each orbital group, a wider variety of challenging and complicated systems could be used in the set of training data while maintaining the balance between accuracy and computational cost. A training set with a broader variation of size and composition would ensure better transferability from the training data to the systems of interest. To this end, we intend to use macroconfigurations within GVVPT2 for the machine to configure different active spaces. However, to simplify our problem at this early state of designing our ML model, we used complete active space (CAS) approach instead. The reinforcement learning approach with convolutional neural network (CNN),^{139,142,143} in which rewards and penalties were utilized as pointers for the machine to figure out which actions to take in the unknown dynamical environment of different chemical systems, was employed to build our ML model. So far, we have studied ground state water (H₂O), triplet ground state methylene (³CH₂), and stretched H₂O (i.e., water in which the bond angle was fixed at the equilibrium value and the bond lengths symmetrically enlarged to 1.5 times their

equilibrium values). These three model systems are widely used in quantum chemistry to assess new methods, since they test a number of complementary challenges. The active space selection ability of our ML algorithm was then validated by comparing the suggested active space configurations from our model with the widely used configurations from published studies.

Computational Methods

Our ML model was built with the reinforcement learning algorithm, which was implemented in the PyTorch software package.¹⁵⁶ The ML model was used as a pre-processor program to our UNDMOL molecular software package³⁶ to generate several suggested active space configurations and provide good inputs for the GVVPT2 method. The initial optimization of equilibrium geometries as well as the initial molecular orbitals (MOs) of each molecular system were obtained with the restricted Hartree–Fock (RHF) approximation^{18–20,157} ahead of time. The restricted second-order Møller–Plesset perturbation theory (RMP2) method^{28,157,216–218} was then employed to include some of the effects of electron correlation to improve these MOs. The CNN in our ML model then generated different active spaces for each chemical system. MCSCF calculations were then carried out with these active space configurations to figure out which ones would generate good starting MOs for the GVVPT2 calculations. For our ML model, good active space configurations would satisfy four conditions which would work for most chemical systems:

1. The energy of highest occupied MO (HOMO) in the frozen core is lower than the energy of the lowest occupied MO in the valance space.

2. The energy of highest occupied MO (HOMO) in the frozen core is lower than the energy of the lowest unoccupied MO (LUMO) in the virtual space.
3. By adding in an extra orbital to the valence space, condition 1 and 2 are still satisfied, which means the energy surface can be extrapolated smoothly.
4. The dimension of the null and concave subspaces of the MCSCF both equal zero (i.e., $\dim(\text{null space}) = 0$ and $\dim(\text{concave space}) = 0$), which means that a local minimum (and not just stationary point) has been found.

Our ML routine started with the machine generating random configurations for the active space until a workable configuration, which did not result in an abnormal termination of the MCSCF calculation, was found. The workable configuration helped set a good starting point for the machine to learn from. The machine did not receive any rewards or suffer from any penalties during this random phase. When the machine arrived at the first workable configuration, its learning phase began. It then proceeded to compare the energies of the orbitals to see if condition 1 and 2 were satisfied. If condition 1 was met, it would earn 2 points as a reward. If both condition 1 and 2 were met, it would receive 5 points and proceed to test condition 3 and 4. A reward of 5 points would be distributed if condition 3 was met. If condition 4 was also satisfied, the configuration would become one of the suggested configurations for the active space and would be appended into the computer's memory. The machine would also receive 15 points as a big reward for finding this configuration and end the first episode.

If the workable configuration failed one of the four conditions, the machine would take one of these four actions: (i) move one orbital from the frozen core to the valence space, (ii) move one orbital from the valence space to the frozen core, (iii) move one orbital

from one symmetry to another symmetry in the same frozen core group (redistribute frozen core orbitals), and (iv) move one orbital from one symmetry to another symmetry in the same valence space group (redistribute valence orbitals), to arrive at the next configuration. If the action the machine took resulted in one of these failures: (i) abnormal termination of the MCSCF calculation, (ii) the number of valence electrons equals or is less than zero, and (iii) a negative value for virtual orbitals, the machine would suffer a 10-point loss as a penalty and end the episode. The machine would start the next episode by generating random configurations until it found the next workable configuration. If none of these three failures occurred, the machine would earn 5 points as a reward and continue to check the four conditions. The episode would end if one of these conditions was not satisfied and the machine went back to the random phase. If the machine found a viable configuration which met all the four conditions mentioned above, then the episode would also end. The rewards would be distributed for each satisfied condition as described earlier and the feasible configuration found by the machine would be appended to the computer's memory.

In the next episode, the machine would use the feasible configuration found in the last episode as a starting point, and then it would take one of the four actions to arrive at the next configuration. After that, it would go through the checking process for the three failure events and the four conditions. The machine would receive either rewards or penalties depending on the outcomes, and a new episode would begin. Every time the machine found a new viable configuration that met the four conditions, it would compare the MCSCF energy with the one from all the previous feasible configurations appended to the memory. If the MCSCF energy was lower than the previous ones, the machine would earn an extra 5-point reward for finding a better viable configuration. The routine continued

until the maximum number of episodes pre-determined by the user had been reached. All the viable configurations which had been appended to the memory would be printed out with the number of times the machine arrive at the same configuration. The schematic for our ML routine is shown in Figure VI-1. The suggested configurations found by the machine were compared with the widely used configurations from published studies to validate the active space selection ability of our ML model. Different parameters such as number of episodes and learning rates were also evaluated to determine which settings were optimal for the ground state H₂O, then these settings were used in the learning process for the triplet ground state ³CH₂ and the stretched H₂O.

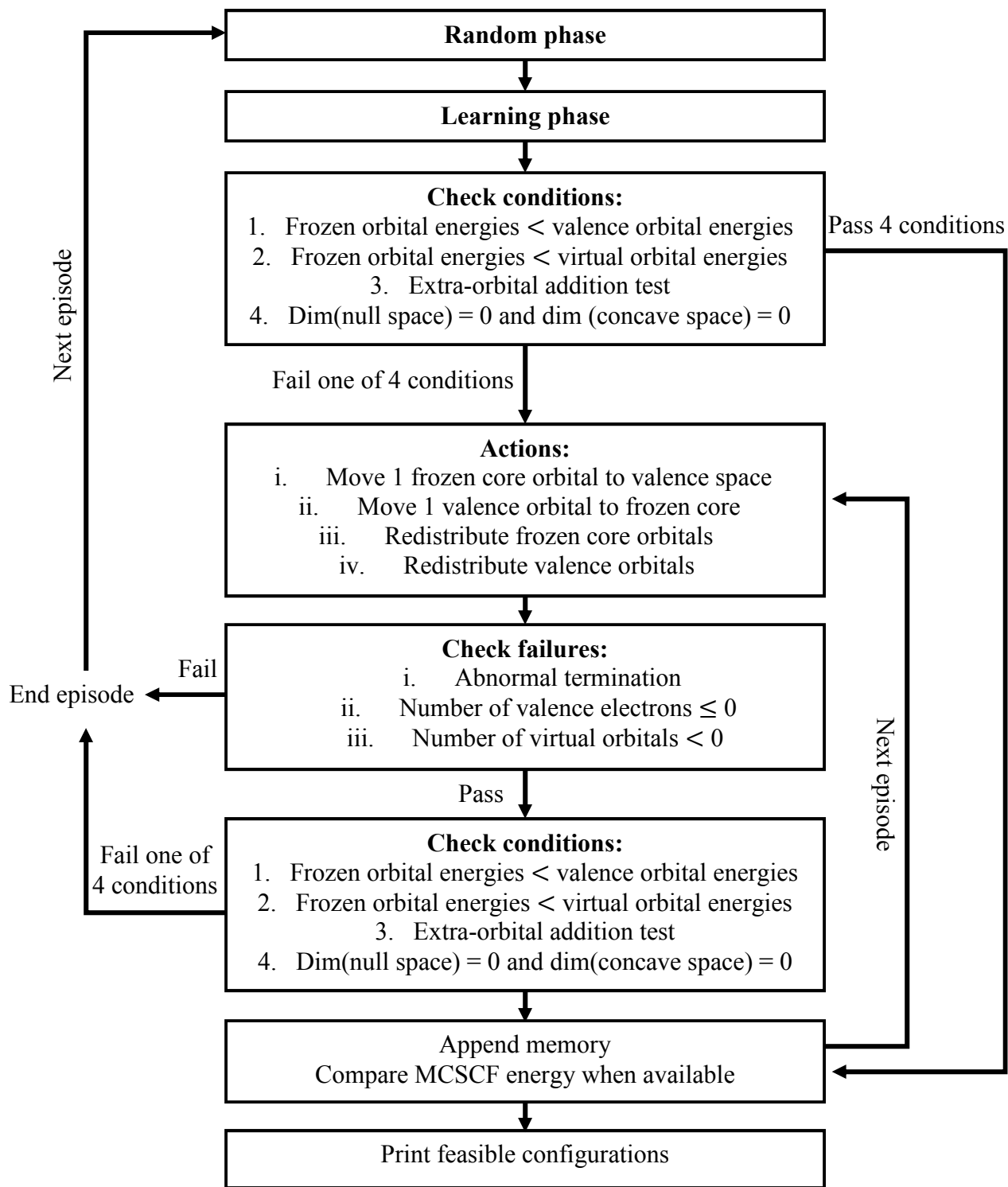


Figure VI-1. Schematic representation of our ML model.

Results and Discussion

The active space selection ability of our ML model was tested with ground state H₂O, triplet ground state ³CH₂, and stretched H₂O. The calculations of these three molecules was carried out with the DH (Dunning/Huzinaga double zeta) basis set³²⁵ and C_{2v} point group symmetry. For the H₂O molecule, the ML model was run three times each for different maximum number of episodes. Then the occurrence probabilities of the widely used configurations were determined for each of these maximum episode settings, using the formula below:

$$Probability(A) = \frac{Occurences\ of\ configuration\ A}{Total\ number\ of\ episodes} \quad (Eq.\ VI-1)$$

When the optimal episode parameter was established, different learning rates were then evaluated by also using the occurrence probabilities for finding the desired configurations. The learning rate (LR) determines how fast the machine can learn and has a value between 0 and 1. If LR = 0, the machine would not learn anything new. If LR = 1, the machine would completely discard the old experiences it had gained previously and would not learn from its mistakes. When testing different maximum number of episodes, we fixed LR to be 10⁻⁸, which is a slow LR so that the machine could learn from many of its good and bad configurations it had found in previous episodes. After the optimal number of maximum episodes was determined for each molecule, we fixed the episode setting while changing the LR. A faster LR of 10⁻⁴ and a slower LR of 10⁻¹² were tested to determine which LR the machine learned best at. The optimal episode and LR settings determined in the study of H₂O were then applied in the investigations of ³CH₂ and stretched H₂O.

In order to evaluate the learning process of our ML model, we used the mean squared error (MSE) loss function³²⁶ implemented in PyTorch to calculate the loss the

machine suffered from in each episode due to the wrong actions it took, which would result in it finding bad active space configurations. The loss, l_n , was calculated as the average of the squared differences between the actual values, x_n , and the target (or predicted) values, y_n , as given below:

$$l_n = (x_n - y_n)^2 \quad (\text{Eq. VI-2})$$

with n being the total number of episodes. In each episode, the machine predicted the next active space configuration, given the current configuration it had then and the action it planned to take. If the machine made a wrong prediction, the predicted value, y_n , would accumulate large number of penalties compared to its current state, reflected in x_n , resulting in a higher loss. The objective of the learning process is to minimize the loss, which means the machine had learnt from its mistakes and could make better prediction for the active space configurations in the next episode. At this early state of designing the ML model, we had to introduce random actions quite frequently during its learning phase, in which the machine would go back to the random phase every time it reached a configuration that would result in a negative value of electrons in the valance space. The purpose of the random actions is to prevent the machine from continuing to explore those bad configurations. However, since the model spaces of our three tested molecules are quite small, there are many configurations which would result in forcing the machine back to the random phase. Consequently, it is very difficult to graph the loss function due to much randomness and too many data points. In our future work, we intend to reduce the randomness by providing the machine with more conditions and more information about the target chemical systems so that the number of electrons will no longer trigger for the machine to go back to its random phase. We will also plan to pre-process the data points,

so that when we run larger sample sizes, the number of data points will not be one of our drawbacks.

A. Ground State Water (H₂O)

For the ground state H₂O molecule, the full valence active space contains 6 orbitals constructed from the $2s$ and $2p$ of oxygen (O), $1s$ of the first hydrogen (H), and $1s$ of the second H) with a total of 8 electrons. The most widely used configuration for the active space of H₂O is (3 0 1 2), which means the $2-4a_1$, $1b_1$, and $1-2b_2$ are in the valence space, with only the $1a_1$ orbital left in the frozen core (i.e., (1 0 0 0)).³²⁷⁻³³⁰ By moving the $2a_1$ orbital back into the frozen core (i.e., (2 0 0 0)), a smaller but also feasible active space configuration can be used for H₂O: (2 0 1 2) with 6 electrons.³²⁷ These are the two configurations we focused on to validate the active space selection ability of our ML model.

We ran the ML three times for each of the three maximum episode settings (i.e., 25,000, 50,000, and 75,000 episodes) to see how long the machine needed to be trained for in order to provide us with the two desired configurations for the active space of H₂O (see Table VI-1). The learning rate was fixed to be 10^{-8} . For a learning duration of 25,000 episodes, our ML model found the first configuration 14 times on average, and only encountered the second configuration twice on average. This means the average chance the machine could find the first configuration is 0.057% and the second one is 0.009% if the machine was only allowed to learn in 25,000 episodes. When the learning duration was increased to 50,000 episodes, the machine discovered the first configuration 42 times on average, which equals to an average of 0.085% chance, much higher than in the previous setting. However, configuration 2 can only be found 5 times on average, which is the same

as the probability of 0.009% in the 25,000-episode setting. When we increased the parameter to 75,000 episodes, the probabilities of finding these configurations were slightly lower – 0.080% (60 times on average) for configuration 1 and 0.006% (4 times on average) for configuration 2.

Table VI-1. The occurrences (times) and the occurrence probabilities (%) that our ML model found the desired configurations for H₂O in different learning durations.

	25,000 episodes	50,000 episodes	75,000 episodes
Configuration 1: Frozen core – (2 0 0 0), active space – (2 0 1 2)			
Trial 1	11 times 0.044%	48 times 0.096%	67 times 0.089%
Trial 2	17 times 0.068%	35 times 0.070%	59 times 0.079%
Trial 3	15 times 0.060%	44 times 0.088%	55 times 0.073%
Average	14 times 0.057%	42 times 0.085%	60 times 0.080%
Configuration 2: Frozen core – (1 0 0 0), active space – (3 0 1 2)			
Trial 1	2 times 0.008%	6 times 0.012%	4 times 0.005%
Trial 2	2 times 0.008%	3 times 0.006%	5 times 0.007%
Trial 3	3 times 0.012%	5 times 0.010%	4 times 0.005%
Average	2 times 0.009%	5 times 0.009%	4 times 0.006%

Table VI-1 shows that increasing the learning duration did not necessarily increase the probabilities of finding the desired configurations. This could be because as the learning duration got longer, it became more apparent that the machine tended to go back to some of the configurations that it had successfully found and received the most rewards in the previous episodes, instead of exploring more new configurations. Unfortunately, not all these successfully found configurations are feasible although they met all the conditions that we pre-determined for our machine. For instance, the configuration of (3 0 0 1) for the frozen core and (3 0 0 1) for the active space was discovered 36 times (0.144% finding chance) in trial 1 of the 25,000-episode run, although this is not a good configuration for the ground state H₂O due to the presence of too many a₁ orbitals but no b₁ orbitals. For our ML algorithm to eliminate these types of configurations, we would need to provide the machine with more information about orbital types along with their symmetries, which is plan for future work. At this state of the program, our ML can provide the user with a list of configurations in which some of them represent the appropriate active spaces, as shown in the case of the ground state H₂O (Table VI-1), the triplet ground state ³CH₂, and the stretched H₂O (shown in section B and C below). In the 25,000-episode runs, there was an average of 77 total configurations discovered by the machine. This number went up to 80 and 82 as the learning duration increased to 50,000 and 75,000 episodes, respectively (see Table VI-2), since the machine had more time to explore more configurations. However, as mentioned earlier, it does not necessarily indicate that the probabilities of finding the right configurations can be increased. More trials with more episode settings should be carried out to get a better understanding of the relation of sample size with orbital partitioning success. With some chemistry knowledge, the user could narrow down the lists

to a few appropriate configurations which would be good starting inputs for GVVPT2 calculations.

Table VI-2. The total number of configurations found by our ML model that met all the predetermined conditions. (LR = 10^{-8})

	25,000 episodes	50,000 episodes	75,000 episodes
Trial 1	78	77	81
Trial 2	76	83	83
Trial 3	77	80	83
Average	77	80	82

Based on Table VI-1, 50,000 episodes is a good setting to evaluate the effects of different LRs. We ran the ML three times each at a faster LR of 10^{-4} and a slower LR of 10^{-12} to determine which LR the machine learned best at. The data from Table VI-3 shows that, with LR = 10^{-4} , configurations 1 and 2 were found 39 and 3 times on average, respectively. This means there are 0.079% chance our ML protocol would find the first configuration, and 0.005% chance it would encounter the second one at this LR. These values are smaller than the ones from a slower LR of 10^{-8} . It indicates that a faster LR did not improve the chances of finding the desired configurations. The reason is that the machine continued discarding too much of the old data, so it did not learn a lot from its old mistakes. Consequently, the model kept starting over on bad configurations and did not improve its own learning progress.

As a result, we lowered the LR to 10^{-12} . The machine identified the first configuration 34 times on average, which equals 0.067% finding chance, and configuration

2 twice on average, which is 0.005%. By using a slower LR, the probabilities of finding the desired configurations decreased drastically. This is because with such a slow LR for a 50,000-episode learning duration, the algorithm did not have enough time to learn new pathways which could lead to the discoveries of more new active space configurations. Therefore, different LRs are suitable for different learning durations. However, in order to draw a better conclusion, more trials with larger testing samples (different molecules, LRs, and maximum numbers of episodes) need to be conducted. With the data we obtained so far, we decided to use $LR = 10^{-8}$ and maximum episodes = 50,000 as the fixed parameters to test the active space selection ability of our ML model in the case of the triplet ground state $^3\text{CH}_2$ and the stretched H_2O .

Table VI-3. The occurrences (times) and the occurrence probabilities (%) that our ML model found the desired configurations for H₂O using different LRs with 50,000 as the maximum number of episodes.

	10^{-4}	10^{-8}	10^{-12}
Configuration 1: Frozen core – (2 0 0 0), active space – (2 0 1 2)			
Trial 1	38 times 0.076%	48 times 0.096%	30 times 0.060%
Trial 2	42 times 0.084%	35 times 0.070%	31 times 0.062%
Trial 3	38 times 0.076%	44 times 0.088%	40 times 0.080%
Average	39 times 0.079%	42 times 0.085%	34 times 0.067%
Configuration 2: Frozen core – (1 0 0 0), active space – (3 0 1 2)			
Trial 1	2 times 0.004%	6 times 0.012%	4 times 0.008%
Trial 2	3 times 0.006%	3 times 0.006%	2 times 0.004%
Trial 3	3 times 0.006%	5 times 0.010%	1 time 0.002%
Average	3 times 0.005%	5 times 0.009%	2 times 0.005%

There is another feasible active space configuration that could be used for H₂O molecule. It contains 3–4a₁ and 1–2b₂ (i.e., (2 0 0 2)) with 4 electrons and the 1–2a₁ and 1b₁ are in the frozen core (i.e., (2 0 1 0)).³²⁷ Our ML model did not find this configuration because condition 1 strictly forbade the machine from choosing a configuration that would result in a frozen core orbital with higher energy than the valence orbitals. We implemented this condition because it will work for most cases. However, for this special case with (2 0 0 2) as an active space, the 1b₁ orbital remains in the frozen core but has higher energy than the lowest occupied MOs in the valence space. Thus, our future plan is to modify condition 1 to allow a small overlap of energies between the frozen core and the valence space with the purpose that our ML model could find the configurations for these special cases.

B. Triplet Ground State Methylene (³CH₂)

For the triplet ground state ³CH₂ radical, the full valence active space contains 6 orbitals (i.e., 2s and 2p of carbon (C), 1s of the first hydrogen (H), and 1s of the second H) and 6 electrons. The configuration often used for its active space is (3 0 1 2), which means the 2–4a₁, 1b₁, and 1–2b₂ are in the valence space, with only the 1a₁ orbital left in the frozen core (i.e., (1 0 0 0)).^{331,332} Similar to H₂O, a smaller active space configuration can also be used for ³CH₂, which is (2 0 1 2) with 4 electrons and the frozen core contains the 1–2a₁ orbitals (i.e., (2 0 0 0)). This active space might be too small, but it is a good starting point that the machine should have in its list of feasible configurations. Hence, these are the two desired configurations for the ³CH₂ radical.

Since 50,000 episodes and a LR of 10⁻⁸ are the best settings we found so far for our model, we applied these parameters in the calculations of the triplet ground state ³CH₂.

Unfortunately, with these settings, the machine did not find either of these desired configurations. The configuration that it identified with the most number occurrences (112 times with 0.224% finding chance) is (3 0 0 0) for the frozen core and (2 0 1 1) for the active space with 2 electrons. This means 1–3a₁ orbitals are left inactive while the valence space includes 4–5a₁, 1b₁, and 1b₂ orbitals. The configuration that looks very close to the optimal ones is (2 0 0 0) for the frozen core and (1 0 2 2) for the active space (i.e., 1–2a₁ orbitals are left inactive while the valence space includes 3a₁, 1–2b₁, and 1–2b₂ orbitals). This configuration was found by the machine 33 times, which equals to a probability of 0.066%.

In order to evaluate the two most feasible active space configurations that our ML model had discovered, we carried out GVVPT2 calculations using these configurations and the DH basis set, and then compare their energies with the GVVPT2 energy obtained from the optimal configuration (frozen core – (1 0 0 0), active space – (3 0 1 2)). For these calculations, we used the experimental values of the ground state ³CH₂ geometry parameters (i.e., the C–H bond length = 1.078 Å and the H–C–H bond angle = 136°)^{333–337} (see Figure VI-2). The comparison of these electronic energies is shown in Table VI-4.

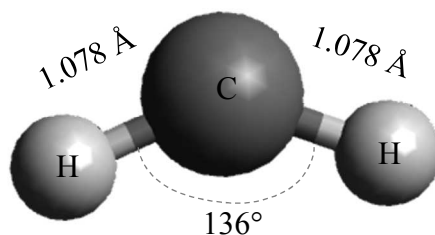


Figure VI-2. Equilibrium structure of ³CH₂ constructed from the experimental values of its geometry parameters.

The electronic energy of the triplet ground state $^3\text{CH}_2$ calculated at the GVVPT2/DH level using the optimal configuration (configuration 1) is -38.6730 a.u. (see Table VI-4). When the second configuration, which is the one our ML model had found with the greatest number of occurrences, was used, the GVVPT2 energy of $^3\text{CH}_2$ turned out to be higher (by approximately 1.0923 a.u.). It indicates that this configuration is not as good as the optimal one. The energy computed using configuration 3, which is also in the list of configurations suggested by the machine, is much closer to the result from the optimal configuration (higher by 0.2233 a.u.). This means the ML algorithm had found us a good starting active space configuration for GVVPT2 calculations. Although the machine did not successfully locate the optimal one, both configuration 2 and 3 would help the user come close to finding a proper active space. Additionally, it is possible that the learning parameter of 50,000 episodes and the LR of 10^{-8} are not the right settings for the $^3\text{CH}_2$ radical. We might need to experiment with different settings to figure out what is the average probability for our ML model to reach to optimal configuration. We also included the electronic energy of $^3\text{CH}_2$ from the parametric two-electron reduced density matrix (P2RDM)/cc-pV5Z method³³⁷ to provide better comparisons. The reason that our GVVPT2 electronic energies are all higher when being compared to the data from this published study is due in part to method and to the larger basis set for these calculations.

Table VI-4. Comparison of electronic energies of ${}^3\text{CH}_2$ computed with different active space configurations at the GVVPT2/DH level. The data from published literature is also included.

Configuration	Energy (a.u.)
1: Frozen core – (1 0 0 0), active space – (3 0 1 2)	-38.6730
2: Frozen core – (3 0 0 0), active space – (2 0 1 1)	-37.5807
3: Frozen core – (2 0 0 0), active space – (1 0 2 2)	-38.4497
P2RDM/cc-pV5Z ³³⁷	-39.1236

C. Stretched Water (H_2O)

For the stretched H_2O , we kept the bond angle fixed to the equilibrium value of the ground state H_2O (104.5°),³³⁸ and the O–H bond lengths were stretched to 1.466 \AA , which is approximately $1.5R_e$, with the equilibrium O–H bond lengths (R_e) equal 0.958 \AA)^{328,338} as shown in Figure VI-3. In order to describe this symmetric stretching of both O–H single bonds, larger active spaces than the one used for the ground state H_2O are often used. Instead of the 6 orbitals (i.e., $2s$ and $2p$ of carbon (O), $1s$ of the first hydrogen (H), and $1s$ of the second H) with 8 electrons as included in the full valence active space of the ground state H_2O , two extra Rydberg orbitals are often added to the active space for the stretched H_2O . There are three active spaces that have been described in previously published studies:^{328,329} (4 0 2 2) for the ${}^1\text{A}_1$ states (i.e., the $2-5a_1$, $1-2b_1$, and $1-2b_2$ are in the valence space); (5 0 1 2) for the ${}^1\text{B}_1$ states (i.e., the $2-6a_1$, $1b_1$, and $1-2b_2$ are in the valence space); and (3 1 1 4) for the ${}^1\text{A}_2$ states (i.e., the $2-4a_1$, $1a_2$, $1b_1$, and $1-4b_2$ are in the valence space). The $1a_1$ orbital is left inactive in the frozen core (i.e., (1 0 0 0)) for all these three configurations. However, we only used the configuration for the ${}^1\text{A}_1$ states as the desired

configuration to test the active space selection ability of our ML model in the case of the stretched H_2O .

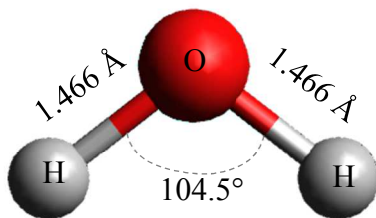


Figure VI-3. Structure of the stretched water constructed from the experimental values of its geometry parameters.

In the case of ground state H_2O and triplet ground state $^3\text{CH}_2$, we placed an input of 7 orbitals as a starting number for the machine to begin exploring different configurations. However, for the stretched H_2O , we increased that number to 9 orbitals, so that the machine could have a better starting point for its search. Since 50,000 episodes and a LR of 10^{-8} are the best settings we had found so far for the case of ground state H_2O , we applied these parameters in the calculations of the stretched H_2O . Unfortunately, with these settings, the machine did not find the desired configuration. The configuration that it discovered with the most number occurrences (37 times with 0.074% finding chance) is (3 0 0 0) for the frozen core and (4 0 1 1) for the active space with 4 electrons. This means the 1–3 a_1 orbitals are left inactive while the valence space includes 4–7 a_1 , 1 b_1 , and 1 b_2 orbitals. The configuration that looks very close to the optimal one is (1 0 0 0) for the frozen core and (3 0 2 3) for the active space (i.e., the 1 a_1 orbital is left inactive while the valence space includes 2–4 a_1 , 1–2 b_1 , and 1–3 b_2 orbitals). This configuration was found by the machine 14 times, which equals to a probability of 0.028%. To evaluate the two most feasible active space configurations that our ML model had identified, we carried out

GVVPT2 calculations using these configurations and the DH basis set, and then compared their energies with the GVVPT2 energy obtained from the optimal configuration (frozen core – (1 0 0 0), active space – (4 0 2 2)).

The electronic energy of the stretched H₂O calculated at the GVVPT2/DH level using the optimal configuration (configuration 1) is -75.8443 a.u. (as shown in Table VI-5). The energy from the second configuration, which is the one our ML model had found with the greatest number of occurrences, is slightly higher (by approximately 0.0308 a.u.). It indicates that this configuration is not a bad one when being compared to the optimal one. The energy computed using configuration 3, which is also in the list of configurations suggested by the machine, is very close to the result from the optimal configuration (only higher by 0.0017 a.u.). This means the ML algorithm had found us a very good starting active space configuration for GVVPT2 calculations. Similar to the case of the triplet ground state ³CH₂, the machine did not successfully locate the optimal one, and it could happen due to inappropriate settings for the learning process. However, both configuration 2 and 3 are comparable to the optimal configuration because their differences in energies are negligible.

Table VI-5. Comparison of electronic energies of the stretched H₂O computed with different active space configurations at the GVVPT2/DH level.

Configuration	Energy (a.u.)
1: Frozen core – (1 0 0 0), active space – (4 0 2 2)	-75.8443
2: Frozen core – (3 0 0 0), active space – (4 0 1 1)	-75.8135
3: Frozen core – (1 0 0 0), active space – (3 0 2 3)	-75.8426

Conclusions

In this work, we used the reinforcement learning approach to design our ML model with the objective that we could solve the user-specified active space problem within the GVVPT2 method. In every run of the ML routine, the machine would set out to explore the unknown dynamical environment of the target chemical systems. The rewards and penalties were provided during its learning process as pointers to help it figure out which actions to take. So far, we have tested the ML algorithm on three molecules: the ground state water (H_2O), the triplet ground state methylene ($^3\text{CH}_2$), and the stretched H_2O . For the case of ground state H_2O , 50,000 episodes and a LR of 10^{-8} appeared to be the optimal settings for the machine to find the desired configurations. However, these settings seemed to fail for the other two molecules. On the other hand, the machine did find other feasible configurations that are comparable to the desired ones for these two cases. The active space selection ability of our ML algorithm was validated by comparing the GVVPT2 energies calculated using the configurations suggested by the machine with the values from the optimal ones. The results indicate that these suggested configurations could be good starting points for GVVPT2 calculations.

For our future work, we plan to test our ML model with more complicated chemical systems as well as different learning parameters to determine the degree of transferability that the model has to offer. In addition, we intend to provide the machine with more information, including the characteristics of each element in the target chemical systems, as well as the types of orbitals and their corresponding symmetries, so that the ML model could find more proper active spaces. Also, we would like to implement the macroconfiguration approach into the ML protocol. This would enable the ability to test

larger chemical systems, compared to the CAS ansatz currently employed in the machine's active space configuring process. Our goal is to build a smarter and more efficient ML model which could help systematize the active space selection and explore more unknown systems.

CONCLUDING REMARKS AND FUTURE DIRECTIONS

The projects described in this dissertation have showcased the ability of *ab initio* electronic structure methods in studying different types of chemical systems. The theoretical studies of Ir-Si monolayers presented in chapter III illustrate the effectiveness of the DFT method in exploring new solid-state materials. While DFT continues to be rightfully regarded as effective and efficient for stable molecular and larger systems, the search for efficient, systematically improvable wavefunction-based approaches remains an important goal for studying molecules with unusual electronic structures. Concomitantly, identifying molecules that require such precise methods is an on-going challenge. In this dissertation, it was shown that the reactive astrophysical radicals CaOH and SrOH, which were hitherto only well described by very computationally resource intensive methods such as MRCI and CCSD, could be studied by the GVVPT2 method. The GVVPT2 has the ability to provide balanced descriptions of dynamic and static electron correlations, as shown in chapter IV. This is particularly important for studying larger systems for which MRCI and CCSD are no longer feasible. In addition to choosing the right method for the right systems, it is important to choose the right basis sets and model spaces. Improper choices could lead to inaccurate results or incapability to reach convergence.

The challenges in the active space selection protocol have motivated us to use ML to systematize this process. We chose the reinforcement learning algorithm as the foundation to build our ML routine so that the model can later be implemented in the studies of different unknown systems. Although the ML program is still in its early state,

chapter VI has demonstrated that our model could help solve the user-specified active space problem within GVVPT2.

For the studies of CaOH and SrOH, our future plan is to investigate their low-lying excited states and their dimerization pathways to have a better understanding of the characteristics of these molecules along with their potential applications in the laser cooling technologies. The future directions for the ML project include programming the machine to have more awareness of the chemical environments around target molecules as well as testing the model on larger systems to determine its transferability between different molecular structures. If we could improve the active space selection ability of the machine, it would open more opportunities for the search of new materials on Earth and in space.

REFERENCES

- (1) Niu, S.; Hall, M. B. Theoretical Studies on Reactions of Transition-Metal Complexes. *Chem. Rev.* **2000**, *100*, 353–406.
- (2) Comba, P.; Kerscher, M. Computation of Structures and Properties of Transition Metal Compounds. *Coord. Chem. Rev.* **2009**, *253*, 564–574.
- (3) Vogiatzis, K. D.; Polynski, M. V; Kirkland, J. K.; Townsend, J.; Hashemi, A.; Liu, C.; Pidko, E. A. Computational Approach to Molecular Catalysis by 3d Transition Metals: Challenges and Opportunities. *Chem. Rev.* **2019**, *119*, 2453–2523.
- (4) Kodikara, M. S.; Stranger, R.; Humphrey, M. G. Computational Studies of the Nonlinear Optical Properties of Organometallic Complexes. *Coord. Chem. Rev.* **2018**, *375*, 389–409.
- (5) Sperger, T.; Sanhueza, I. A.; Kalvet, I.; Schoenebeck, F. Computational Studies of Synthetically Relevant Homogeneous Organometallic Catalysis Involving Ni, Pd, Ir, and Rh: An Overview of Commonly Employed DFT Methods and Mechanistic Insights. *Chem. Rev.* **2015**, *115*, 9532–9586.
- (6) González, L.; Escudero, D.; Serrano-Andrés, L. Progress and Challenges in the Calculation of Electronic Excited States. *ChemPhysChem* **2012**, *13*, 28–51.
- (7) Hafner, J. Ab-Initio Simulations of Materials Using VASP: Density-Functional Theory and Beyond. *J. Comput. Chem.* **2008**, *29*, 2044–2078.
- (8) Zhu, Z.; Guan, J.; Tománek, D. Strain-Induced Metal-Semiconductor Transition in Monolayers and Bilayers of Gray Arsenic: A Computational Study. *Phys. Rev. B*

- 2015**, *91*, 161404.
- (9) Groves, C. Simulating Charge Transport in Organic Semiconductors and Devices: A Review. *Reports Prog. Phys.* **2016**, *80*, 26502.
 - (10) Wang, X.; Li, T.; Cheng, Z.; Wang, X.-L.; Chen, H. Recent Advances in Dirac Spin-Gapless Semiconductors. *Appl. Phys. Rev.* **2018**, *5*, 41103.
 - (11) Hu, H.; Yang, W. Free Energies of Chemical Reactions in Solution and in Enzymes with Ab Initio Quantum Mechanics/Molecular Mechanics Methods. *Annu. Rev. Phys. Chem.* **2008**, *59*, 573–601.
 - (12) Cole, D. J.; Hine, N. D. M. Applications of Large-Scale Density Functional Theory in Biology. *J. Phys. Condens. Matter* **2016**, *28*, 393001.
 - (13) Dirac, P. A. M.; Fowler, R. H. Quantum Mechanics of Many-Electron Systems. *Proc. Math. Phys. Eng. Sci.* **1929**, *123*, 714–733.
 - (14) Tew, D. P.; Klopper, W.; Helgaker, T. Electron Correlation: The Many-Body Problem at the Heart of Chemistry. *J. Comput. Chem.* **2007**, *28*, 1307–1320.
 - (15) Schrödinger, E. An Undulatory Theory of the Mechanics of Atoms and Molecules. *Phys. Rev.* **1926**, *28*, 1049–1070.
 - (16) Raghavachari, K.; Anderson, J. B. Electron Correlation Effects in Molecules. *J. Phys. Chem.* **1996**, *100*, 12960–12973.
 - (17) Pople, J. A.; Binkley, J. S.; Seeger, R. Theoretical Models Incorporating Electron Correlation. *Int. J. Quantum Chem.* **1976**, *10*, 1–19.
 - (18) Hartree, D. R. The Wave Mechanics of an Atom with a Non-Coulomb Central Field. Part I. Theory and Methods. *Math. Proc. Cambridge Philos. Soc.* **1928**, *24*, 89–110.
 - (19) Fock, V. Näherungsmethode Zur Lösung Des Quantenmechanischen

- Mehrkörperprobleme. *Z. Phys.* **1930**, *61*, 126–148.
- (20) Slater, J. C. Note on Hartree's Method. *Phys. Rev.* **1930**, *35*, 210–211.
- (21) Echenique, P.; Alonso, J. L. A Mathematical and Computational Review of Hartree–Fock SCF Methods in Quantum Chemistry. *Mol. Phys.* **2007**, *105*, 3057–3098.
- (22) Ghosh, S.; Verma, P.; Cramer, C. J.; Gagliardi, L.; Truhlar, D. G. Combining Wave Function Methods with Density Functional Theory for Excited States. *Chem. Rev.* **2018**, *118*, 7249–7292.
- (23) Rimola, A.; Ferrero, S.; Germain, A.; Corno, M.; Ugliengo, P. Computational Surface Modelling of Ices and Minerals of Interstellar Interest—Insights and Perspectives. *Minerals* **2021**, *11*, 26.
- (24) Shavitt, I. The Method of Configuration Interaction. In *Methods of Electronic Structure Theory*; Schaefer III, H. F., Ed.; Springer US: Boston, MA, 1977; pp 189–275.
- (25) Shavitt, I. The History and Evolution of Configuration Interaction. *Mol. Phys.* **1998**, *94*, 3–17.
- (26) Sherrill, C. D.; Schaefer III, H. F. The Configuration Interaction Method: Advances in Highly Correlated Approaches. In *Advances in Quantum Chemistry*; Löwdin, P.-O., Sabin, J. R., Zerner, M. C., Brändas, E., Eds.; Academic Press: San Diego, 1999; Vol. 34, pp 143–269.
- (27) Čársky, P. Configuration Interaction. In *Encyclopedia of Computational Chemistry*; Schleyer, P. v. R., Clark, N. L., Gasteiger, J., Schaefer III, H. F., Schreiner, P. R., Eds.; Wiley: Chichester, 1998; pp 485–497.
- (28) Møller, C.; Plesset, M. S. Note on an Approximation Treatment for Many-Electron

- Systems. *Phys. Rev.* **1934**, *46*, 618–622.
- (29) Gauss, J. Coupled-Cluster Theory. In *Encyclopedia of Computational Chemistry*; Schleyer, P. v. R., Allinger, N. L., Clark, T., Gasteiger, J., Kollman, P. A., Schaefer III, H. F., Schreiner, P. R., Eds.; Wiley: Chichester, 1998; pp 615–636.
- (30) Buenker, R. J.; Peyerimhoff, S. D.; Butscher, W. Applicability of the Multi-Reference Double-Excitation CI (MRD-CI) Method to the Calculation of Electronic Wavefunctions and Comparison with Related Techniques. *Mol. Phys.* **1978**, *35*, 771–791.
- (31) Szalay, P. G.; Müller, T.; Gidofalvi, G.; Lischka, H.; Shepard, R. Multiconfiguration Self-Consistent Field and Multireference Configuration Interaction Methods and Applications. *Chem. Rev.* **2012**, *112*, 108–181.
- (32) Roos, B. O.; Linse, P.; Siegbahn, P. E. M.; Blomberg, M. R. A. A Simple Method for the Evaluation of the Second-Order-Perturbation Energy from External Double-Excitations with a CASSCF Reference Wavefunction. *Chem. Phys.* **1982**, *66*, 197–207.
- (33) Andersson, K.; Malmqvist, P. A.; Roos, B. O.; Sadlej, A. J.; Wolinski, K. Second-Order Perturbation Theory with a CASSCF Reference Function. *J. Phys. Chem.* **1990**, *94*, 5483–5488.
- (34) Andersson, K.; Malmqvist, P.; Roos, B. O. Second-order Perturbation Theory with a Complete Active Space Self-consistent Field Reference Function. *J. Chem. Phys.* **1992**, *96*, 1218–1226.
- (35) Werner, H.-J. Third-Order Multireference Perturbation Theory The CASPT3 Method. *Mol. Phys.* **1996**, *89*, 645–661.

- (36) Jiang, W.; Khait, Y. G.; Hoffmann, M. R. Configuration-Driven Unitary Group Approach for Generalized Van Vleck Variant Multireference Perturbation Theory. *J. Phys. Chem. A* **2009**, *113*, 4374–4380.
- (37) Schmidt, M. W.; Gordon, M. S. The Construction and Interpretation of MCSCF Wavefunctions. *Annu. Rev. Phys. Chem.* **1998**, *49*, 233–266.
- (38) Shepard, R. The Multiconfiguration Self-Consistent Field Method. In *Advances in Chemical Physics*; Lawley, K. P., Ed.; John Wiley & Sons: New York, 1987; pp 63–200.
- (39) Köhn, A.; Hanauer, M.; Mück, L. A.; Jagau, T.-C.; Gauss, J. State-Specific Multireference Coupled-Cluster Theory. *Wiley Interdiscip. Rev. Comput. Mol. Sci.* **2013**, *3*, 176–197.
- (40) Čárský, P.; Paldus, J.; Pittner, J. *Recent Progress in Coupled Cluster Methods : Theory and Applications*; Springer: Dordrecht; New York, 2010.
- (41) Hohenberg, P.; Kohn, W. Inhomogeneous Electron Gas. *Phys. Rev.* **1964**, *136*, B864–B871.
- (42) Kohn, W.; Sham, L. J. Self-Consistent Equations Including Exchange and Correlation Effects. *Phys. Rev.* **1965**, *140*, A1133–A1138.
- (43) Pople, J. A.; Gill, P. M. W.; Johnson, B. G. Kohn—Sham Density-Functional Theory within a Finite Basis Set. *Chem. Phys. Lett.* **1992**, *199*, 557–560.
- (44) Parr, R. G.; Yang, W. *Density-Functional Theory of Atoms and Molecules*; Oxford University Press: New York, 1995.
- (45) Kohn, W.; Becke, A. D.; Parr, R. G. Density Functional Theory of Electronic Structure. *J. Phys. Chem.* **1996**, *100*, 12974–12980.

- (46) Mardirossian, N.; Head-Gordon, M. Thirty Years of Density Functional Theory in Computational Chemistry: An Overview and Extensive Assessment of 200 Density Functionals. *Mol. Phys.* **2017**, *115*, 2315–2372.
- (47) Bickelhaupt, F. M.; Baerends, E. J. Kohn-Sham Density Functional Theory: Predicting and Understanding Chemistry. In *Reviews in Computational Chemistry*; Lipkowitz, K. B., Boyd, D. B., Eds.; John Wiley & Sons: New Jersey, 2007; pp 1–86.
- (48) Dreuw, A.; Head-Gordon, M. Single-Reference Ab Initio Methods for the Calculation of Excited States of Large Molecules. *Chem. Rev.* **2005**, *105*, 4009–4037.
- (49) Yu, H. S.; Li, S. L.; Truhlar, D. G. Perspective: Kohn-Sham Density Functional Theory Descending a Staircase. *J. Chem. Phys.* **2016**, *145*, 130901.
- (50) Tsuneda, T. *Density Functional Theory in Quantum Chemistry*; Springer: Tokyo, Japan, 2014.
- (51) Thiel, W. Semiempirical Quantum–Chemical Methods. *Wiley Interdiscip. Rev. Comput. Mol. Sci.* **2014**, *4*, 145–157.
- (52) Pan, J. Scaling up System Size in Materials Simulation. *Nat. Comput. Sci.* **2021**, *1*, 95.
- (53) Dewar, M. J. S.; Thiel, W. Ground States of Molecules. 38. The MNDO Method. Approximations and Parameters. *J. Am. Chem. Soc.* **1977**, *99*, 4899–4907.
- (54) Dewar, M. J. S.; Zoebisch, E. G.; Healy, E. F.; Stewart, J. J. P. Development and Use of Quantum Mechanical Molecular Models. 76. AM1: A New General Purpose Quantum Mechanical Molecular Model. *J. Am. Chem. Soc.* **1985**, *107*, 3902–3909.

- (55) Stewart, J. J. P. Optimization of Parameters for Semiempirical Methods I. Method. *J. Comput. Chem.* **1989**, *10*, 209–220.
- (56) Stewart, J. J. P. Optimization of Parameters for Semiempirical Methods II. Applications. *J. Comput. Chem.* **1989**, *10*, 221–264.
- (57) Allinger, N. L. Conformational Analysis. 130. MM2. A Hydrocarbon Force Field Utilizing V1 and V2 Torsional Terms. *J. Am. Chem. Soc.* **1977**, *99*, 8127–8134.
- (58) Case, D. A.; Cheatham, T. E. 3rd; Darden, T.; Gohlke, H.; Luo, R.; Merz, K. M. J.; Onufriev, A.; Simmerling, C.; Wang, B.; Woods, R. J. The Amber Biomolecular Simulation Programs. *J. Comput. Chem.* **2005**, *26*, 1668–1688.
- (59) Christensen, A. S.; Kubař, T.; Cui, Q.; Elstner, M. Semiempirical Quantum Mechanical Methods for Noncovalent Interactions for Chemical and Biochemical Applications. *Chem. Rev.* **2016**, *116*, 5301–5337.
- (60) Zheng, M.; Waller, M. P. Adaptive Quantum Mechanics/Molecular Mechanics Methods. *Wiley Interdiscip. Rev. Comput. Mol. Sci.* **2016**, *6*, 369–385.
- (61) Grimme, S.; Antony, J.; Ehrlich, S.; Krieg, H. A Consistent and Accurate Ab Initio Parametrization of Density Functional Dispersion Correction (DFT-D) for the 94 Elements H-Pu. *J. Chem. Phys.* **2010**, *132*, 154104.
- (62) Schwabe, T.; Grimme, S. Theoretical Thermodynamics for Large Molecules: Walking the Thin Line between Accuracy and Computational Cost. *Acc. Chem. Res.* **2008**, *41*, 569–579.
- (63) Antony, J.; Grimme, S.; Liakos, D. G.; Neese, F. Protein-Ligand Interaction Energies with Dispersion Corrected Density Functional Theory and High-Level Wave Function Based Methods. *J. Phys. Chem. A* **2011**, *115*, 11210–11220.

- (64) Lonsdale, R.; Harvey, J. N.; Mulholland, A. J. Effects of Dispersion in Density Functional Based Quantum Mechanical/Molecular Mechanical Calculations on Cytochrome P450 Catalyzed Reactions. *J. Chem. Theory Comput.* **2012**, *8*, 4637–4645.
- (65) Moellmann, J.; Grimme, S. DFT-D3 Study of Some Molecular Crystals. *J. Phys. Chem. C* **2014**, *118*, 7615–7621.
- (66) Zhang, H.-M.; Chen, S.-L. Include Dispersion in Quantum Chemical Modeling of Enzymatic Reactions: The Case of Isoaspartyl Dipeptidase. *J. Chem. Theory Comput.* **2015**, *11*, 2525–2535.
- (67) Goerigk, L. Chapter 6 - A Comprehensive Overview of the DFT-D3 London-Dispersion Correction. In *Non-Covalent Interactions in Quantum Chemistry and Physics*; Otero de la Roza, A., DiLabio, G., Eds.; Elsevier: Amsterdam, Netherlands, 2017; pp 195–219.
- (68) Grimme, S.; Ehrlich, S.; Goerigk, L. Effect of the Damping Function in Dispersion Corrected Density Functional Theory. *J. Comput. Chem.* **2011**, *32*, 1456–1465.
- (69) Novoselov, K. S.; Geim, A. K.; Morozov, S. V; Jiang, D.; Zhang, Y.; Dubonos, S. V; Grigorieva, I. V; Firsov, A. A. Electric Field Effect in Atomically Thin Carbon Films. *Science (80-.)*. **2004**, *306*, 666–669.
- (70) Geim, A. K.; Novoselov, K. S. The Rise of Graphene. *Nat Mater* **2007**, *6*, 183–191.
- (71) Novoselov, K. S.; Geim, A. K.; Morozov, S. V; Jiang, D.; Katsnelson, M. I.; Grigorieva, I. V; Dubonos, S. V; Firsov, A. A. Two-Dimensional Gas of Massless Dirac Fermions in Graphene. *Nature* **2005**, *438*, 197–200.
- (72) Bolotin, K. I.; Sikes, K. J.; Jiang, Z.; Klima, M.; Fudenberg, G.; Hone, J.; Kim, P.;

- Stormer, H. L. Ultrahigh Electron Mobility in Suspended Graphene. *Solid State Commun.* **2008**, *146*, 351–355.
- (73) Castro Neto, A. H.; Guinea, F.; Peres, N. M. R.; Novoselov, K. S.; Geim, A. K. The Electronic Properties of Graphene. *Rev. Mod. Phys.* **2009**, *81*, 109–162.
- (74) Das Sarma, S.; Adam, S.; Hwang, E. H.; Rossi, E. Electronic Transport in Two-Dimensional Graphene. *Rev. Mod. Phys.* **2011**, *83*, 407–470.
- (75) Tao, L.; Cinquanta, E.; Chiappe, D.; Grazianetti, C.; Fanciulli, M.; Dubey, M.; Molle, A.; Akinwande, D. Silicene Field-Effect Transistors Operating at Room Temperature. *Nat Nano* **2015**, *10*, 227–231.
- (76) Zhang, X.; Xie, H.; Hu, M.; Bao, H.; Yue, S.; Qin, G.; Su, G. Thermal Conductivity of Silicene Calculated Using an Optimized Stillinger-Weber Potential. *Phys. Rev. B* **2014**, *89*, 54310.
- (77) Guzmán-Verri, G. G.; Lew Yan Voon, L. C. Electronic Structure of Silicon-Based Nanostructures. *Phys. Rev. B* **2007**, *76*, 75131.
- (78) Zhao, J.; Liu, H.; Yu, Z.; Quhe, R.; Zhou, S.; Wang, Y.; Liu, C. C.; Zhong, H.; Han, N.; Lu, J.; Yao, Y.; Wu, K. Rise of Silicene: A Competitive 2D Material. *Prog. Mater. Sci.* **2016**, *83*, 24–151.
- (79) Vogt, P.; De Padova, P.; Quaresima, C.; Avila, J.; Frantzeskakis, E.; Asensio, M. C.; Resta, A.; Ealet, B.; Le Lay, G. Silicene: Compelling Experimental Evidence for Graphenelike Two-Dimensional Silicon. *Phys. Rev. Lett.* **2012**, *108*, 155501.
- (80) Kara, A.; Enriquez, H.; Seitsonen, A. P.; Voon, L. C. L. Y.; Vizzini, S.; Aufray, B.; Oughaddou, H. A Review on Silicene — New Candidate for Electronics. *Surf. Sci. Rep.* **2012**, *67*, 1–18.

- (81) Le Lay, G. 2D Materials: Silicene Transistors. *Nat Nano* **2015**, *10*, 202–203.
- (82) Shao, Z.-G.; Ye, X.-S.; Yang, L.; Wang, C.-L. First-Principles Calculation of Intrinsic Carrier Mobility of Silicene. *J. Appl. Phys.* **2013**, *114*, 93712.
- (83) Ye, X.-S.; Shao, Z.-G.; Zhao, H.; Yang, L.; Wang, C.-L. Intrinsic Carrier Mobility of Germanene Is Larger than Graphene's: First-Principle Calculations. *RSC Adv.* **2014**, *4*, 21216–21220.
- (84) Kane, C. L.; Mele, E. J. Quantum Spin Hall Effect in Graphene. *Phys. Rev. Lett.* **2005**, *95*, 226801.
- (85) Ezawa, M. A Topological Insulator and Helical Zero Mode in Silicene under an Inhomogeneous Electric Field. *New J. Phys.* **2012**, *14*, 33003.
- (86) Tahir, M.; Schwingenschlögl, U. Valley Polarized Quantum Hall Effect and Topological Insulator Phase Transitions in Silicene. *Sci. Rep.* **2013**, *3*, 1075.
- (87) Ezawa, M. Monolayer Topological Insulators: Silicene, Germanene, and Stanene. *J. Phys. Soc. Japan* **2015**, *84*, 121003.
- (88) Zhang, Y.; Tan, Y.-W.; Stormer, H. L.; Kim, P. Experimental Observation of the Quantum Hall Effect and Berry's Phase in Graphene. *Nature* **2005**, *438*, 201–204.
- (89) Liu, C.-C.; Feng, W.; Yao, Y. Quantum Spin Hall Effect in Silicene and Two-Dimensional Germanium. *Phys. Rev. Lett.* **2011**, *107*, 76802.
- (90) Liu, C.-C.; Jiang, H.; Yao, Y. Low-Energy Effective Hamiltonian Involving Spin-Orbit Coupling in Silicene and Two-Dimensional Germanium and Tin. *Phys. Rev. B* **2011**, *84*, 195430.
- (91) Ezawa, M. Valley-Polarized Metals and Quantum Anomalous Hall Effect in Silicene. *Phys. Rev. Lett.* **2012**, *109*, 55502.

- (92) Pan, H.; Li, Z.; Liu, C.-C.; Zhu, G.; Qiao, Z.; Yao, Y. Valley-Polarized Quantum Anomalous Hall Effect in Silicene. *Phys. Rev. Lett.* **2014**, *112*, 106802.
- (93) Lalmi, B.; Oughaddou, H.; Enriquez, H.; Kara, A.; Vizzini, S.; Ealet, B.; Aufray, B. Epitaxial Growth of a Silicene Sheet. *Appl. Phys. Lett.* **2010**, *97*, 223109.
- (94) Feng, B.; Ding, Z.; Meng, S.; Yao, Y.; He, X.; Cheng, P.; Chen, L.; Wu, K. Evidence of Silicene in Honeycomb Structures of Silicon on Ag(111). *Nano Lett.* **2012**, *12*, 3507–3511.
- (95) Lin, C.-L.; Arafune, R.; Kawahara, K.; Tsukahara, N.; Minamitani, E.; Kim, Y.; Takagi, N.; Kawai, M. Structure of Silicene Grown on Ag(111). *Appl. Phys. Express* **2012**, *5*, 45802.
- (96) Jamgotchian, H.; Colignon, Y.; Hamzaoui, N.; Ealet, B.; Hoarau, J. Y.; Aufray, B.; Bibérian, J. P. Growth of Silicene Layers on Ag(111): Unexpected Effect of the Substrate Temperature. *J. Phys. Condens. Matter* **2012**, *24*, 172001.
- (97) Chen, L.; Liu, C.-C.; Feng, B.; He, X.; Cheng, P.; Ding, Z.; Meng, S.; Yao, Y.; Wu, K. Evidence for Dirac Fermions in a Honeycomb Lattice Based on Silicon. *Phys. Rev. Lett.* **2012**, *109*, 56804.
- (98) Meng, L.; Wang, Y.; Zhang, L.; Du, S.; Wu, R.; Li, L.; Zhang, Y.; Li, G.; Zhou, H.; Hofer, W. A.; Gao, H.-J. Buckled Silicene Formation on Ir(111). *Nano Lett.* **2013**, *13*, 685–690.
- (99) Fleurence, A.; Friedlein, R.; Ozaki, T.; Kawai, H.; Wang, Y.; Yamada-Takamura, Y. Experimental Evidence for Epitaxial Silicene on Diboride Thin Films. *Phys. Rev. Lett.* **2012**, *108*, 245501.
- (100) Chiappe, D.; Scalise, E.; Cinquanta, E.; Grazianetti, C.; van den Broek, B.; Fanciulli,

- M.; Houssa, M.; Molle, A. Two-Dimensional Si Nanosheets with Local Hexagonal Structure on a MoS₂ Surface. *Adv. Mater.* **2014**, *26*, 2096–2101.
- (101) Aizawa, T.; Suehara, S.; Otani, S. Silicene on Zirconium Carbide (111). *J. Phys. Chem. C* **2014**, *118*, 23049–23057.
- (102) Sadeddine, S.; Enriquez, H.; Bendounan, A.; Kumar Das, P.; Vobornik, I.; Kara, A.; Mayne, A. J.; Sirotti, F.; Dujardin, G.; Oughaddou, H. Compelling Experimental Evidence of a Dirac Cone in the Electronic Structure of a 2D Silicon Layer. *Sci. Rep.* **2017**, *7*, 44400.
- (103) Quhe, R.; Yuan, Y.; Zheng, J.; Wang, Y.; Ni, Z.; Shi, J.; Yu, D.; Yang, J.; Lu, J. Does the Dirac Cone Exist in Silicene on Metal Substrates? *Sci. Rep.* **2014**, *4*, 5476.
- (104) Satta, M.; Colonna, S.; Flammini, R.; Cricenti, A.; Ronci, F. Silicon Reactivity at the Ag(111) Surface. *Phys. Rev. Lett.* **2015**, *115*, 26102.
- (105) Han, N.; Liu, H.; Zhao, J. Novel Magnetic Monolayers of Transition Metal Silicide. *J. Supercond. Nov. Magn.* **2015**, *28*, 1755–1758.
- (106) Dzade, N. Y.; Obodo, K. O.; Adjokatse, S. K.; Ashu, A. C.; Amankwah, E.; Atiso, C. D.; Bello, A. A.; Igumbor, E.; Nzabarinda, S. B.; Obodo, J. T.; Ogbuu, A. O.; Femi, O. E.; Udeigwe, J. O.; Waghmare, U. V. Silicene and Transition Metal Based Materials: Prediction of a Two-Dimensional Piezomagnet. *J. Phys. Condens. Matter* **2010**, *22*, 375502.
- (107) Zhang, X.-L.; Liu, L.-F.; Liu, W.-M. Quantum Anomalous Hall Effect and Tunable Topological States in 3d Transition Metals Doped Silicene. *Sci. Rep.* **2013**, *3*, 2908.
- (108) Sahin, H.; Peeters, F. M. Adsorption of Alkali, Alkaline-Earth, and 3d Transition Metal Atoms on Silicene. *Phys. Rev. B* **2013**, *87*, 85423.

- (109) Bui, V. Q.; Pham, T.-T.; Nguyen, H.-V. S.; Le, H. M. Transition Metal (Fe and Cr) Adsorptions on Buckled and Planar Silicene Monolayers: A Density Functional Theory Investigation. *J. Phys. Chem. C* **2013**, *117*, 23364–23371.
- (110) Kaloni, T. P.; Singh, N.; Schwingenschlögl, U. Prediction of a Quantum Anomalous Hall State in Co-Decorated Silicene. *Phys. Rev. B* **2014**, *89*, 35409.
- (111) Lee, Y.; Yun, K.-H.; Cho, S. B.; Chung, Y.-C. Electronic Properties of Transition-Metal-Decorated Silicene. *ChemPhysChem* **2014**, *15*, 4095–4099.
- (112) Sun, X.; Wang, L.; Lin, H.; Hou, T.; Li, Y. Induce Magnetism into Silicene by Embedding Transition-Metal Atoms. *Appl. Phys. Lett.* **2015**, *106*, 222401.
- (113) Wu, Q.; Zhang, J.-J.; Hao, P.; Ji, Z.; Dong, S.; Ling, C.; Chen, Q.; Wang, J. Versatile Titanium Silicide Monolayers with Prominent Ferromagnetic, Catalytic, and Superconducting Properties: Theoretical Prediction. *J. Phys. Chem. Lett.* **2016**, *7*, 3723–3729.
- (114) Popis, M. D.; Popis, S. V; Oncel, N.; Hoffmann, M. R.; Çakır, D. Study of Iridium Silicide Monolayers Using Density Functional Theory. *J. Appl. Phys.* **2018**, *123*, 74301.
- (115) Roueff, E. Microphysics and Astrophysical Observations: The Molecular Perspective. *J. Phys. Conf. Ser.* **2005**, *4*, 1–9.
- (116) McGuire, B. A. 2018 Census of Interstellar, Circumstellar, Extragalactic, Protoplanetary Disk, and Exoplanetary Molecules. *Astrophys. J. Suppl. Ser.* **2018**, *239*, 17.
- (117) Matson, D. L.; Spilker, L. J.; Lebreton, J.-P. The Cassini/Huygens Mission to the Saturnian System. In *The Cassini-Huygens Mission: Overview, Objectives and*

Huygens Instrumentarium Volume 1; Russell, C. T., Ed.; Springer Netherlands: Dordrecht, 2003; pp 1–58.

- (118) NASA’s Jet Propulsion Laboratory - California Institute of Technology
<https://www.jpl.nasa.gov/missions/cassini-huygens> (accessed Sep 14, 2021).
- (119) NASA Science - Solar System Exploration
<https://solarsystem.nasa.gov/missions/cassini/mission/quick-facts/> (accessed Sep 14, 2021).
- (120) Petrie, S.; Bohme, D. K. Ions in Space. *Mass Spectrom. Rev.* **2007**, *26*, 258–280.
- (121) de Barros, A. L. F.; Bordalo, V.; Seperuelo Duarte, E.; F da Silveira, E.; Domaracka, A.; Rothard, H.; Boduch, P. Cosmic Ray Impact on Astrophysical Ices: Laboratory Studies on Heavy Ion Irradiation of Methane. *A&A* **2011**, *531*, A160.
- (122) Allodi, M. A.; Baragiola, R. A.; Baratta, G. A.; Barucci, M. A.; Blake, G. A.; Boduch, P.; Brucato, J. R.; Contreras, C.; Cuyille, S. H.; Fulvio, D.; Gudipati, M. S.; Ioppolo, S.; Kaňuchová, Z.; Lignell, A.; Linnartz, H.; Palumbo, M. E.; Raut, U.; Rothard, H.; Salama, F.; Savchenko, E. V.; Sciamma-O’Brien, E.; Strazzulla, G. Complementary and Emerging Techniques for Astrophysical Ices Processed in the Laboratory. *Space Sci. Rev.* **2013**, *180*, 101–175.
- (123) López, A.; Tercero, B.; Kisiel, Z.; Daly, A. M.; Bermúdez, C.; Calcutt, H.; Marcelino, N.; Viti, S.; Drouin, B. J.; Medvedev, I. R.; Neese, C. F.; Pszczółkowski, L.; Alonso, J. L.; Cernicharo, J. Laboratory Characterization and Astrophysical Detection of Vibrationally Excited States of Vinyl Cyanide in Orion-KL. *A&A* **2014**, *572*, A44.
- (124) Danger, G.; Fresneau, A.; Abou Mrad, N.; de Marcellus, P.; Orthous-Daunay, F.-R.;

- Duvernay, F.; Vuitton, V.; Le Sergeant d'Hendecourt, L.; Thissen, R.; Chiavassa, T. Insight into the Molecular Composition of Laboratory Organic Residues Produced from Interstellar/Pre-Cometary Ice Analogues Using Very High Resolution Mass Spectrometry. *Geochim. Cosmochim. Acta* **2016**, *189*, 184–196.
- (125) Wilson, S. Theoretical Studies of Interstellar Radicals and Ions. *Chem. Rev.* **1980**, *80*, 263–267.
- (126) Kang, D.; Hou, Y.; Zeng, Q.; Dai, J. Unified First-Principles Equations of State of Deuterium-Tritium Mixtures in the Global Inertial Confinement Fusion Region. *Matter Radiat. Extrem.* **2020**, *5*, 55401.
- (127) Weber, S.; Wu, Y.; Wang, J. Recent Progress in Atomic and Molecular Physics for Controlled Fusion and Astrophysics. *Matter Radiat. Extrem.* **2021**, *6*, 23002.
- (128) Wan, M.; Yuan, D.; Jin, C.; Wang, F.; Yang, Y.; Yu, Y.; Shao, J. Laser Cooling of the AlCl Molecule with a Three-Electronic-Level Theoretical Model. *J. Chem. Phys.* **2016**, *145*, 24309.
- (129) Owens, A.; Clark, V. H. J.; Mitrushchenkov, A.; Yurchenko, S. N.; Tennyson, J. Theoretical Rovibronic Spectroscopy of the Calcium Monohydroxide Radical (CaOH). *J. Chem. Phys.* **2021**, *154*, 234302.
- (130) Hoffmann, M. R. Canonical Van Vleck Quasidegenerate Perturbation Theory with Trigonometric Variables. *J. Phys. Chem.* **1996**, *100*, 6125–6130.
- (131) Hoffmann, M. R.; Helgaker, T. Use of Density Functional Theory Orbitals in the GVVPT2 Variant of Second-Order Multistate Multireference Perturbation Theory. *J. Phys. Chem. A* **2015**, *119*, 1548–1553.
- (132) Theis, D.; Khait, Y. G.; Hoffmann, M. R. GVVPT2 Energy Gradient Using a

- Lagrangian Formulation. *J. Chem. Phys.* **2011**, *135*, 44117.
- (133) Khait, Y. G.; Song, J.; Hoffmann, M. R. Explication and Revision of Generalized Van Vleck Perturbation Theory for Molecular Electronic Structure. *J. Chem. Phys.* **2002**, *117*, 4133–4145.
- (134) Khait, Y. G.; Song, J.; Hoffmann, M. R. Macroconfigurations in Molecular Electronic Structure Theory. *Int. J. Quantum Chem.* **2004**, *99*, 210–220.
- (135) Hoy, M. B. Alexa, Siri, Cortana, and More: An Introduction to Voice Assistants. *Med. Ref. Serv. Q.* **2018**, *37*, 81–88.
- (136) Darabant, A. S.; Borza, D.; Danescu, R. Recognizing Human Races through Machine Learning—A Multi-Network, Multi-Features Study. *Mathematics* **2021**, *9*, 195.
- (137) Sharma, A.; Meena, U. Undefeatable System Using Machine Learning. In *Intelligent Computing and Applications*; Dash, S. S., Das, S., Panigrahi, B. K., Eds.; Springer Singapore: Singapore, 2021; pp 759–767.
- (138) García Cuenca, L.; Sanchez-Soriano, J.; Puertas, E.; Fernandez Andrés, J.; Aliane, N. Machine Learning Techniques for Undertaking Roundabouts in Autonomous Driving. *Sensors* **2019**, *19*, 2386.
- (139) Jordan, M. I.; Mitchell, T. M. Machine Learning: Trends, Perspectives, and Prospects. *Science (80-.)*. **2015**, *349*, 255–260.
- (140) Bzdok, D.; Krzywinski, M.; Altman, N. Machine Learning: Supervised Methods. *Nat. Methods* **2018**, *15*, 5–6.
- (141) Ceriotti, M. Unsupervised Machine Learning in Atomistic Simulations, between Predictions and Understanding. *J. Chem. Phys.* **2019**, *150*, 150901.

- (142) Sutton, R. S. Introduction: The Challenge of Reinforcement Learning. In *Reinforcement Learning*; Sutton, R. S., Ed.; Springer US: Boston, MA, 1992; pp 1–3.
- (143) Liu, R.; Nageotte, F.; Zanne, P.; de Mathelin, M.; Dresch-Langley, B. Deep Reinforcement Learning for the Control of Robotic Manipulation: A Focussed Mini-Review. *Robotics* **2021**, *10*, 22.
- (144) Hady, M. F. A.; Schwenker, F. Semi-Supervised Learning. In *Handbook on Neural Information Processing*; Bianchini, M., Maggini, M., Jain, L. C., Eds.; Springer Berlin Heidelberg: Berlin, Heidelberg, 2013; pp 215–239.
- (145) Daniels, M. W.; Dvorkin, D.; Powers, R. K.; Kechris, K. Semi-Supervised Learning Using Hierarchical Mixture Models: Gene Essentiality Case Study. *Math. Comput. Appl.* **2021**, *26*, 40.
- (146) Yu, H.; Sun, C.; Yang, W.; Yang, X.; Zuo, X. AL-ELM: One Uncertainty-Based Active Learning Algorithm Using Extreme Learning Machine. *Neurocomputing* **2015**, *166*, 140–150.
- (147) Gubaev, K.; Podryabinkin, E. V.; Shapeev, A. V. Machine Learning of Molecular Properties: Locality and Active Learning. *J. Chem. Phys.* **2018**, *148*, 241727.
- (148) Behler, J. Perspective: Machine Learning Potentials for Atomistic Simulations. *J. Chem. Phys.* **2016**, *145*, 170901.
- (149) von Lilienfeld, O. A.; Burke, K. Retrospective on a Decade of Machine Learning for Chemical Discovery. *Nat. Commun.* **2020**, *11*, 4895.
- (150) Westermayr, J.; Marquetand, P. Machine Learning for Electronically Excited States of Molecules. *Chem. Rev.* **2021**, *121*, 9873–9926.

- (151) Schleder, G. R.; Padilha, A. C. M.; Acosta, C. M.; Costa, M.; Fazzio, A. From DFT to Machine Learning: Recent Approaches to Materials Science—a Review. *J. Phys. Mater.* **2019**, *2*, 32001.
- (152) Chandrasekaran, A.; Kamal, D.; Batra, R.; Kim, C.; Chen, L.; Ramprasad, R. Solving the Electronic Structure Problem with Machine Learning. *npj Comput. Mater.* **2019**, *5*, 22.
- (153) Bogojeski, M.; Vogt-Maranto, L.; Tuckerman, M. E.; Müller, K.-R.; Burke, K. Quantum Chemical Accuracy from Density Functional Approximations via Machine Learning. *Nat. Commun.* **2020**, *11*, 5223.
- (154) Jeong, W.; Stoneburner, S. J.; King, D.; Li, R.; Walker, A.; Lindh, R.; Gagliardi, L. Automation of Active Space Selection for Multireference Methods via Machine Learning on Chemical Bond Dissociation. *J. Chem. Theory Comput.* **2020**, *16*, 2389–2399.
- (155) Hermann, J.; Schätzle, Z.; Noé, F. Deep-Neural-Network Solution of the Electronic Schrödinger Equation. *Nat. Chem.* **2020**, *12*, 891–897.
- (156) Paszke, A.; Gross, S.; Chintala, S.; Chanan, G.; Yang, E.; DeVito, Z.; Lin, Z.; Desmaison, A.; Antiga, L.; Lerer, A. Automatic Differentiation in PyTorch. *NIPS-W* **2017**.
- (157) Szabo, A.; Ostlund, N. S. *Modern Quantum Chemistry: Introduction to Advanced Electronic Structure Theory*; Dover: Mineola, New York, 1996.
- (158) Shikano, Y.; Watanabe, H. C.; Nakanishi, K. M.; Ohnishi, Y. Post-Hartree–Fock Method in Quantum Chemistry for Quantum Computer. *Eur. Phys. J. Spec. Top.* **2021**, *230*, 1037–1051.

- (159) Born, M.; Oppenheimer, R. Zur Quantentheorie Der Molekeln. *Ann. Phys.* **1927**, *389*, 457–484.
- (160) Pauli, W. Über Den Zusammenhang Des Abschlusses Der Elektronengruppen Im Atom Mit Der Komplexstruktur Der Spektren. *Z. Phys.* **1925**, *31*, 765–783.
- (161) Lieb, E. H. Variational Principle for Many-Fermion Systems. *Phys. Rev. Lett.* **1981**, *46*, 457–459.
- (162) Löwdin, P.-O. Quantum Theory of Many-Particle Systems. II. Study of the Ordinary Hartree-Fock Approximation. *Phys. Rev.* **1955**, *97*, 1490–1508.
- (163) Roothaan, C. C. J. New Developments in Molecular Orbital Theory. *Rev. Mod. Phys.* **1951**, *23*, 69–89.
- (164) Hall, G. G.; Lennard-Jones, J. E. The Molecular Orbital Theory of Chemical Valency VIII. A Method of Calculating Ionization Potentials. *Proc. Math. Phys. Eng. Sci.* **1951**, *205*, 541–552.
- (165) Thomas, L. H. The Calculation of Atomic Fields. *Math. Proc. Camb. Philos. Soc.* **1927**, *23*, 542–548.
- (166) Fermi, E. Eine Statistische Methode Zur Bestimmung Einiger Eigenschaften Des Atoms Und Ihre Anwendung Auf Die Theorie Des Periodischen Systems Der Elemente. *Z. Phys.* **1928**, *48*, 73–79.
- (167) Burke, K. Perspective on Density Functional Theory. *J. Chem. Phys.* **2012**, *136*, 150901.
- (168) Sholl, D. S.; Steckel, J. A. *Density Functional Theory : A Practical Introduction*; Wiley: Hoboken, NJ, 2009.
- (169) Wang, Y. A.; Govind, N.; Carter, E. A. Orbital-Free Kinetic-Energy Density

- Functionals with a Density-Dependent Kernel. *Phys. Rev. B* **1999**, *60*, 16350–16358.
- (170) Xia, J.; Huang, C.; Shin, I.; Carter, E. A. Can Orbital-Free Density Functional Theory Simulate Molecules? *J. Chem. Phys.* **2012**, *136*, 84102.
- (171) Levine, I. N. *Quantum Chemistry*; Prentice Hall: Upper Saddle River, N.J., 2000.
- (172) Kryachko, E. S.; Ludeña, E. V. Density Functional Theory: Foundations Reviewed. *Phys. Rep.* **2014**, *544*, 123–239.
- (173) Woods, N. D.; Payne, M. C.; Hasnip, P. J. Computing the Self-Consistent Field in Kohn–Sham Density Functional Theory. *J. Phys. Condens. Matter* **2019**, *31*, 453001.
- (174) Vosko, S. H.; Wilk, L.; Nusair, M. Accurate Spin-Dependent Electron Liquid Correlation Energies for Local Spin Density Calculations: A Critical Analysis. *Can. J. Phys.* **1980**, *58*, 1200–1211.
- (175) Vosko, S. H.; Wilk, L. Influence of an Improved Local-Spin-Density Correlation-Energy Functional on the Cohesive Energy of Alkali Metals. *Phys. Rev. B* **1980**, *22*, 3812–3815.
- (176) Perdew, J. P.; Zunger, A. Self-Interaction Correction to Density-Functional Approximations for Many-Electron Systems. *Phys. Rev. B* **1981**, *23*, 5048–5079.
- (177) Perdew, J. P.; Wang, Y. Accurate and Simple Analytic Representation of the Electron-Gas Correlation Energy. *Phys. Rev. B* **1992**, *45*, 13244–13249.
- (178) Becke, A. D. Density-Functional Exchange-Energy Approximation with Correct Asymptotic Behavior. *Phys. Rev. A* **1988**, *38*, 3098–3100.
- (179) Perdew, J. P.; Chevary, J. A.; Vosko, S. H.; Jackson, K. A.; Pederson, M. R.; Singh, D. J.; Fiolhais, C. Atoms, Molecules, Solids, and Surfaces: Applications of the

- Generalized Gradient Approximation for Exchange and Correlation. *Phys. Rev. B* **1992**, *46*, 6671–6687.
- (180) Perdew, J. P.; Burke, K.; Ernzerhof, M. Generalized Gradient Approximation Made Simple. *Phys. Rev. Lett.* **1996**, *77*, 3865–3868.
- (181) Perdew, J. P. Density-Functional Approximation for the Correlation Energy of the Inhomogeneous Electron Gas. *Phys. Rev. B* **1986**, *33*, 8822–8824.
- (182) Lee, C.; Yang, W.; Parr, R. G. Development of the Colle-Salvetti Correlation-Energy Formula into a Functional of the Electron Density. *Phys. Rev. B* **1988**, *37*, 785–789.
- (183) Becke, A. D. A New Mixing of Hartree–Fock and Local Density-functional Theories. *J. Chem. Phys.* **1993**, *98*, 1372–1377.
- (184) Perdew, J. P.; Schmidt, K. Jacob’s Ladder of Density Functional Approximations for the Exchange-Correlation Energy. *AIP Conf. Proc.* **2001**, *577*, 1–20.
- (185) Makov, G.; Payne, M. C. Periodic Boundary Conditions in Ab Initio Calculations. *Phys. Rev. B* **1995**, *51*, 4014–4022.
- (186) Bloch, F. Über Die Quantenmechanik Der Elektronen in Kristallgittern. *Z. Phys.* **1929**, *52*, 555–600.
- (187) Kittel, C. *Introduction to Solid State Physics*, 7th ed.; Wiley: New York, NY, 1996.
- (188) Bylaska, E. J. Chapter Five - Plane-Wave DFT Methods for Chemistry. In *Annual Reports in Computational Chemistry*; Dixon, D. A., Ed.; Elsevier: Amsterdam, Netherlands, 2017; Vol. 13, pp 185–228.
- (189) Blöchl, P. E.; Först, C. J.; Schimpl, J. Projector Augmented Wave Method: Ab Initio Molecular Dynamics with Full Wave Functions. *Bull. Mater. Sci.* **2003**, *26*, 33–41.

- (190) Herring, C. A New Method for Calculating Wave Functions in Crystals. *Phys. Rev.* **1940**, *57*, 1169–1177.
- (191) Antončík, E. Approximate Formulation of the Orthogonalized Plane-Wave Method. *J. Phys. Chem. Solids* **1959**, *10*, 314–320.
- (192) Phillips, J. C.; Kleinman, L. New Method for Calculating Wave Functions in Crystals and Molecules. *Phys. Rev.* **1959**, *116*, 287–294.
- (193) Phillips, J. C. Energy-Band Interpolation Scheme Based on a Pseudopotential. *Phys. Rev.* **1958**, *112*, 685–695.
- (194) Austin, B. J.; Heine, V.; Sham, L. J. General Theory of Pseudopotentials. *Phys. Rev.* **1962**, *127*, 276–282.
- (195) Bachelet, G. B.; Hamann, D. R.; Schlüter, M. Pseudopotentials That Work: From H to Pu. *Phys. Rev. B* **1982**, *26*, 4199–4228.
- (196) Yin, M. T.; Cohen, M. L. Theory of Ab Initio Pseudopotential Calculations. *Phys. Rev. B* **1982**, *25*, 7403–7412.
- (197) Hamann, D. R. Generalized Norm-Conserving Pseudopotentials. *Phys. Rev. B* **1989**, *40*, 2980–2987.
- (198) Troullier, N.; Martins, J. L. Efficient Pseudopotentials for Plane-Wave Calculations. *Phys. Rev. B* **1991**, *43*, 1993–2006.
- (199) Slater, J. C. Wave Functions in a Periodic Potential. *Phys. Rev.* **1937**, *51*, 846–851.
- (200) Korringa, J. On the Calculation of the Energy of a Bloch Wave in a Metal. *Physica* **1947**, *13*, 392–400.
- (201) Kohn, W.; Rostoker, N. Solution of the Schrödinger Equation in Periodic Lattices with an Application to Metallic Lithium. *Phys. Rev.* **1954**, *94*, 1111–1120.

- (202) Blöchl, P. E. Projector Augmented-Wave Method. *Phys. Rev. B* **1994**, *50*, 17953–17979.
- (203) Kresse, G.; Joubert, D. From Ultrasoft Pseudopotentials to the Projector Augmented-Wave Method. *Phys. Rev. B* **1999**, *59*, 1758–1775.
- (204) Holzwarth, N. A. W.; Matthews, G. E.; Dunning, R. B.; Tackett, A. R.; Zeng, Y. Comparison of the Projector Augmented-Wave, Pseudopotential, and Linearized Augmented-Plane-Wave Formalisms for Density-Functional Calculations of Solids. *Phys. Rev. B* **1997**, *55*, 2005–2017.
- (205) Valiev, M.; Weare, J. H. The Projector-Augmented Plane Wave Method Applied to Molecular Bonding. *J. Phys. Chem. A* **1999**, *103*, 10588–10601.
- (206) Runge, E.; Gross, E. K. U. Density-Functional Theory for Time-Dependent Systems. *Phys. Rev. Lett.* **1984**, *52*, 997–1000.
- (207) Petersilka, M.; Gossmann, U. J.; Gross, E. K. U. Excitation Energies from Time-Dependent Density-Functional Theory. *Phys. Rev. Lett.* **1996**, *76*, 1212–1215.
- (208) van Leeuwen, R. Causality and Symmetry in Time-Dependent Density-Functional Theory. *Phys. Rev. Lett.* **1998**, *80*, 1280–1283.
- (209) van Leeuwen, R. Mapping from Densities to Potentials in Time-Dependent Density-Functional Theory. *Phys. Rev. Lett.* **1999**, *82*, 3863–3866.
- (210) Burke, K.; Werschnik, J.; Gross, E. K. U. Time-Dependent Density Functional Theory: Past, Present, and Future. *J. Chem. Phys.* **2005**, *123*, 62206.
- (211) Silva-Junior, M. R.; Schreiber, M.; Sauer, S. P. A.; Thiel, W. Benchmarks for Electronically Excited States: Time-Dependent Density Functional Theory and Density Functional Theory Based Multireference Configuration Interaction. *J.*

- Chem. Phys.* **2008**, *129*, 104103.
- (212) Laurent, A. D.; Jacquemin, D. TD-DFT Benchmarks: A Review. *Int. J. Quantum Chem.* **2013**, *113*, 2019–2039.
- (213) Adamo, C.; Jacquemin, D. The Calculations of Excited-State Properties with Time-Dependent Density Functional Theory. *Chem. Soc. Rev.* **2013**, *42*, 845–856.
- (214) Rayleigh, J. W. S. B. *The Theory of Sound*; Macmillan and Co.: London, 1877.
- (215) Sakurai, J. J.; Napolitano, J. *Modern Quantum Mechanics*; Cambridge University Press: Cambridge, 2020.
- (216) Cremer, D. Møller–Plesset Perturbation Theory: From Small Molecule Methods to Methods for Thousands of Atoms. *Wiley Interdiscip. Rev. Comput. Mol. Sci.* **2011**, *1*, 509–530.
- (217) Head-Gordon, M.; Pople, J. A.; Frisch, M. J. MP2 Energy Evaluation by Direct Methods. *Chem. Phys. Lett.* **1988**, *153*, 503–506.
- (218) Grimme, S. Improved Second-Order Møller–Plesset Perturbation Theory by Separate Scaling of Parallel- and Antiparallel-Spin Pair Correlation Energies. *J. Chem. Phys.* **2003**, *118*, 9095–9102.
- (219) Jensen, H. J. A.; Jørgensen, P.; Ågren, H.; Olsen, J. Second-order Møller–Plesset Perturbation Theory as a Configuration and Orbital Generator in Multiconfiguration Self-consistent Field Calculations. *J. Chem. Phys.* **1988**, *88*, 3834–3839.
- (220) Roos, B. O.; Taylor, P. R.; Sigbahn, P. E. M. A Complete Active Space SCF Method (CASSCF) Using a Density Matrix Formulated Super-CI Approach. *Chem. Phys.* **1980**, *48*, 157–173.
- (221) Olsen, J.; Roos, B. O.; Jørgensen, P.; Jensen, H. J. A. Determinant Based

- Configuration Interaction Algorithms for Complete and Restricted Configuration Interaction Spaces. *J. Chem. Phys.* **1988**, *89*, 2185–2192.
- (222) Townsend, J.; Kirkland, J. K.; Vogiatzis, K. D. Chapter 3 - Post-Hartree-Fock Methods: Configuration Interaction, Many-Body Perturbation Theory, Coupled-Cluster Theory. In *Developments in Physical & Theoretical Chemistry*; Blinder, S. M., House, J. E., Eds.; Elsevier: Amsterdam, Netherlands, 2019; pp 63–117.
- (223) Gérard, H.; Davidson, E. R.; Eisenstein, O. Comparison of α CH and CF Activation in Alkyl Transition Metal Complexes: A DFT and CASSCF Study. *Mol. Phys.* **2002**, *100*, 533–540.
- (224) Chen, M.; Dixon, D. A. Low-Lying Electronic States of Iron Clusters with $n = 2-8$ Predicted at the DFT, CASSCF, and CCSD(T) Levels. *J. Phys. Chem. A* **2013**, *117*, 3676–3688.
- (225) Blaziak, K.; Tzeli, D.; Xantheas, S. S.; Uggerud, E. The Activation of Carbon Dioxide by First Row Transition Metals (Sc–Zn). *Phys. Chem. Chem. Phys.* **2018**, *20*, 25495–25505.
- (226) Sobolewski, A. L.; Domcke, W.; Dedonder-Lardeux, C.; Jouvet, C. Excited-State Hydrogen Detachment and Hydrogen Transfer Driven by Repulsive $1\pi\sigma^*$ States: A New Paradigm for Nonradiative Decay in Aromatic Biomolecules. *Phys. Chem. Chem. Phys.* **2002**, *4*, 1093–1100.
- (227) Francés-Monerris, A.; Segarra-Martí, J.; Merchán, M.; Roca-Sanjuán, D. Complete-Active-Space Second-Order Perturbation Theory (CASPT2//CASSCF) Study of the Dissociative Electron Attachment in Canonical DNA Nucleobases Caused by Low-Energy Electrons (0-3 eV). *J. Chem. Phys.* **2015**, *143*, 215101.

- (228) Olsen, J. The CASSCF Method: A Perspective and Commentary. *Int. J. Quantum Chem.* **2011**, *111*, 3267–3272.
- (229) Friesner, R. A. Ab Initio Quantum Chemistry: Methodology and Applications. *Proc. Natl. Acad. Sci. U.S.A.* **2005**, *102*, 6648–6653.
- (230) Shavitt, I.; Redmon, L. T. Quasidegenerate Perturbation Theories. A Canonical van Vleck Formalism and Its Relationship to Other Approaches. *J. Chem. Phys.* **1980**, *73*, 5711–5717.
- (231) Kuhler, K.; Hoffmann, M. R. A Nondiagonal Quasidegenerate Fourth-Order Perturbation Theory. *J. Math. Chem.* **1996**, *20*, 351–364.
- (232) Autschbach, J. Perspective: Relativistic Effects. *J. Chem. Phys.* **2012**, *136*, 150902.
- (233) Dyall, K. G. Interfacing Relativistic and Nonrelativistic Methods. I. Normalized Elimination of the Small Component in the Modified Dirac Equation. *J. Chem. Phys.* **1997**, *106*, 9618–9626.
- (234) Liu, W. Ideas of Relativistic Quantum Chemistry. *Mol. Phys.* **2010**, *108*, 1679–1706.
- (235) Liu, W.; Peng, D. Exact Two-Component Hamiltonians Revisited. *J. Chem. Phys.* **2009**, *131*, 31104.
- (236) Cheng, L.; Gauss, J. Analytic Energy Gradients for the Spin-Free Exact Two-Component Theory Using an Exact Block Diagonalization for the One-Electron Dirac Hamiltonian. *J. Chem. Phys.* **2011**, *135*, 84114.
- (237) Li, Z.; Suo, B.; Zhang, Y.; Xiao, Y.; Liu, W. Combining Spin-Adapted Open-Shell TD-DFT with Spin–Orbit Coupling. *Mol. Phys.* **2013**, *111*, 3741–3755.
- (238) Li, Z.; Xiao, Y.; Liu, W. On the Spin Separation of Algebraic Two-Component

- Relativistic Hamiltonians: Molecular Properties. *J. Chem. Phys.* **2014**, *141*, 54111.
- (239) Li, Z.; Xiao, Y.; Liu, W. On the Spin Separation of Algebraic Two-Component Relativistic Hamiltonians. *J. Chem. Phys.* **2012**, *137*, 154114.
- (240) Autschbach, J.; Peng, D.; Reiher, M. Two-Component Relativistic Calculations of Electric-Field Gradients Using Exact Decoupling Methods: Spin–Orbit and Picture-Change Effects. *J. Chem. Theory Comput.* **2012**, *8*, 4239–4248.
- (241) Cheng, L.; Stopkowicz, S.; Gauss, J. Analytic Energy Derivatives in Relativistic Quantum Chemistry. *Int. J. Quantum Chem.* **2014**, *114*, 1108–1127.
- (242) Saue, T. Relativistic Hamiltonians for Chemistry: A Primer. *ChemPhysChem* **2011**, *12*, 3077–3094.
- (243) Cheng, L.; Gauss, J.; Stanton, J. F. Treatment of Scalar-Relativistic Effects on Nuclear Magnetic Shieldings Using a Spin-Free Exact-Two-Component Approach. *J. Chem. Phys.* **2013**, *139*, 54105.
- (244) Cheng, L.; Gauss, J. Perturbative Treatment of Spin-Orbit Coupling within Spin-Free Exact Two-Component Theory. *J. Chem. Phys.* **2014**, *141*, 164107.
- (245) Peng, D.; Middendorf, N.; Weigend, F.; Reiher, M. An Efficient Implementation of Two-Component Relativistic Exact-Decoupling Methods for Large Molecules. *J. Chem. Phys.* **2013**, *138*, 184105.
- (246) Iliáš, M.; Jensen, H. J. A.; Kellö, V.; Roos, B. O.; Urban, M. Theoretical Study of PbO and the PbO Anion. *Chem. Phys. Lett.* **2005**, *408*, 210–215.
- (247) Chen, T.; Guestrin, C. XGBoost: A Scalable Tree Boosting System. In *Proceedings of the 22nd ACM SIGKDD International Conference on Knowledge Discovery and Data Mining*; KDD '16; Association for Computing Machinery: New York, NY,

USA, 2016; pp 785–794.

- (248) Golub, P.; Antalik, A.; Veis, L.; Brabec, J. Automatic Selection of Active Spaces for Strongly Correlated Systems Using Machine Learning Algorithms. *arXiv Prepr. arXiv2011.14715* **2020**.
- (249) White, S. R. Density Matrix Formulation for Quantum Renormalization Groups. *Phys. Rev. Lett.* **1992**, *69*, 2863–2866.
- (250) White, S. R. Density-Matrix Algorithms for Quantum Renormalization Groups. *Phys. Rev. B* **1993**, *48*, 10345–10356.
- (251) Schollwöck, U. The Density-Matrix Renormalization Group. *Rev. Mod. Phys.* **2005**, *77*, 259–315.
- (252) Dávila, M. E.; Xian, L.; Cahangirov, S.; Rubio, A.; Lay, G. Le. Germanene: A Novel Two-Dimensional Germanium Allotrope Akin to Graphene and Silicene. *New J. Phys.* **2014**, *16*, 95002.
- (253) Acun, A.; Zhang, L.; Bampoulis, P.; Farmanbar, M.; van Houselt, A.; Rudenko, A. N.; Lingenfelder, M.; Brocks, G.; Poelsema, B.; Katsnelson, M. I.; Zandvliet, H. J. W. Germanene: The Germanium Analogue of Graphene. *J. Phys. Condens. Matter* **2015**, *27*, 443002.
- (254) Cahangirov, S.; Topsakal, M.; Aktürk, E.; Şahin, H.; Ciraci, S. Two- and One-Dimensional Honeycomb Structures of Silicon and Germanium. *Phys. Rev. Lett.* **2009**, *102*, 236804.
- (255) Çakır, D.; Sahin, H.; Peeters, F. M. Tuning of the Electronic and Optical Properties of Single-Layer Black Phosphorus by Strain. *Phys. Rev. B* **2014**, *90*, 205421.
- (256) Çakır, D.; Sevik, C.; Peeters, F. M. Significant Effect of Stacking on the Electronic

- and Optical Properties of Few-Layer Black Phosphorus. *Phys. Rev. B* **2015**, *92*, 165406.
- (257) Britnell, L.; Ribeiro, R. M.; Eckmann, A.; Jalil, R.; Belle, B. D.; Mishchenko, A.; Kim, Y.-J.; Gorbachev, R. V.; Georgiou, T.; Morozov, S. V.; Grigorenko, A. N.; Geim, A. K.; Casiraghi, C.; Neto, A. H. C.; Novoselov, K. S. Strong Light-Matter Interactions in Heterostructures of Atomically Thin Films. *Science (80-.)*. **2013**, *340*, 1311–1314.
- (258) Lee, C.; Wei, X.; Kysar, J. W.; Hone, J. Measurement of the Elastic Properties and Intrinsic Strength of Monolayer Graphene. *Science (80-.)*. **2008**, *321*, 385–388.
- (259) Bertolazzi, S.; Brivio, J.; Kis, A. Stretching and Breaking of Ultrathin MoS₂. *ACS Nano* **2011**, *5*, 9703–9709.
- (260) Baroni, S.; de Gironcoli, S.; Dal Corso, A.; Giannozzi, P. Phonons and Related Crystal Properties from Density-Functional Perturbation Theory. *Rev. Mod. Phys.* **2001**, *73*, 515–562.
- (261) Togo, A.; Tanaka, I. First Principles Phonon Calculations in Materials Science. *Scr. Mater.* **2015**, *108*, 1–5.
- (262) Paier, J.; Marsman, M.; Hummer, K.; Kresse, G.; Gerber, I. C.; Ángyán, J. G. Screened Hybrid Density Functionals Applied to Solids. *J. Chem. Phys.* **2006**, *124*, 154709.
- (263) Çakır, D.; Peeters, F. M.; Sevik, C. Mechanical and Thermal Properties of H-MX₂ (M = Cr, Mo, W; X = O, S, Se, Te) Monolayers: A Comparative Study. *Appl. Phys. Lett.* **2014**, *104*, 203110.
- (264) Yu, L.; Ruzsinszky, A.; Perdew, J. P. Bending Two-Dimensional Materials To

- Control Charge Localization and Fermi-Level Shift. *Nano Lett.* **2016**, *16*, 2444–2449.
- (265) Booth, T. J.; Blake, P.; Nair, R. R.; Jiang, D.; Hill, E. W.; Bangert, U.; Bleloch, A.; Gass, M.; Novoselov, K. S.; Katsnelson, M. I.; Geim, A. K. Macroscopic Graphene Membranes and Their Extraordinary Stiffness. *Nano Lett.* **2008**, *8*, 2442–2446.
- (266) Tang, W.; Sanville, E.; Henkelman, G. A Grid-Based Bader Analysis Algorithm without Lattice Bias. *J. Phys. Condens. Matter* **2009**, *21*, 84204.
- (267) Sanville, E.; Kenny, S. D.; Smith, R.; Henkelman, G. Improved Grid-Based Algorithm for Bader Charge Allocation. *J. Comput. Chem.* **2007**, *28*, 899–908.
- (268) Henkelman, G.; Arnaldsson, A.; Jónsson, H. A Fast and Robust Algorithm for Bader Decomposition of Charge Density. *Comput. Mater. Sci.* **2006**, *36*, 354–360.
- (269) Yu, M.; Trinkle, D. R. Accurate and Efficient Algorithm for Bader Charge Integration. *J. Chem. Phys.* **2011**, *134*, 64111.
- (270) Fatima; Can Oguz, I.; Çakır, D.; Hossain, S.; Mohottige, R.; Gulseren, O.; Oncel, N. On the Structural and Electronic Properties of Ir-Silicide Nanowires on Si(001) Surface. *J. Appl. Phys.* **2016**, *120*, 95303.
- (271) Sun, Y.; Zhuo, Z.; Wu, X.; Yang, J. Room-Temperature Ferromagnetism in Two-Dimensional Fe₂Si Nanosheet with Enhanced Spin-Polarization Ratio. *Nano Lett.* **2017**, *17*, 2771–2777.
- (272) Yang, L.-M.; Bačić, V.; Popov, I. A.; Boldyrev, A. I.; Heine, T.; Frauenheim, T.; Ganz, E. Two-Dimensional Cu₂Si Monolayer with Planar Hexacoordinate Copper and Silicon Bonding. *J. Am. Chem. Soc.* **2015**, *137*, 2757–2762.
- (273) Yang, L.-M.; Popov, I. A.; Frauenheim, T.; Boldyrev, A. I.; Heine, T.; Bacic, V.;

- Ganz, E. Revealing Unusual Chemical Bonding in Planar Hyper-Coordinate Ni₂Ge and Quasi-Planar Ni₂Si Two-Dimensional Crystals. *Phys. Chem. Chem. Phys.* **2015**, *17*, 26043–26048.
- (274) Liu, G.; Lei, X. L.; Wu, M. S.; Xu, B.; Ouyang, C. Y. Is Silicene Stable in O₂? — First-Principles Study of O₂ Dissociation and O₂-Dissociation-Induced Oxygen Atoms Adsorption on Free-Standing Silicene. *EPL* **2014**, *106*, 47001.
- (275) McCurdy, H. E. *Faster, Better, Cheaper: Low-Cost Innovation in the U.S. Space Program*; Johns Hopkins University Press: Baltimore, 2001.
- (276) Tennyson, J.; Yurchenko, S. N. ExoMol: Molecular Line Lists for Exoplanet and Other Atmospheres. *Mon. Not. R. Astron. Soc.* **2012**, *425*, 21–33.
- (277) Bernath, P. F. Molecular Astronomy of Cool Stars and Sub-Stellar Objects. *Int. Rev. Phys. Chem.* **2009**, *28*, 681–709.
- (278) Tennyson, J.; Yurchenko, S. N. Laboratory Spectra of Hot Molecules: Data Needs for Hot Super-Earth Exoplanets. *Mol. Astrophys.* **2017**, *8*, 1–18.
- (279) Allard, F. The BT-Settl Model Atmospheres for Stars, Brown Dwarfs and Planets. *Proc. Int. Astron. Union* **2013**, *8*, 271–272.
- (280) Rajpurohit, A. S.; Reylé, C.; Allard, F.; Homeier, D.; Schultheis, M.; Bessell, M. S.; Robin, A. C. The Effective Temperature Scale of M Dwarfs. *Astron. Astrophys.* **2013**, *556*, A15.
- (281) Wang, Y.; Owens, A.; Tennyson, J.; Yurchenko, S. N. MARVEL Analysis of the Measured High-Resolution Rovibronic Spectra of the Calcium Monohydroxide Radical (CaOH). *Astrophys. J. Suppl. Ser.* **2020**, *248*, 9.
- (282) Bauschlicher, C. W.; Partridge, H. On the Dissociation Energy of CaOH and LiOH.

Chem. Phys. Lett. **1984**, *106*, 65–68.

- (283) Bauschlicher, C. W.; Langhoff, S. R.; Partridge, H. Ab Initio Study of the Alkali and Alkaline-earth Monohydroxides. *J. Chem. Phys.* **1986**, *84*, 901–909.
- (284) Bauschlicher, C. W.; Langhoff, S. R.; Steimle, T. C.; Shirley, J. E. The Permanent Electric Dipole Moment of CaOH. *J. Chem. Phys.* **1990**, *93*, 4179–4186.
- (285) Ortiz, J. V. Ground and Excited States of CaCH₃, CaNH₂, CaOH, and CaF through Electron Propagator Calculations. *J. Chem. Phys.* **1990**, *92*, 6728–6731.
- (286) Kong, J.; Boyd, R. J. The ²Σ⁺ States of HBeO, HMgO, and HCaO. *J. Chem. Phys.* **1996**, *104*, 4055–4060.
- (287) Koput, J.; Peterson, K. A. Ab Initio Potential Energy Surface and Vibrational–Rotational Energy Levels of X²Σ⁺ CaOH. *J. Phys. Chem. A* **2002**, *106*, 9595–9599.
- (288) Theodorakopoulos, G.; Petsalakis, I. D.; Liebermann, H.-P.; Buenker, R. J.; Koput, J. Ab Initio Calculations on Electronic States of CaOH. *J. Chem. Phys.* **2002**, *117*, 4810–4819.
- (289) Taylor, C. M.; Chaudhuri, R. K.; Freed, K. F. Electronic Structure of the Calcium Monohydroxide Radical. *J. Chem. Phys.* **2005**, *122*, 44317.
- (290) Kozyryev, I.; Steimle, T. C.; Yu, P.; Nguyen, D.-T.; Doyle, J. M. Determination of CaOH and CaOCH₃ Vibrational Branching Ratios for Direct Laser Cooling and Trapping. *New J. Phys.* **2019**, *21*, 52002.
- (291) Augustovičová, L. D.; Bohn, J. L. Ultracold Collisions of Polyatomic Molecules: CaOH. *New J. Phys.* **2019**, *21*, 103022.
- (292) Baum, L.; Vilas, N. B.; Hallas, C.; Augendraun, B. L.; Raval, S.; Mitra, D.; Doyle,

- J. M. 1D Magneto-Optical Trap of Polyatomic Molecules. *Phys. Rev. Lett.* **2020**, *124*, 133201.
- (293) Baum, L.; Vilas, N. B.; Hallas, C.; Augendraun, B. L.; Raval, S.; Mitra, D.; Doyle, J. M. Establishing a Nearly Closed Cycling Transition in a Polyatomic Molecule. *Phys. Rev. A* **2021**, *103*, 43111.
- (294) Kozyryev, I.; Baum, L.; Matsuda, K.; Olson, P.; Hemmerling, B.; Doyle, J. M. Collisional Relaxation of Vibrational States of SrOH with He at 2 K. *New J. Phys.* **2015**, *17*, 45003.
- (295) Kozyryev, I.; Baum, L.; Matsuda, K.; Hemmerling, B.; Doyle, J. Radiation Pressure Force from Optical Cycling on a Polyatomic Molecule. *J. Phys. B At. Mol. Opt. Phys.* **2016**, *49*, 134002.
- (296) Kozyryev, I.; Baum, L.; Matsuda, K.; Augendraun, B. L.; Anderegg, L.; Sedlack, A. P.; Doyle, J. M. Sisyphus Laser Cooling of a Polyatomic Molecule. *Phys. Rev. Lett.* **2017**, *118*, 173201.
- (297) Morita, M.; Kłos, J.; Buchachenko, A. A.; Tscherbul, T. V. Cold Collisions of Heavy $^2\Sigma$ Molecules with Alkali-Metal Atoms in a Magnetic Field: Ab Initio Analysis and Prospects for Sympathetic Cooling of SrOH ($^2\Sigma^+$) by Li (2S). *Phys. Rev. A* **2017**, *95*, 63421.
- (298) Li, M.; Kłos, J.; Petrov, A.; Kotochigova, S. Emulating Optical Cycling Centers in Polyatomic Molecules. *Commun. Phys.* **2019**, *2*, 148.
- (299) Kozyryev, I.; Lasner, Z.; Doyle, J. M. Enhanced Sensitivity to Ultralight Bosonic Dark Matter in the Spectra of the Linear Radical SrOH. *Phys. Rev. A* **2021**, *103*, 43313.

- (300) Augenbraun, B. L.; Doyle, J. M.; Zelevinsky, T.; Kozyryev, I. Molecular Asymmetry and Optical Cycling: Laser Cooling Asymmetric Top Molecules. *Phys. Rev. X* **2020**, *10*, 31022.
- (301) Krems, R. V. Cold Controlled Chemistry. *Phys. Chem. Chem. Phys.* **2008**, *10*, 4079–4092.
- (302) Tscherbul, T. V.; Kłos, J. Magnetic Tuning of Ultracold Barrierless Chemical Reactions. *Phys. Rev. Res.* **2020**, *2*, 13117.
- (303) Anderson, M. A.; Barclay, W. L.; Ziurys, L. M. The Millimeter-Wave Spectrum of the SrOH and SrOD Radicals. *Chem. Phys. Lett.* **1992**, *196*, 166–172.
- (304) Dunning, T. H. Gaussian Basis Sets for Use in Correlated Molecular Calculations. I. The Atoms Boron through Neon and Hydrogen. *J. Chem. Phys.* **1989**, *90*, 1007–1023.
- (305) Feng, R.; Peterson, K. A. Correlation Consistent Basis Sets for Actinides. II. The Atoms Ac and Np–Lr. *J. Chem. Phys.* **2017**, *147*, 84108.
- (306) Lu, Q.; Peterson, K. A. Correlation Consistent Basis Sets for Lanthanides: The Atoms La–Lu. *J. Chem. Phys.* **2016**, *145*, 54111.
- (307) Li, M.; Coxon, J. A. High-resolution Analysis of the Fundamental Bending Vibrations in the $\tilde{A}^2\Pi$ and $\tilde{X}^2\Sigma^+$ States of CaOH and CaOD: Deperturbation of Renner–Teller, Spin–Orbit and K-type Resonance Interactions. *J. Chem. Phys.* **1995**, *102*, 2663–2674.
- (308) Li, M.; Coxon, J. A. Dye Laser Excitation Studies of the $\tilde{A}^2\Pi(100)/(020)$ – $\tilde{X}^2\Sigma^+(020)/(000)$ Bands of CaOD: Analysis of the $\tilde{A}^2\Pi(100)\sim(020)$ Fermi Resonance. *J. Chem. Phys.* **1996**, *104*, 4961–4977.

- (309) Shuman, E. S.; Barry, J. F.; DeMille, D. Laser Cooling of a Diatomic Molecule. *Nature* **2010**, *467*, 820–823.
- (310) Zeppenfeld, M.; Englert, B. G. U.; Glöckner, R.; Prehn, A.; Mielenz, M.; Sommer, C.; van Buuren, L. D.; Motsch, M.; Rempe, G. Sisyphus Cooling of Electrically Trapped Polyatomic Molecules. *Nature* **2012**, *491*, 570–573.
- (311) Prehn, A.; Ibrügger, M.; Glöckner, R.; Rempe, G.; Zeppenfeld, M. Optoelectrical Cooling of Polar Molecules to Submillikelvin Temperatures. *Phys. Rev. Lett.* **2016**, *116*, 63005.
- (312) Williams, H. J.; Caldwell, L.; Fitch, N. J.; Truppe, S.; Rodewald, J.; Hinds, E. A.; Sauer, B. E.; Tarbutt, M. R. Magnetic Trapping and Coherent Control of Laser-Cooled Molecules. *Phys. Rev. Lett.* **2018**, *120*, 163201.
- (313) McCarron, D. J.; Steinecker, M. H.; Zhu, Y.; DeMille, D. Magnetic Trapping of an Ultracold Gas of Polar Molecules. *Phys. Rev. Lett.* **2018**, *121*, 13202.
- (314) Anderegg, L.; Augenbraun, B. L.; Bao, Y.; Burchesky, S.; Cheuk, L. W.; Ketterle, W.; Doyle, J. M. Laser Cooling of Optically Trapped Molecules. *Nat. Phys.* **2018**, *14*, 890–893.
- (315) Cheuk, L. W.; Anderegg, L.; Augenbraun, B. L.; Bao, Y.; Burchesky, S.; Ketterle, W.; Doyle, J. M. Λ -Enhanced Imaging of Molecules in an Optical Trap. *Phys. Rev. Lett.* **2018**, *121*, 83201.
- (316) Hummon, M. T.; Yeo, M.; Stuhl, B. K.; Collopy, A. L.; Xia, Y.; Ye, J. 2D Magneto-Optical Trapping of Diatomic Molecules. *Phys. Rev. Lett.* **2013**, *110*, 143001.
- (317) Barry, J. F.; McCarron, D. J.; Norrgard, E. B.; Steinecker, M. H.; DeMille, D. Magneto-Optical Trapping of a Diatomic Molecule. *Nature* **2014**, *512*, 286–289.

- (318) Norrgard, E. B.; McCarron, D. J.; Steinecker, M. H.; Tarbutt, M. R.; DeMille, D. Submillikelvin Dipolar Molecules in a Radio-Frequency Magneto-Optical Trap. *Phys. Rev. Lett.* **2016**, *116*, 63004.
- (319) Tscherbul, T. V; Kłos, J.; Buchachenko, A. A. Ultracold Spin-Polarized Mixtures of $^2\Sigma$ Molecules with S-State Atoms: Collisional Stability and Implications for Sympathetic Cooling. *Phys. Rev. A* **2011**, *84*, 40701.
- (320) Tscherbul, T. V; Grinev, T. A.; Yu, H.-G.; Dalgarno, A.; Kłos, J.; Ma, L.; Alexander, M. H. Cold Collisions of Polyatomic Molecular Radicals with S-State Atoms in a Magnetic Field: An Ab Initio Study of He + CH₂ (\tilde{X}) Collisions. *J. Chem. Phys.* **2012**, *137*, 104302.
- (321) Song, J.; Khait, Y. G.; Wang, H.; Hoffmann, M. R. Low-Lying Electronic States of Difluorodioxirane. *J. Chem. Phys.* **2003**, *118*, 10065–10072.
- (322) Wang, H.; Khait, Y. G.; Hoffmann, M. R. Low-Lying Quintet States of the Cobalt Dimer. *Mol. Phys.* **2005**, *103*, 263–268.
- (323) Mbote, Y. E. B.; Khait, Y. G.; Hardel, C.; Hoffmann, M. R. Multireference Generalized Van Vleck Perturbation Theory (GVVPT2) Study of the NCO + HCNO Reaction: Insight into Intermediates. *J. Phys. Chem. A* **2010**, *114*, 8831–8836.
- (324) Mokambe, R. M.; Hicks, J. M.; Kerker, D.; Jiang, W.; Theis, D.; Chen, Z.; Khait, Y. G.; Hoffmann, M. R. GVVPT2 Multireference Perturbation Theory Study of Selenium Oxides. *Mol. Phys.* **2013**, *111*, 1078–1091.
- (325) Dunning Jr., T. H.; Hay, P. J. Gaussian Basis Sets for Molecular Calculations. In *Methods of Electronic Structure Theory*; Schaefer III, H. F., Ed.; Plenum: New

York, NY, 1977; pp 1–28.

(326) PyTorch

<https://pytorch.org/docs/stable/generated/torch.nn.MSELoss.html> (accessed Nov 5, 2021).

(327) Helgaker, T.; Jørgensen, P.; Olsen, J. *Molecular Electronic-Structure Theory*; Wiley: Chichester, 2000.

(328) Rubio, M.; Serrano-Andrés, L.; Merchán, M. Excited States of the Water Molecule: Analysis of the Valence and Rydberg Character. *J. Chem. Phys.* **2008**, *128*, 104305.

(329) Leszczynski, J. *Handbook of Computational Chemistry*; Springer: Dordrecht; New York, 2012.

(330) da Cruz, V. V.; Ertan, E.; Couto, R. C.; Eckert, S.; Fondell, M.; Dantz, M.; Kennedy, B.; Schmitt, T.; Pietzsch, A.; Guimarães, F. F.; Ågren, H.; Gel'mukhanov, F.; Odelius, M.; Föhlisch, A.; Kimberg, V. A Study of the Water Molecule Using Frequency Control over Nuclear Dynamics in Resonant X-Ray Scattering. *Phys. Chem. Chem. Phys.* **2017**, *19*, 19573–19589.

(331) Reuter, W.; Engels, B.; Peyerimhoff, S. D. The Reaction of Singlet and Triplet Methylene with Ethene. A Multireference Configuration Interaction Study. *J. Phys. Chem.* **1992**, *96*, 6221–6232.

(332) Shiozaki, T.; Werner, H.-J. Communication: Second-Order Multireference Perturbation Theory with Explicit Correlation: CASPT2-F12. *J. Chem. Phys.* **2010**, *133*, 141103.

(333) Herzberg, G. The Bakerian Lecture, The Spectra and Structures of Free Methyl and Free Methylene. *Proc. Math. Phys. Eng. Sci.* **1961**, *262*, 291–317.

- (334) Petek, H.; Nesbitt, D. J.; Darwin, D. C.; Ogilby, P. R.; Moore, C. B.; Ramsay, D. A. Analysis of CH₂ \tilde{a}^1A_1 (1,0,0) and (0,0,1) Coriolis-coupled States, \tilde{a}^1A_1 - \tilde{X}^3B_1 Spin-Orbit Coupling, and the Equilibrium Structure of CH₂ \tilde{a}^1A_1 State. *J. Chem. Phys.* **1989**, *91*, 6566–6578.
- (335) Yamaguchi, Y.; Sherrill, C. D.; Schaefer, H. F. The \tilde{X}^3B_1 , \tilde{a}^1A_1 , \tilde{b}^1B_1 , and \tilde{c}^1A_1 Electronic States of CH₂. *J. Phys. Chem.* **1996**, *100*, 7911–7918.
- (336) Jensen, F. *Introduction to Computational Chemistry*; Wiley: Hoboken, NJ, 2017.
- (337) Montgomery, J. M.; Alexander, E.; Mazziotti, D. A. Prediction of the Existence of LiCH: A Carbene-like Organometallic Molecule. *J. Phys. Chem. A* **2020**, *124*, 9562–9566.
- (338) Hertzberg, G. *Molecular Spectra and Molecular Structure III, Electronic Spectra and Electronic Structure of Polyatomic Molecules*; van Nostrand: New York, NY, 1966.